UNIVERSITÀ
DEGLI STUDI
DI PADOVA

Sede amministrativa: Università degli studi di Padova
Dipartimento di: Ingegneria dell'informazione

SCUOLA DI DOTTORATO DI RICERCA IN: INGEGNERIA DELL'INFORMAZIONE
INDIRIZZO: BIOINGEGNERIA
CICLO: XXIV

Development and web-based implementation of algorithms for the automatic analysis of vessels in retinal images

Direttore della scuola : Ch. mo Prof. Matteo Bertocco
Coordinatore d'indirizzo : Ch. mo Prof. Claudio Cobelli
Supervisore : Ch. mo Prof. Alfredo Ruggeri

Dottorando: Lara Tramontan

To myself

A fool thinks himself to be wise, but a wise man knows himself to be a fool.

WILLIAM SHAKSPEARE

In the long history of humankind (and animal kind, too) those who learned to collaborate and improvise most effectively have prevailed.

CHARLES DARWIN

Sommario

L'analisi del fundus retinico è diventata oramai un comune sistema diagnostico, in quanto permette di ottenere informazioni sulla circolazione sanguigna in maniera facile e non-invasiva. La mia attività di dottorato si è principalmente concentrata sullo sviluppo di algoritmi e tools per l'analisi dell'immagine retinica permettendo un'automatica e riproducibile conoscenza della circolazione sanguigna e in particolare dei parametri strutturali della rete vascolare e dei parametri clinici che da essi si possono dedurre.

Se parecchi algoritmi sono stati sviluppati allo scopo di segmentare i vasi sanguigni, molti pochi sono stati proposti per il postprocessing a questo primo step. Innanzitutto quest'ulteriore elaborazione è importante perchè la segmentazione potrebbe essere affetta da alcuni errori quali il riconoscimento come vasi di altre regioni scure dell'immagine (per esempio microaneurismi e emorragie in situazioni patologiche dell'occhio, o solamente rumore, ombre e la fovea in condizioni normali). Quindi il primo compito del postprocessing consiste nel miglioramento delle prestazioni dell'algoritmo di tracking in termini di specificità: a questo scopo un modulo per il riconoscimento di falsi vasi è stato sviluppato.

Dopo questo step preliminare, l'algoritmo di postprocessing analizza la rete vascolare precedentemente segmentata allo scopo di ricavare alcuni punti d'interesse dell'immagine, alcuni di essi appartenenti alla rete vascolare come biforcazioni e incroci, altri deducibili da essa come il disco ottico e la fovea. I vasi sanguigni emergono dal disco ottico come arteriole, si aprono e si diffondono quasi radialmente (nell'immagine retinica assumono un profilo a doppia arcata) e allo stesso tempo si assotigliano fino a diventare capillari. Molti di essi convergono nella fovea, ossia la zona della retina con la massima acuità

visiva. Da essa dipartono i capillari con flusso venoso seguendo un percorso a parabola simile a quello arteriolare per riunirsi ancora poi nel disco ottico. Questo definito comportamento è stato utilizzato dall'algoritmo come un'utile informazione per l'identificazione del disco ottico e della fovea a partire dalla rete vascolare segmentata. L'importanza di questi punti è da ricondurre a molteplici ragioni: molte patologie colpiscono il disco ottico (come il glaucoma) o la fovea (come nella telengiectasia maculare) o entrambi e spesso il loro riconoscimento è usato per altri scopi quali la calibrazione dell'immagine. Inoltre nell'algoritmo di postprocessing l'informazione sulla loro posizione permette di capire il verso del flusso sanguigno all'interno dei singoli segmenti di vasi disconnessi tra loro. Questa informazione è stata sfruttata per la connessione di tali segmenti in un unico vaso, per esempio in presenza di un incrocio, e nel riconscimento di biforcazioni quando due rami dipartono da un unico vaso.

L'algoritmo di postprocessing permette inoltre di classificare i vasi in arterie e vene ed esso può essere applicato nella diagnosi precoce delle retinopatie. Infatti nei primi stadi di diverse patologie sono visibili cambiamenti a livello vascolare che interessano diversamente i due tipi di vaso. Le arterie di solito appaiono più chiare delle vene e talora con un riflesso centrale dovuto alla maggiore reflettività delle pareti arteriolare in presenza di ossigeno.Tuttavia queste differenze colpiscono solo i vasi maggiori e variano fortemente da paziente a paziente e a seconda delle zone della retina, rendendo la loro classificazione un difficile compito. L'algoritmo di classificazione proposto usa un approccio modulare probabilistico: sono stati implementati diversi classificatori che restituiscono ognuno una probabilità che il vaso considerato sia vena (uguale a 1 meno la probabilità di essere arteria). Le diverse probabilità sono poi integrate sfruttando anche metainformazioni derivanti da caratteristiche topologiche dei vasi: agli incroci i due vasi appartengono a classi diverse e alle biforcazioni i due rami appartengono alla stessa classe del tronco e, ancora, nell'area attorno al disco ottico un' arteria è spesso alternata ad una vena.

Oltre allo sviluppo dell'algoritmo di postprocessing la mia attività si è focalizzata sull'applicazione dell'informazione vascolare per la stima di alcuni indici clinici, in particolare della tortuosità e del rapporto Artero-Venoso

(AVR). E' stato ampiamente dimostrato che le arterie si restringono (e conseguentemente è misurato un ridotto valore dell'AVR) in presenza di alcune patologie oculari come nella retinopatia diabetica e ipertensiva. E' stato osservato che uno dei loro effetti è una cresciuta tortuosità vascolare: i vasi retinici in condizioni normali sono dritti o leggermente curvi, ma si dilatano e aumentano in tortuosità in presenza di alta pressione del sangue, angiogenesi e congestione vasale. Tuttavia questo comportamento, in particolare nel caso del diabete, non è stato chiaramente capito e dimostrato in maniera affidabile, sostanzialemente perchè una misura quantitativa della tortuosità non esiste ancora, così come i tool per poterla misurare. Fino ad ora la tortuosità è stata valutata dagli esperti usando una scala qualitativa (leggera, modesta, severa e estrema), ma una misura quantitativa permetterebbe di comprendere e verificare più facilmente la tortuosità vascolare retinica e la sua progressione. Inoltre la mancanza di tool che forniscono una misura automatica di tortuosità, ha finora impedito l'analisi di questo segno nella normale pratica clinica. Infine in letteratua alcuni lavori propongono misure di tortuosità del singolo vaso, mentre non è ancora stata proposta una misura di tortuosità dell'intera immagine. La collaborazione con il Reading Center, Dipartimento R&D, del Moorfields Eye Hospital di Londra, dove ho trascorso sei mesi, ha permesso di approfondire la conoscenza riguardo i cambiamenti di tortuosità dei vasi in presenza di retinopatia diabetica. Inoltre ha permesso di svolgere uno studio sulla valutazione degli esperti e la loro percezione riguardo il parametro tortuosità e, infine, di sviluppare un tool per la misura di questo parametro. Lo studio riguardo la percezione clinica della tortuosità è stato organizzato come segue: è stato chiesto a due esperti di classificare il livello di tortuosità (distinguendo tra 6 classi) di un dataset di 200 immagini appartenenti a 50 pazienti mongoli (2 immagini per occhio: una con FoV centrato sul disco ottico, l'altra sulla macula, e entrambi gli occhi sono stati considerati). E' apparso che i graders condividono, ma solo modestamente, la percezione di tortuosità, che entrambi i FoV sono necessari per una misura affidabile di tortuosità e la modesta correlazione tra occhio destro e sinistro ha suggerito che la tortuosità potrebbe essere parzialmente congenita e parzialmente dovuta a condizioni patologiche del singolo occhio. Allo scopo di stimare la tortuosità in modo automatico, una misura di tortuosità del singolo vaso è stata proposta:

essa integra l'informazione sul numero di cambiamenti di convessità (o del segno di curvatura) del vaso e sull'ampiezza di ciascun segmento di curva (delimitato da due cambiamenti in convessità), e considera anche il diametro del vaso. Una seconda misura di tortuosità è stata proposta: essa considera soltanto i cambiamenti locali di curvatura e il diametro locale del vaso, senza considerare a quale vaso appartenga il punto considerato. Entrambe le misure correlano bene con la percezione di tortuosità degli esperti, offrendo quindi una stima di essa quantitativa, obiettiva e riproducibile. Inoltre la correlazione di tali misure con i dati clinici suggerisce che la tortuosità abbia potere diagnostico per la retinopatia diabetica.

Infine due sistemi sono stati sviluppati: uno per la stima dell'AVR (AVR-net) e l'altro per la stima della tortuosità (TorTnet). Entrambi sono composti di un modulo automatico per il tracking vascolare, di un'interfaccia interattiva per correggere gli errori in modo facile e veloce e per settare i parametri d'analisi richiesti, e di un modulo per il calcolo degli indici clinici. I sistemi sono stati organizzati con una struttura client-server per permettere a clinici e ricercatori da tutto il mondo di poter lavorare con essi da remoto.

Summary

The retinal fundus image analysis has become a common diagnostics tool, as it allows e.g. to gather information on the blood circulation in an easy and non-invasive way. My activity during the PhD has primarily focused on the development of algorithms and tools for the retinal images analysis allowing an automatic and reproducible understanding of information about the blood circulation and in particular about the structural features of the vascular network and the clinical parameters inferable from them.

If several algorithms have been developed to segment the blood vessels, a very few algorithms have been proposed for the postprocessing to the vessel tracking step. First of all this step is useful because the segmentation could be affected by some errors as the detection as vessels of some other dark regions in the image (for example microaneurysms and haemmorages in pathological eyes conditions, or just noise, shadows and the fovea in normal conditions), therefore the first task of the postprocessing is to improve the performance of the tracking algorithm in terms of specificity: a module for the false vessels detection has been developed.

After this preliminary step, the postprocessing algorithm analyzes the segmented vessels network in order to detect some points of interests in the image, some of them belonging to the vascular network as bifurcations and crossing points, other inferring from it as the optic disk and the fovea. The blood vessels in the eyes emerge from the optic disk as arteriolars, they open and spread almost radially (appearing in the image of the retina as a double arcade) and in the meantime they get narrower until they become capillaries. Most of them converge on the fovea, which is the area with the greatest visual acuity. From it the capillaries with venous blood depart following a

parabolic course similar to the arteriolars one and they join again into the optic disk. This standard behavior have been used in the algorithm as a useful information for the detection of the optic disk and the fovea starting from the segmented vessels network. These points are important for many reasons: a lot of pathologies affect or the optic disk (as in the glaucoma) or the fovea (as in the macular telengiectasia) or both and they are often detected to perform other tasks as for the image calibration. Moreover in the postprocessing algorithm the information about their position has been used to understand which is the versus of the blood flux inside each disconnected vessel segment. This information has been exploited for the linking of the segments into a single vessel, for example where a crossing is present, and in the detection of the bifurcations where two branches depart from a single vessel.

The postprocessing algorithm allows also the vessels classification in arteries and veins and it can be applied in the early diagnosis of retinopathies. Indeed, in the early stage of several diseases vascular changes do appear but they often affect differently each type of vessels. Arteries usually appear brighter than veins and sometimes with a central reflex due to the increased reflectivity of the arteriolar walls because of the oxygen content. Nevertheless these dissimilarities affect only the main vessels and strongly vary dependent on patients and locations on the retina, making their classification an hard task. The developed algorithm of classification uses a modular probabilistic approach: different classificators have been implemented providing each one a probability that a vessel is vein (equal to one minus the probability to be artery). The different probabilities are then integrated exploiting also metaknowledge information deriving from topological features: at crossings the two vessels have to belong to different classes, at a bifurcation the two branches belong to the same class of the trunk and in the area around the optic disk an artery often alternates with a vein.

Besides the development of the postprocessing algorithm my activity focused on the application of the vascular information for the estimation of some clinical indexes, in particular the vessels' tortuosity and the Artery-to-Vein Ratio (AVR). It has been widely demonstrated that arteries becomes narrower (and consequently a reduced value of the AVR is measured) in presence of some eye's pathologies as in the diabetic and hypertensive retinopathy.

It has been also observed that one of their effects is an increased vessel tortuosity: normal retinal blood vessels are straight or gently curved, but they become dilated and tortuous in presence of high blood flow, angiogenesis and blood vessel congestion. Nevertheless this behavior, in particular in the case of diabetes has not been clearly understood and reliably demonstrated, basically because a consistent quantitative measure of tortuosity and tools to measure it in an automatic way, do not exist yet. Until now the tortuosity has been evaluated by the graders using a qualitative scale (e.g. mild, moderate, severe, extreme) but a reliable quantitative measure would enable the retinal vascular tortuosity and its progression to be more easily concerned. Moreover the lack of tools providing an automated measurement of the tortuosity has until now prevented the analysis of this sign in the normal clinical practice. Finally, in literature some works propose measures to evaluate the tortuosity of just the single vessel, whereas a measure of the tortuosity of the global image has not been proposed yet. The collaboration with the Reading Centre, R&D department, at the Moorfields Eye Hospital, where I passed six months as a research fellow, allowed a deeper understanding of the vascular changes in tortuosity in the diabetic retinopathy, to perform a study about the graders' evaluation and perception of the tortuosity feature and, finally, to develop a tool for the measure of this parameter. The study about the graders' perception of the tortuosity has been organized as it follows: two graders has been asked to classify the level of tortuosity (distinguishing among 6 different classes) on a medium large dataset of 200 images belonging to 50 diabetic Mongolian people (2 images per eye: one with field of view centered on the optic disk, the other on the macula, and both the eyes have been considered). It resulted that the graders agreed, but just modestly, about the perception of the images' tortuosity, both the field of view are needed for a reliable measure of the tortuosity and just a medium correlation between the right and left eyes has been measured suggesting that the tortuosity could be just partially congenital and partially due to the pathological condition of the single eye. In order to estimate the tortuosity in an automatic way a measure of tortuosity of the single vessels has been proposed: it integrates information on how many times a vessel changes convexity (or curvature sign) and on how large is the amplitude of each of the recognized turn curves (each segment delimited

by two changes in convexity) and it considers how large is the vessel diameter. Moreover another measure of tortuosity has been proposed: it considers just the local changes of curvature and the diameter in that point of the vessel, regardless of that point belongs to a vessel or another one. Both the measures well correlate with the graders' perception of the tortuosity, providing a quantitative, objective and reproducible estimation of it. The correlation with the clinical data also suggests that the tortuosity has a diagnostic power for the diabetic retinopathy.

Finally two systems have been developed: one for the estimation of the AVR (AVRnet) and the other one for the estimation of the tortuosity (TORTnet). Both of them are composed of a module for the automatic vascular tracking, an interactive editing interface to correct errors in a fast and easy way and set the required parameters of analysis, and a module for the computation of clinical indexes. The systems have been organized as a client-server structure to allow clinicians and researchers from all over the world to work remotely with them.

Contents

Chapter 1

Introduction

Hypertensive retinopathy is associated with systemic arterial hypertension; retinal vascular changes can be seen in both chronic and acute stages. It is likely that an increasing number of patients in the future will suffer from hypertension, a pathology ranked as one of the top-10 risk factors for burden of diseases in developed countries by the World Health Organization. In this context, it must be noticed that ophthalmologists occupy a privileged, central position in the detection of the disease, and consequently in the prevention of the visual loss it causes: indeed, a patient with undiagnosed malignant hypertension will probably consult first an ophthalmologist with a complaint of visual loss.

An even more dramatic situation characterizes diabetes-related retinopathy. Diabetes is a growing epidemic in the world, due to population growth, aging, urbanization and increasing prevalence of obesity and physical inactivity: it is estimated that the population with diabetes will grow by 37% by 2030, and today it already counts around 200 million people worldwide. Following the trend of diabetes, diabetic retinopathy assumes an ever increasing importance as a cause of blindness: in the United States it constitutes the first cause of blindness in subjects in working age, with all the economic and social burdens this implies. The timely diagnosis and referral for management of diabetic retinopathy can prevent 98% of visual loss. It is estimated that the underlying cause of blindness in the majority of diabetic patients is not diabetic retinopathy per se but the misdiagnosis of diabetic retinopathy.

Currently, a periodic dilated direct ophthalmoscopic examination appears to be the best approach for a screening with near universal coverage of the population at risk, despite the proved low sensitivity of direct ophthalmoscopy [1], [2], [3]. However, the number of ophthalmologists available is a limiting factor in initiating an ophthalmological screening [4].

With the increasing availability of digital fundus cameras, there is a wide consensus of opinion that an automatic analysis of such digital images might, at least partially, relieve ophthalmologists of the burden of retinopathy screening.

1.1 Aims and Objectives

The aims of the work presented in this thesis are the development of algorithms and tools for the retinal images analysis allowing an automatic and reproducible understanding of information about the blood circulation and in particular about the structural features of the vascular network and the clinical parameters inferable from them.

The morphology of the vascular structure can be affected by different abnormalities caused by acute pathologies or by early signs of certain systemic disease, such as diabetes and hypertension. Ocular fundus images can provide important information about these signs and their accurate analysis is necessary to improve clinical diagnosis of diseases. An *automatic and quantitative assessment of vessel morphological features*, such as diameters and tortuosity, can reveal important information on the mentioned diseases.

To this aim, not only the exact layout of vessels in the image must be extracted, but also their connections and bifurcations must be detected. Indeed the procedure for the parameter estimation requires that the vascular network is segmented and that the *vascular tree is recognized*, with its main and secondary vessels and their different orders of bifurcations until they become capillaries. The bifurcation points themselves are points of interest for the diagnosis of the retinopathy, since the angle between the two branches and the relation between the diameters of brunches and trunk have a significant diagnostic power.

Moreover the *vascular tree must be distinguished in the arteriolar and*

venular components, because the two types of vessels are often affected in different way by pathologies. For example an important diagnostic sign for both the hypertensive and diabetic retinopathy is the generalized arteriolar narrowing, reflected by decreased value of the CRAE (Central Retinal Arteriolar Equivalent) parameter [5]. In addition, it has been suggested that changes in the arteriolar tortuosity are related to pathological conditions, in particular in the hypertensive retinopathy, but also in the diabetic and hereditary vascular retinopathy [6]. In presence of high blood pressure, vessels may increase in length and vessel walls thicken, and as a result they become increasingly tortuous. This is at first seen in arteries, and only in more severe stages of retinopathy, also in veins. Although different studies support the diagnostic power of the tortuosity parameter, its value in particular for the diabetic retinopathy is not clearly understood.

An important purpose of my activity regarded *a study about the tortuosity sign* performed in collaboration with the Reading Center, R & D Department, at the Moorfields Eyes Hospital, one of the main center for research and clinics in the ophthalmological field. The aim has been threefold: firstly the investigation of the clinical perception of the tortuosity of retinal vessels, secondly the formulation of a quantitative and automatic measure of this parameter and the development of a web-based tool for its estimation and thirdly a study about the tortuosity diagnostic power for the diabetic retinopathy.

My activity focused also on another important parameter: the Artery to Vein Ratio (AVR), which measures the generalized arteriolar narrowing [5]. Despite its importance in the diagnosis of both the hypertensive and diabetic retinopathy, its application in a clinical context is not a common practice. The first limitation is the lack of a standardized accurate, precise and fast tool for the AVR estimation, which requires an high accuracy both in the vessels diameter estimation and in the artery-vein classification. Thanks also to the collaboration with the Department of Ophthalmology and Visual Sciences, University of Wisconsin, Madison, WI (USA) (one of the main centers in the ophthalmological context) and with the Twin Research & Genetic Epidemiology Department, KingŠs College London Division of Genetics and Molecular Medicine, St ThomasŠ Hospital, (UK), an *accurate, fast and user-friendly web-based system for the AVR computation* could be developed.

1.2 Outline

Chapters 2 is introductory and describes the main features of the retinal imaging: the fundus camera examination, the appearance of the retina in a fundus image, and the main findings of hypertensive and diabetic retinopathy.

Chapter 3 describes the postprocessing step to the vascular segmentation, which is a prerequisite for the following parameter estimation. First of all an algorithm for the false vessel detection is presented. Secondly algorithms for the detection of retinal points of interest are described. These landmarks comprise the optic disc center, the fovea, the vessels bifurcations and crossings. Their importance is to be ascribed to the estimation of parameters directly measurable from them (as the bifurcation angle and the Salus & Gunns signs at crossings) as well as of parameters whose procedure estimation needs this intermediate landmarks detection (as for the AVR and tortuosity parameters).

Chapter 4 deals with the algorithm for the artery-vein vessels classification. A particular customization of this algorithm regards the AVR computation, which is performed in a circular region centered at the optic disc.

Chapter 5 presents the tool for the AVR estimation: the AVRnet system, which has been conceived as a web-based application.

Finally chapter 6 deals with the study about the tortuosity parameter and presents another web-based application for its computation: the TorTnet system.

Chapter 2

Fundus Imaging and its Findings

In this chapter a brief review will be presented about what is seen in an image from a fundus camera examination and all the most relevant lesions to be found in the hypertensive and diabetic retinopathy.

2.1 Fundus Oculi Examination

The first instrument that made available to ophthalmologists the direct examination of the retina was the direct ophthalmoscope, which is still used today. It was first described by Helmholtz at the end of the XIX century, and since then it has not changed much. In its basic form is composed by a light source and a set of lenses. The light is projected through the dilated pupil onto the retina, and the lenses focus on so that the observer can look at the retina. Its use is widespread in the clinical practice, but it has been proved to provide poor sensitivity and results highly dependent on the observer experience.

In the middle of the XX century the first instrument able to acquire photographs of the retina appeared. This is a photographic 35mm back connected to an optic system that focuses on the fundus oculi, illuminated by a coaxial flash. This fundus camera enables the photography of different portions of the retina with different magnification, which ranges from 10^o to 60^o.

Around 1990, the first digital fundus camera appeared. The optic system is not connected anymore to a traditional camera, but to a CCD, and the image is sent to a computer for visualization and storage.

2.1.1 Fundus Oculi Appearance

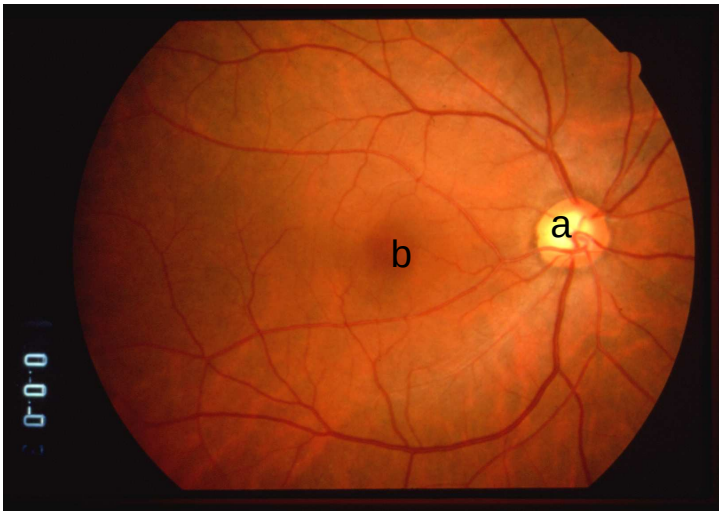

Figure (2.1). *An image of a normal fundus oculi. Papilla (a), fovea (b) and vessel networks are clearly visible*

Using a fundus camera, an image of the fundus oculi is acquired. The visible part of it is composed by the retina with its vascular network and the optic nerve head. The choroid is the structure below the retina and is usually obscured by it.
The retina is a multilayer structure, which is transparent except for the deepest layer, the pigmented epithelium. This gives to the retina its reddish colour. More superficially than the pigmented epithelium there is the sensorial retina, composed by the photoreceptor cells and by the gangliar cells. The axons of the gangliar cells runs to the papilla, or optic disc, or optic nerve head, which is the place where the bundle of nervous fibers forms the optic nerve, and leaves the optic bulb. From the center of the optic disc the ophthalmic artery enters into the optic bulb, and subsequently branches to provide vascularization to most of the retina. From the capillary network

originates the venous vessels, which flow into the central retinal vein that exit the ocular bulb through the optic disc.
Topologically, the temporal vessel arcades delimit the posterior pole. At the center of the posterior pole there is the macula: its center is occupied by a small depression, the fovea, that is the region most densely packed with photoreceptor of the retina and is normally the center of vision. The macula is not fed by retinal vessels, but takes its nutrients from the choroid vessels below the retina.
Choroidal vessels are not usually visible in an image taken with a fundus camera, but if the the pigmented epithelium is very lightly pigmented or in case of pathological depigmentation, the retina becomes almost transparent and the choroid becomes visible.

2.2 Main Vascular Abnormalities

2.2.1 Tortuosity

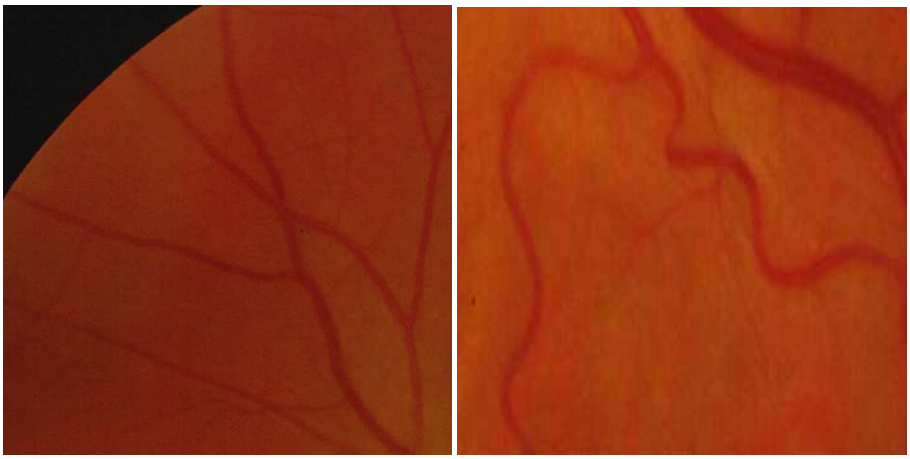

(a) (b)

Figure (2.2)

In presence of high blood pressure, vessels may increase in length and vessel walls thicken, and as a result they become increasingly tortuous. This is at first seen in arteries, and only in more severe stages of retinopathy, also in veins.

2.2.2 Generalized Arteriolar Narrowing

The earliest fundus change due to hypertension is the thinning of the retinal arterioles. Narrowing of the arterioles is usually proportional to the degree of elevation of blood pressure. However, retinal arteriolar narrowing is imprecisely quantified from a clinical ophthalmoscopic examination, since the examiner should estimate the normal vessel width prior to the narrowing to evaluate severity of the latter.

2.2.3 Focal Arteriolar Narrowing

Figure (2.3). *A definite focal narrowing*

In severe hypertension states, irregularities in the caliber of blood vessels may appear. In arterioles, they are due to localized spasm and contraction of the wall. They appear as a focal thinning of the blood column: the narrowing may increase until the vessels become thread-like.

2.2.4 Bifurcations Abnormalities

Arterial diameters and topography at branch points are believed to conform to design principles that optimize circulatory efficiency and maintain constant shear stress across the network [7]. It has been suggested that arterial diameters at a bifurcation should conform to a power relationship, and arterial branches in various circulation have been shown to obey to this design. It

has been shown that bifurcation angles are reduced with increasing hypertension, probably because the atheroma fibrosis of the central artery displace by contraction the arteries toward the disk. Although the mechanisms of bifurcation changes are not clear, both branching angles and also the value of the junction exponent seems to deviate from its optimal values with age [8]

2.2.5 Crossing Abnormalities

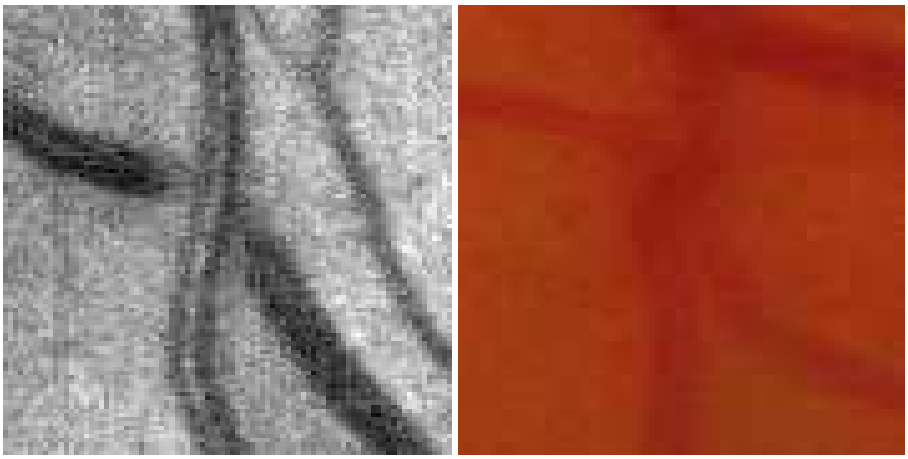

(a) (b)

Figure (2.4)

The abnormal changes in arteriovenous crossings result from the thickening of the wall of the arterioles due to hypertension and sclerosis, and associated changes in the veins at the crossings. The first appearance of crossing abnormalities is the compression of the vein by the artery, which may vary in severity from a slight indentation to complete interruption of the vein where the artery crosses. When the sclerotic process in the artery extends to the adventitia of the vein, the blood column in the vein will be partially obscured and appear tapered on each side of the crossing.
Constriction and compression of the veins may impede the blood return, so that the veins become distended for some distance peripheral to the crossing: this is the so called Gunn's sign.
The arterial sclerosis may cause deflection of the vein from its normal course at the point where the artery crosses. The vein may deflect both vertically

(dipping under the artery or humping over it), or laterally. In this last case, instead of crossing the artery obliquely, the vein does so at right angles and appears as S-shaped at the bend, which has been referred as the Salus sign.

2.3 Main Non Vascular Findings

2.3.1 Microaneurysms and Red Dots

(a) (b)

Figure (2.5)

Retinal microaneurysms are the most characteristic lesion of diabetic retinopathy, but are present also in other pathologies that affect the microvessels. Micoraneurysms are a small dilation of a capillary wall. It is not clear if retinal microaneurysms are due to a vessel wall damage or to the beginning of a neovascolarization. However, the result is the appearance of small saccular structures, of approximate dimension between $10\mu m$ and $100\mu m$, that in the retinal fluorescein angiography appear as bright hyperfluorescent spots, whereas in colour fundus images appears as round, red spots. They are indistinguishable from small hemorrhages of the same dimension, since they both are small round regions, with a dark red colour. Therefore, both microaneurysms and hemorrhages smaller than the major vein caliber at the optic disc margin (usually 125 μm), are considered red dots, and evaluated as microaneurysms [9]. On the contrary, any red spot greater than that is considered an hemorrhage, unless features as round shape, smooth margins and a central light reflex suggest that it is probably a microaneurysm.

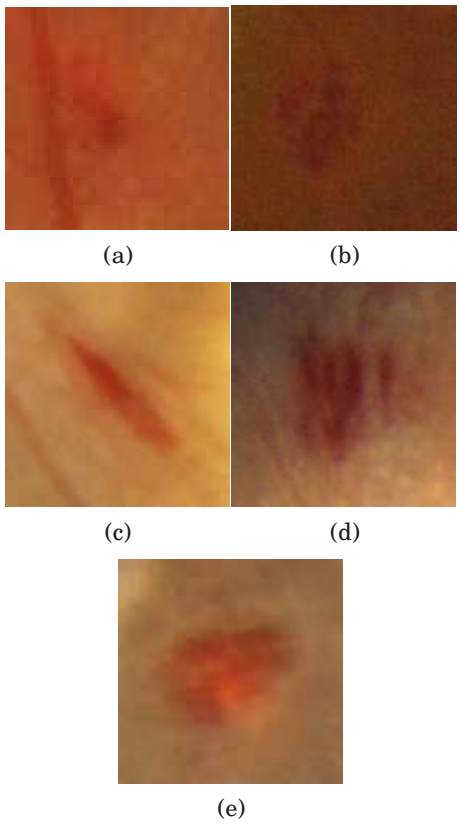

Figure (2.6)

2.3.2 Hemorrhages

Retinal hemorrhages are blood deposits on the retina. Hemorrhages disappear as the blood is reabsorbed with time.
They are due to the breaking of a vessel wall or of a microaneurysm, and the increase in their presence is a clear sign of diffuse retinal damage.
They have very different shapes, going from the round red spot with sharp margins, to the blot hemorrhage, to the flame-shaped hemorrhage. As the blood is reabsorbed, hemorrhage margins fade and the characteristic red colour turns to a faint greyish-red before disappearing completely.

2.3.3 Hard Exudates

Hard exudates are small lipidic and proteinic deposits, which appear as white or yellowish-white areas with sharp margins. They may be arranged as in-

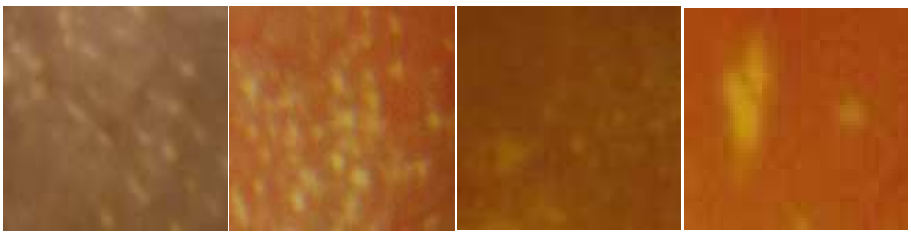

Figure (2.7). *Different hard exudates*

dividual dots, confluent patches or in partial or complete rings surrounding microanaeurysms or zones of retinal edema. In the more severe cases of hypertensive retinopathy, they appear as a confluent ring around the macula (the macular star).

2.3.4 Cotton Wool Spots

Figure (2.8). *Cotton wool spots*

Cotton wool spots are the consequence of retinal ischemic events, due to precapillary arterioles stenosis. This causes a swelling of the nerve fiber layer, with local deposit of cytoplasmatic material. They are round or oval in shape, white, pale yellow-white or greyish-white, with soft and feathery edges, that give their characteristic aspect and their name. They usually appear along the major vessel arcades, parallel to the nerve fibers, and are sometimes accompanied by the presence of microaneurysms.

2.3.5 Drusen

Drusen are deposits associated with thinning or hypopigmentation of the retinal pigment epithelium. They appear as deep, yellowish-white dots. To distinguish drusen from hard exudates, good stereoscopic view would be necessary,

since drusen appear very deep while hard exudates are slightly more superficial. In the protocol used in this thesis the photographs are mono, therefore it is not easy to identify hard exudates from drusen. Several other features are used in distinguishing drusen from hard exudates. Drusen are usually scattered diffusely or scattered near the center of the macula. They are usually round in shape, while hard exudates are usually irregular in shape. Finally, drusen have often a faint border of pigment.

2.4 Hypertensive Retinopathy Grading

The classification of hypertensive changes in the retina in a severity scale was first proposed by Keith [10], in what is now currently known as the Keith-Wegener-Barker grading system. It was subsequently modified by Scheie [11] to better separate hypertensive from atherosclerotic abnormalities. In Tab. 2.1 the two classifications for hypertensive retinopathy are shown. It is worth noting that recent literature challenges the prognostic significance of these classifications. The poor correlation with the severity of hypertension variation in the onset and progression of the clinical signs, has suggested the use of a classification of retinopathy into two grades: non-malignant and malignant [12]. This is further confirmed by the fact that density of perifoveal capillaries and capillary blood flow velocity analysed with an angiographic examination, correlate more with a two grade rather than with the classical four grade classification system. Nevertheless, the Keith-Wegener-Barker is still the standard *de facto* in the evaluation of hypertensive retinopathy.

2.5 Diabetic Retinopathy

Two landmark clinical trials set the standard in grading diabetic retinopathy. They are the Diabetic Retinopathy Study (DRS) [13] and the Early Treatment Diabetic Retinopathy Study (ETDRS) [14]. The ETDRS severity scale was based on the Airlie House classification of diabetic retinopathy and is used to grade fundus photographs. It has been widely applied in research settings, publications and it has shown satisfactory reproducibility and validity. Although it is recognized as the *gold standard* for grading the severity

Keith-Wegener-Barker		Scheie	
Grade	Features	Grade	Features
I	Mild generalised retinal arteriolar narrowing. Increased arterial tortuosity	1	Barely detectable arterial narrowing
II	Definite focal narrowing and arteriovenous crossing abnormalities	2	Obvious arterial narrowing with focal irregularities and light reflex changes
III	The above and retinal hemorrhages, exudates and cotton wool spots	3	The above plus copper wiring,and retinal hemorrhages and exudates
IV	Severe grade III plus papillar oedema	4	Grade 3 plus silver wire and papillar oedema

Table (2.1). *Classification of hypertensive retinopathy as proposed in [10] and [11]*

of diabetic retinopathy in clinical trials, its use in everyday clinical practice has not proven easy or practical. The first reason for this is that the photographic grading system has 90 levels, many more than what is necessary for clinical care. Given the number of levels to consider and the detailed specific definitions of the levels, and the requirement of comparison with standard photographs, it is not surprising that ETDRS grading procedure is difficult to remember and apply in a clinical setting.

Recently, simplified severity scales have been developed in an effort to improve both the screening of patient with diabetes and communication among caregivers. Yet, to overcome this proliferation of *ad hoc* grading scales, it has been proposed in [**?**] a Diabetic Retinopathy Disease Severity Scale, in which separate scales were proposed to grade diabetic retinopathy (4 levels) and macular oedema (5 levels). The two scales are summarized in in Tab. 2.2 and Tab. 2.3.

Disease Severity Level proposed in [**?**]	Findings Observable on Dilated Ophthalmoscopy
No Apparent Retinopathy	No abnormalities
Mild nonproliferative diabetic retinopathy	Microaneurysms only
Moderate nonproliferative diabetic retinopathy	More than just microaneurysms but less than severe nonproliferative diabetic retinopathy
Severe nonproliferative diabetic retinopathy	Any of the following: more than 20 intraretinal hemorrhages in each of 4 quadrants; definite venous beading in 2 or more quadrants; prominent intraretinal microvascular abnormalities in one or more quadrant and no signs of proliferative diabetic retinopathy
Proliferative diabetic retinopathy	One or more of the following: neovascularization, vitreous or preretinal hemorrhage

Table (2.2). *Classification of diabetic retinopathy as proposed in [?]*

Disease Severity Level proposed in [**?**]	Findings Observable on Dilated Ophthalmoscopy
Diabetic macular oedema apparently absent	No apparent retinal thickening or hard exudates in posterior pole
Mild diabetic macular oedema	Some retinal thickening or hard exudates in the posterior pole but distant from the center of the macula
Moderate diabetic macular oedema	Retinal thickening or hard exudates approaching the center of the macula but not involving the center
Severe diabetic macular oedema	Retinal thickening or hard exudates involving the center of the macula

Table (2.3). *Classification of diabetic macular oedema proposed in [?]* . Hard exudates are a sign of current or previous macular oedema. Diabetic macular oedema is defined as retinal thickening and requires a three-dimensional assessment.

Chapter 3

The Postprocessing for the Points of Interest localization

In this chapter algorithms for the detection of important points of interest in retinal images are presented. The vascular network is assumed to be already segmented, at least partially and with some errors, manually or automatically by any algorithm for the vessels detection. The segmentation can provide the singular vessel structures or just the binary image vessel-no vessel, in this case a skeletonisation process is applied. From the vascular network a lot of features can be deduced and related parameters can be measured, some of them directly from the vascular structures as those concerning diameters or particular configurations at crosses and bifurcations, and others indirectly considering the vessels pattern as those regarding the optic disk and the fovea.

Although the postprocessing modules presented in this chapter are assumed to work after any algorithm for the vessel detection, we start describing briefly the one proposed by our group in [15], because it is the one mostly applied in the images analyzed. Then a module to improve the performance of the tracking algorithm in terms of sensibility, specificity and precision is presented, followed by the description of algorithms to build up the vascular network and to detect important points of interest.

3.1 Vessel Tracking

The methods to detect the vascular tree can de distinguished in global and tracking techniques. Global techniques based on template matching techniques to automatically extract vessels are adversely affected by the large variability in vessel caliber distribution [16]. To circumvent this problem, multi-scale approaches have been proposed [17]. However, those algorithms are computationally demanding, as they involve the processing of the entire image with a large number of filters.

Unlike the global techniques, tracking-based segmentation methods trace the vessels by analyzing local areas. Starting from a set of starting points (seeds), they proceed along the corresponding vessels. Methods proposed in the literature to this end use matched filters [18], morphological filters [19], optimization of Gaussian profiles [20] or classification techniques (vessel or non vessel pixels) based on vessel profiles [21]. Compared to the global techniques, tracking has obvious advantages in terms of computational efficiency, since the number of pixels analyzed is far smaller than the image dimension.

Seed points can be found starting from easily recognizable areas of the image (e.g. the optic disc [21]) and then exploring the outer regions. However, this approach may fail to track peripheral and low-contrast vessels. A more principled approach implies sparse tracking [22], where seeds are found over the whole image. This in turn requires a joining algorithm that connects segments resulting from separate tracking of the same vessel.

In order to extract the vascular network from retinal images, we decided to avoid global methods (which usually need long processing time) and developed an algorithm based on a tracking technique, which analyzes only localized areas of the image. It starts from a set of initial points (seeds) and it proceeds along the corresponding vessels employing a multi-directional graph search approach [15]. Vessel axes and diameters are estimated in two consecutive steps.

A seed finding procedure aims to extract in a fast and robust way a set of seed points, from where the tracking can start. To this end, a regular grid of lines and/or curves is analyzed to search for candidate seed points. On each selected line/curve, the gray-level profile is extracted (Fig.3.1b, 3.1c) and ana-

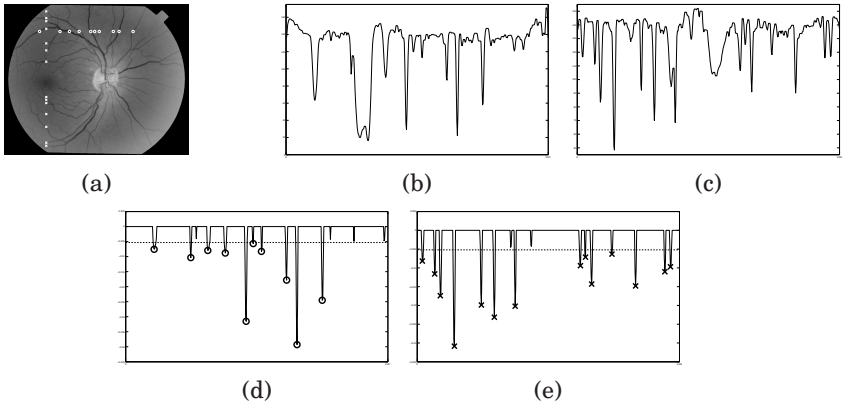

Figure (3.1). *(a)Seed points (b)found by analyzing the horizontal profile and (c)the vertical profile. After matched filtering (d)(e), thresholding provides the set of points suggesting the presence of vessel: circles and crosses correspond to the seeds shown in (a).*

lyzed by means of a matched filter method, looking for patterns corresponding to candidate vessels. The convolution of the profile with a discretized Laplacian of Gaussian function filter over multiple scales is performed. To avoid that the largest response is always obtained with the largest scale, we normalize the response by dividing it by the profile norm and the kernel norm. The maximum response among the output results is then saved (Fig.3.1d, 3.1e). The local peaks of such output indicate the possible presence of a vessel in the corresponding points of the image (Fig.3.1a).

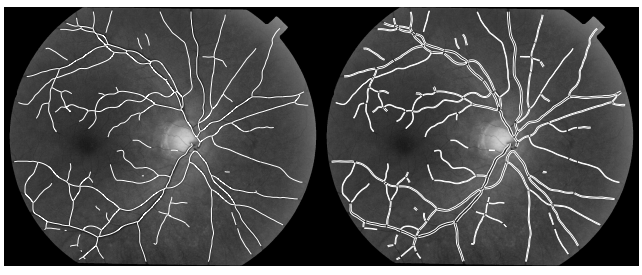

Figure (3.2). *(a)Example of estimated vessel axis networks and (b)estimated vessel diameters of an image from our dataset.*

The rationale of the following vessel tracking step is to consider the im-

age as a weighted un-oriented sparse graph, where each node represents a pixel, and to determine minimum-cost connections on this graph connecting the seed points previously found (Fig.3.2a). The graph arches describe the 8-adjacency among pixels in the image, and the cost of a single arch is function of the gray level of the pixels it connects. Vessels are minimum cost paths connecting remote nodes: in order to find them, a novel graph search algorithm was implemented [15]. This formulation allows a robust vessel axis extraction with respect to possible false positive seeds, at the same time keeping the algorithm computational requirement low.

Diameter extraction (Fig.3.2b) is accomplished via self-correcting scale fast-adaptive matched filters [23]. Cross section vessel profiles are extracted along every branch of the vessel network, orthogonally to the axis direction. They are then preprocessed with a mono-dimensional shift-invariant Gaussian filter, to reduce noise. For each profile, a preliminary vessel width estimation is performed, in order to estimate the kernel scale for the mono-dimensional filtering. Caliber measurements that appear to be non consistent are fixed either by changing the matched filter scale or by forcing them to a trustworthy value if a reliable diameter cannot be found. This approach allows a robust vessel border detection, even in the presence of both intra- and inter-image luminosity and contrast variability, inter-image quality and acquisition-modality dissimilarity.

3.2 From the segmented vascular image to the vessel structures

The postprocessing algorithms assume that the segmentation is provided as a set of vascular structures, described by the quadruple:

$$v_i = (x_i, y_i, \theta_i, c_i) \tag{3.1}$$

whose elements represent respectively the coordinates of vessel center-point (x_i, y_i), the vessel caliber c_i and vessel direction θ_i at that point.

If the global approach, instead of the tracking one, is used to segment the vessel network, a further step is required to pass from a segmented binary

image vessel-no vessel to the vessel structures. In order to achieve this goal, we firstly applied the skeletonisation morphological operation to the binary image (Fig. 3.3a on the left). After that, the leaves of the skeleton graph are identified and as well as the internal nodes. The arches connecting the leaves to the internal nodes are deleted from the graph and identified as vessel centerlines (Fig. 3.3a at center). The remaining graph is split where the previous internal nodes were present and at their place 2 new leaves are created. The process is iterated until no more internal nodes are present and finally the disconnected vessels centerlines are obtained (Fig. 3.3a on the right), nevertheless their identification via the skeletonisation process has not been accurately performed (the black dash line in fig. 3.3b). For each sample the refinement of the vessel centerline detection, follows: lines with different angulation are centered at that sample with the 2 ends positioned at the two vessel edges, the shortest is chosen and the new sample is positioned in the mean point of that line 3.3b. Finally the new centerlines samples are interpolated with a spline and the diameter is determined on sections transversal to the vessel centerlines as the distance between the two edges.

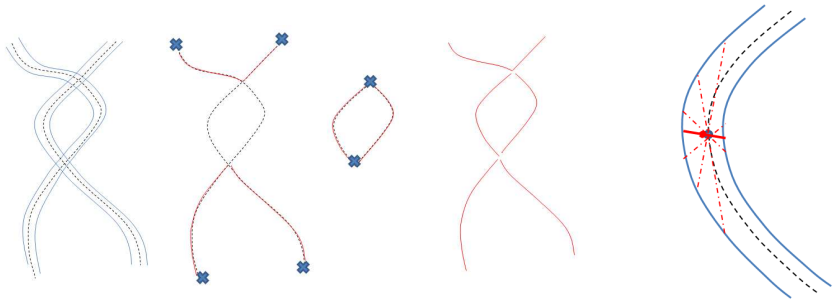

Figure (3.3). *a) From the skeleton to the disconnected vessels centerlines. b) Refinement of the estimated vessel centerline.*

3.3 The false vessels detection

3.3.1 Introduction

A reliable vessel extraction is a prerequisite for subsequent retinal image analysis. All the algorithms presented in the first chapter, even the most accurate, are not able to provide a perfect segmentation and the number of errors increases when poor quality images or images with pathologies need to be analyzed. In these situations the tracking techniques often present a high rate of false positives. Type I errors can be generated by choroidal vessels running below the retina producing ghost paths through the partially opaque retinal tissue, or by vessel-like structures caused by hemorrhages or exhudates, or by random paths on the fundus pigmentation, or by the retina and optic disk boundaries. The figure 3.4 shows in 3.4a an image belonging to the public database STARE and in 3.4b the relative vessels segmentation publicly available provided by a matched filter using a probing technique (Hoover et al [17]): the high number of false positives is in this case related to the patient's pathological state. Figures 3.4c and 3.4d show respectively the true positive and the false positive vessel pixels. The distinction is based on the hand labeled vessel network ground truth provided by Adam Hoover: a sensitivity of 0.55 and a positive predictive value of 0.67 are measured (the specificity is in this case poorly informative because of the high number of background pixels).

The importance of a postprocessing step for the false positive vessels detection is often reported in literature, for example by Salem et al. [24], who propose a "vesselness" measure based on the eigenvectors and eigenvalues of the image Hessian matrix and finally report that they are investigating on a postprocessing step to reduce the false positive rate. Despite the wide and important application of this final step, just Grisan et al. [25] proposed a postprocessing algorithm to distinguish true and false vessels, based on a model of the vessel considering the average geometric and grayscale properties along the full trajectory of the vessel itself. They proposed six models of the vessel with a different grade of detail and with a number of features varying from 4 to 20: the asymmetric model (respect to the central axis) with

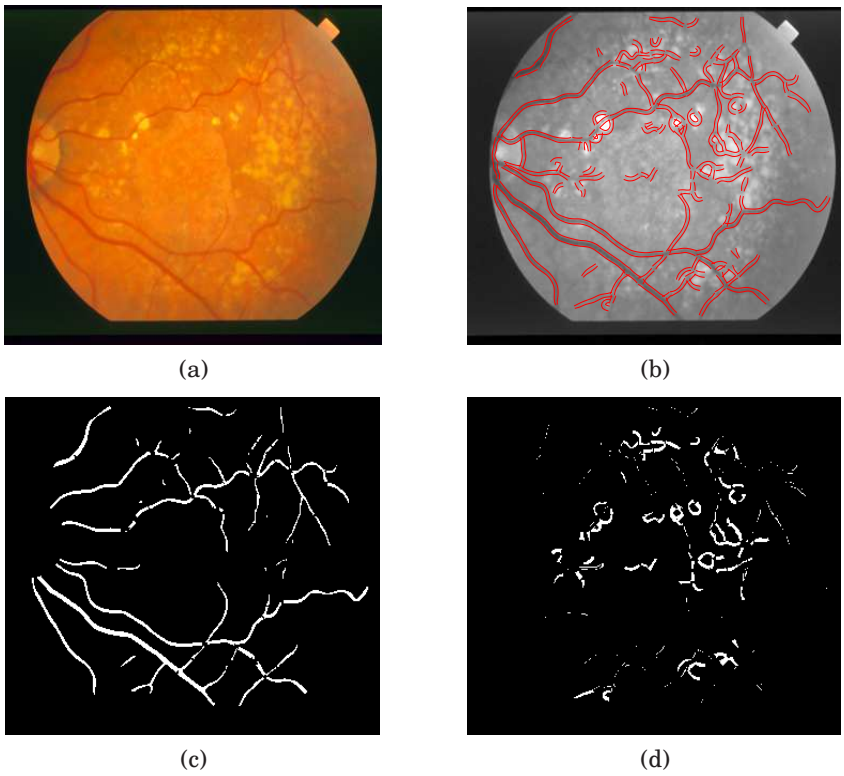

(a) (b)

(c) (d)

Figure (3.4). *The image 0003 belonging to the STARE database. A lot of lesions are present (a). The tracked vessels edges as provided by the algorithm of Hoover et al. (b). True positive (c) and false positive (d) vessel pixels.*

8 features achieved the best results. They used a supervised classification with the Fisher linear discriminant method. The rationale is that once the segmentation has been completed, we can gather information from the full vessel trajectory and solve ambiguities that cannot be fixed during tracking. This is also the rationale of the algorithm we propose: much more information can be provided considering the vessel as a single unit pixels. In the next paragraphs this idea is described in detail.

3.3.2 Materials

Two datasets have been considered for the experiments. The first one has been kindly provided by the Moorfields Eye Hospital of London and it is composed of 24 images from Mongolian diabetic people, including cases without retinopathy lesions as well as pathological ones with exhudates, cotton spots and hemorrhages. 10 images have been used as training set, 14 for the testing set. They have been acquired digitally, with a field of view of 50^0 and a resolution of 3888*2592 pixels. The segmentation has been obtained using the tracking method proposed by our group in [15] and the ground truth has been created indicating the false vessels in each image. Not the single pixels have been evaluated as true or false in accordance with the output of algorithm: it just says which vessels and not which pixels have been wrongly detected. If just a part of the vessel is really a vessel and the other is false, it is graded as right if at least half of the central line pixels are real true pixels. The results are provided both in terms of vessels and in terms of pixels, because with the first way we can appreciate which is the performance of the algorithm, with the second the actual consequences: has a stronger effect discarding or including a long vessel than considering a small vessel. Vessels inside the optic disk have not been considered by the algorithm because their appearance is often very far from the usual one (vessels are very close and cross each others) and moreover they are not useful for the diagnostic parameters estimation.

The second dataset is the public dataset STARE. Images have been acquired as slides and then digitized. The field of view is 35^0 and resolution is 605*700 pixels. Ten of the images are of patients with no pathology (normals), the other ten contain pathology that obscures or confuses the blood vessel ap-

pearance in varying portions of the image (abnormals). The reason why this dataset have been used is threefold: it is a public dataset and also the original segmentation is public, so our results can be compared in the future with others, secondly the abnormal' images present an high rate of false positive vessels and thirdly the manual segmentation (ground truth) by an expert is provided. Since both the automatic segmentation and the ground truth are binary images, they needed to be converted into vessels structures before being analyzed by the false vessels algorithm: the procedure of skeletonisation presented in the previous chapter has been applied. The same rules of the first dataset have been used for the results calculation.

3.3.3 Methods

The rationale of the algorithm proposed here is that a true vessel has a diameter nearly constant and considering image sections transversal to the central axis, centered on it and slightly wider than the vessel's max diameter, their intensity profile shape is nearly symmetrical with respect to the central axis. This idea has been found to be more true if instead of the image intensity another feature is analyzed: a fuzzy-C-mean classificator is applied to the intensity profile of each transversal section in order to distinguish vessel pixels from background pixels and the new feature for each section is the resulting probability profile. In particular for each profile a monodimensional bilateral filter is applied in order to reduce the small intensity variation inside the vessel and to preserve the step between the vessel and the background: this in the case in particular of vessels with a central reflex. In image 3.5 a true (3.5a) and a false (3.5b) vessel and their fuzzy-C-mean probability profiles (3.5c and 3.5d) for consecutive transversal sections are compared: the true vessel has a shape almost symmetrical to the central axis and a diameter almost constant, the opposite happens for the false vessel.

In order to infer where the vessel's edges are on the basis of each probability profile, an empirical threshold of 0.5 has been used to classify between vessel and background pixels, resulting in a binary vector. All the binary vectors corresponding to consecutive sections are then joined together to form a binary image (3.5e and 3.5f on the left). The algorithm then delete the pixels

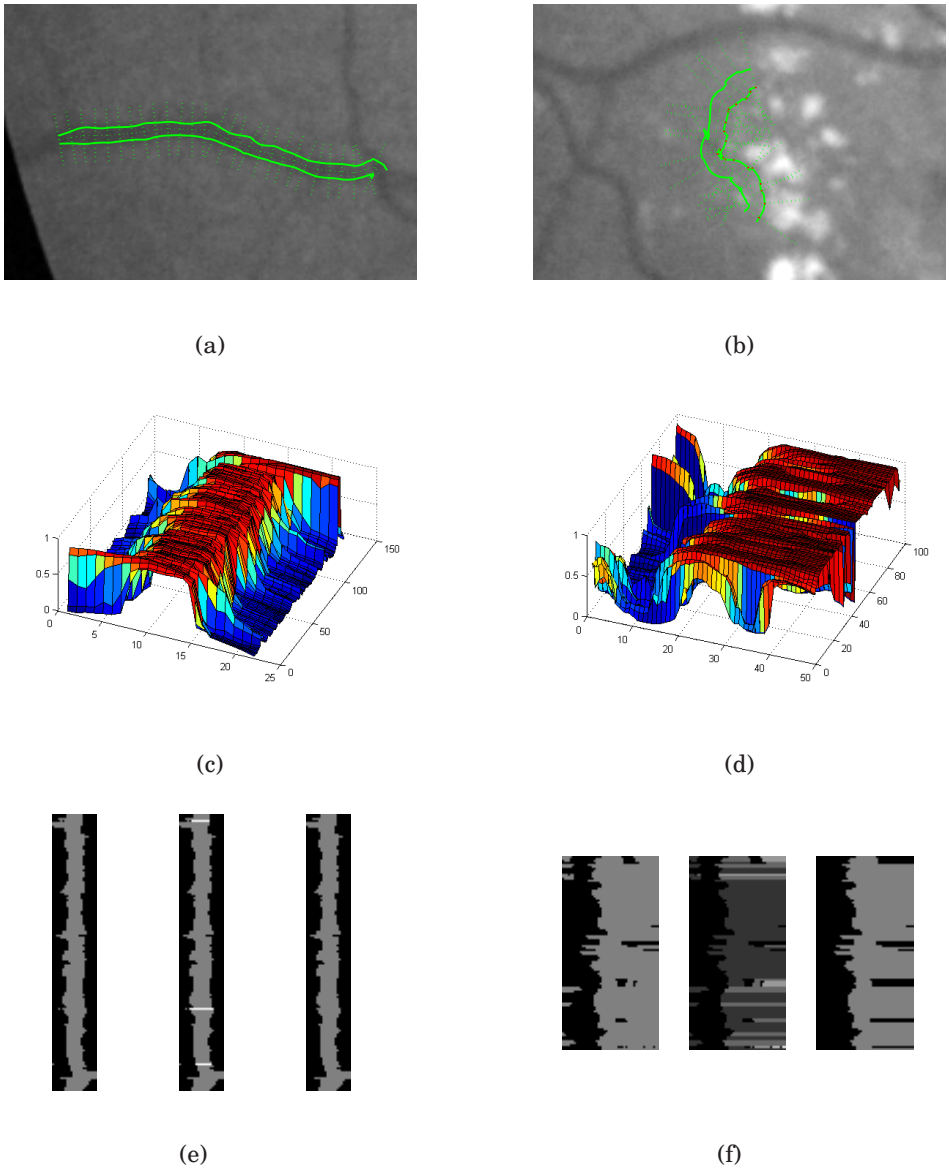

Figure (3.5). *The different behavior of a true (left) and a false (right) vessel. c-d)The FCM probability classification profiles: a uniform and symmetrical distribution can be seen only for the true vessel. e-f on the left) The binary images obtained from the FCM profiles after the thresholding. e and f on the right) The "refined" binary image after having removed the connected components of pixels supposed to not belong to the vessel analyzed but to other close dark regions.*

classified as vessel's if they are supposed to not belong to the vessel analyzed but to other close vessels or noise. This step is performed analyzing again each row separately and identifying the connected components (3.5e and 3.5f at the center): if they are two or more, all the pixels on the left of the last step from 0 to 1 are considered as background pixels as well as all the pixels on the right of the first step from 1 to 0, resulting in a connected component for each row (3.5e and 3.5f on the right). Sometimes two connected components are considered instead of just one in order to segment properly also vessels with a strong central reflex not removed by the bilateral filter. The way to recognize this case will be discussed at the end of the paragraph.

Once the final binary image is obtained, it is possible to notice that a true vessel has a shape almost symmetrical to the center of the x-axis (corresponding to the vessel centerline) and the diameter is nearly constant along the y-axis, i. e. each edge (the left and the right step, respectively from 0 to 1 and from 1 to 0) at different y-coordinates comes at nearly the same x-coordinates. On the contrary in false vessels the two edges come at different x-coordinates (in the example this behavior is more evident for the right edge). In the next steps in order to distinguish between these two behaviors, the x-coordinates distribution of each edge is analyzed to understand if it can be considered a realization of a unique value, i.e. if they refer to the same x true value where the real edge is. Supposing, without loss of generality, that the measure errors (that it the distance between the x_i coordinate and the true value $\bar{x}$) come from a gaussian distribution and that they are small comparing to the vessel diameter, the algorithm tries to understand if the x_i coordinates come from a gaussian distribution and if this distribution has a small standard deviation or not. Therefore the x-data are firstly fitted with a unimodal gaussian mixture model and the estimate of the sigma parameter is used to identify some false edges:

$$if \;\; \sigma^1 < th_\sigma \Rightarrow edge \;\; FALSE \tag{3.2}$$

The th_σ value have been set using the training dataset.

If a vessel has at least one edge identified as false, it is considered as false and deleted, otherwise it is submitted to a further validation based on

the idea that the x-data of a false edge are sometimes fitted better with the bimodal distribution instead of the monomodal one. It can be easily understood looking for example at 3.5b and at 3.5d. If a vessel edge is identified where there is a strong intensity step as in the case of bright lesions, often the segmentation algorithm (especially in the case of a tracking algorithm) tries to proceed the vessel edges beyond the lesion and for a while the vessel is found in correspondence of noise pixels just slightly darker than the the background. In the situation represented in 3.5b and 3.5d the fuzzy C-mean in some sections identifies a vessel where there is not the lesion and in others it identifies a lot of vessel pixels (even if they are not), also until the end of the ROI considered, because no meaningful intensity difference is noticed among them, in other words for some sections the right edge is detected where the lesion starts, for others at the ROI boundaries or close to them (3.5f at the right side).

Therefore at this point the algorithm fits the x-data also with the double gaussian distribution model, then it compares the Akaike index and the parameters estimates between the two models in order to choose the best one: in the case of the best fit with a single gaussian distribution, the edge is classified as true, otherwise as false (the gaussian mixture models have been adopted and the estimates are performed with the Expectation Maximization method). A vessel is identified as false if, as before, at least one edge has been identified as false.

In mathematical terms we are assuming that x_i, $1 \leq i \leq n$ (n is the number of rows of the binary image) are drawn from a pdf $p(x|\theta)$:

$$p(x|\theta) = \sum_{j=1}^{J} \pi_j \Theta_j(x - \theta) \tag{3.3}$$

with $J = 1|J = 2$ and where

$$\Theta_j(x) = \frac{1}{\sqrt{2\pi\sigma_j}} \exp - \frac{x^2}{2{\sigma_j}^2} \tag{3.4}$$

and with the EM method we want to estimate $\hat{x} = \hat{\theta}$.

In the training phase we noticed that just the the Akaike index was not able

to classify the true and the false vessels, in particular the algorithm was too much sensitive to false vessels. So other features were included in our feature vector, in particular the algorithm considers the parameter estimates deriving from the fit with the double gaussians and the Akaike indexes obtaining the feature vector: $\overline{v} = ({\pi_1}^2, {\pi_2}^2, {\sigma_1}^2, {\sigma_2}^2, {\theta_1}^2, {\theta_1}^2, AIC^2, AIC^1)$, where the apex indicates the number of gaussian components J. An edge is defined as false if the Akaike index for $J = 2$ is much smaller than the Akaike index for $J = 1$ and the two components are easily separable and they have a comparable amplitude:

$$AIC(J = 2) < AIC(J = 1) + th_{AIC} \tag{3.5}$$

$$\frac{{\pi_1}^2}{{\pi_2}^2} < th_\pi \quad ({\pi_2}^2 > {\pi_1}^2) \tag{3.6}$$

$$|{\theta_1}^2 - {\theta_2}^2| > th_\theta \tag{3.7}$$

$$\max {\sigma_1}^2, {\sigma_2}^2 < th_{\sigma 2} \tag{3.8}$$

We said before that the binary images vessel-no vessel in 3.5f and 3.5e on the right have been obtained from those on the left considering for each row just a single connected component and we also said that sometimes the connected components counted are two. It happens when the EM algorithm for the monomodal gaussian mixture model does not converge, because it alternates between two local minimums. This is the case when it is possible to see two well defined x-values where the edge should be present, that is almost half of x-coordinates fall at the same value and almost the other half of x-coordinates fall at another value enough far from the first one. This behavior usually is recognizable when a vessel has for a while a very strong central reflex: in this case the real edges can be misunderstood with the spurious edges formed by the central wire. The two connected components allow two consider for the false vessel detection just the external true edges (3.6).

Finally also bifurcations and crossings of the vessel with another vessel are managed by the algorithm, because they usually involve just a small part of the vessel (where the branch starts or where the two vessels crossing appear attached). In this way the x-coordinates distribution of the edge is not significantly influenced and if the bimodal gaussian distribution is con-

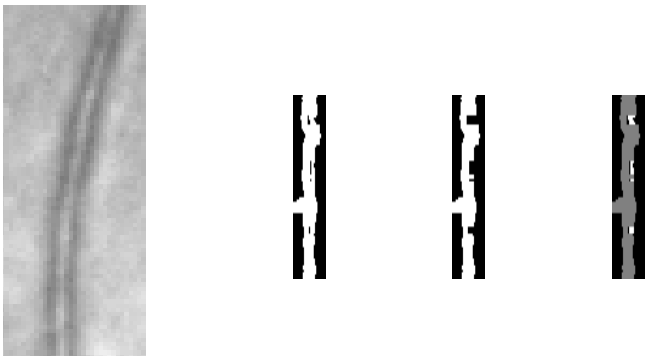

(a) (b) (c) (d)

Figure (3.6). *Because of the central reflex of the true vessel in a), the process "refinement" of the binary FCM image (b) discards some correct pixels (c). Exploiting the information about the non-convergence of the EM algorithm, also these pixels are finally considered (d)*

Dataset	w_{th}	Sens(v)	TPV(v)	Sens(v) ([25])	TPV(v) ([25])
MONGOLIA (TRAINING)	0	0.83	0.11	0.80	0.96
	1	0.57	0.29		
MONGOLIA (TESTING)	0	0.77	0.06	0.62	0.97
	1	0.30	0.11		

Table (3.1). *Results of the method by Giani et al. applied on our dataset*

sidered, the criteria to find a false edge expressed in 3.6-3.8 should not be satisfied.

3.3.4 Results

First of all in table 3.1 the results of the algorithm by Giani et al. [25] as sensitivity and True Positive Value (rate of real false vessel among the positives), applied on our dataset (the testing and the training) have been reported for two significant values of the tuning parameter w_{th}. The indexes have been calculated considering the vessels and not the pixels. The not excellent results induce us to develop the new false vessels detection algorithm.

Results on the Mongolia dataset of the proposed method for different val-

ues of the thresholding parameter th_σ are reported in table 3.2 (both in terms of vessels and pixels). The values have been calculated both considering the average among the images and considering together all the vessels and pixels in all the images ("all" in table). The close values of the "all" indexes and the "mean" indexes and the show that all the algorithm in all the images (the normal and the pathological ones) has a similar behavior. The ROC curve (calculating with "all" the images together) is illustrated in Fig. 3.7. The Area Under the Curve (AUC) is very high (0.94 for the training set and 0.90 for the testing one) indicating a very good performance of the algorithm.

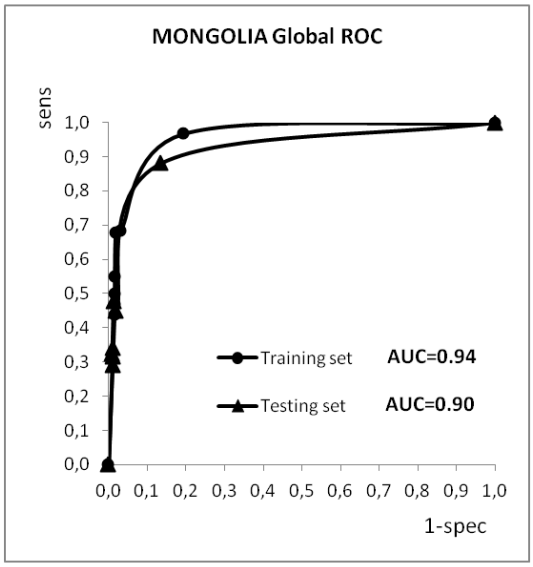

Figure (3.7). *The ROC curve of the false vessels algorithm for the Mongolia dataset*

Results on the STARE database are reported in table 3.3 and the corresponding ROC curves are plotted in Fig. 3.8. The average ROC has an area under the curve of 0.72, suggesting good performance, even not so important as in the Mongolia dataset. It should be said that the 2 datasets have very different features (firstly in FoV and dimension) and the method is unsupervised, therefore the results also for the STARE database can be considered as good ones. Moreover it is interesting to notice (Fig. 3.8b) that the method works in the same way in images with a lot of false vessels (because of the unhealthy state of the patient) and in good quality images where the false

Dataset	th_σ		Sens(px)	Spec(px)	TPV(px)	Sens(v)	Spec(v)	TPV(v)	AUC
MONGOLIA (TRAINING)	0.1	mean	0.86	0.77	0.15	0.87	0.52	0.17	
		std dev	0.33	0.08	0.15	0.31	0.10	0.14	
		all	0.97	0.81	0.21	0.98	0.51	0.22	
	0.4	mean	0.69	0.94	0.40	0.74	0.75	0.24	
		std dev	0.35	0.04	0.25	0.30	0.10	0.17	
		all	0.69	0.97	0.53	0.83	0.75	0.32	
	0.7	mean	0.62	0.96	0.42	0.67	0.84	0.26	
		std dev	0.36	0.01	0.27	0.33	0.06	0.21	
		all	0.68	0.98	0.46	0.79	0.84	0.30	
	1.0	mean	0.66	0.97	0.53	0.61	0.87	0.30	all
		std dev	0.33	0.03	0.31	0.26	0.07	0.20	0.94
		all	0.55	0.98	0.63	0.66	0.86	0.40	
	1.3	mean	0.56	0.97	0.52	0.57	0.87	0.31	
		std dev	0.32	0.02	0.31	0.28	0.07	0.21	
		all	0.50	0.98	0.62	0.61	0.86	0.40	
	1.6	mean	0.55	0.97	0.51	0.57	0.89	0.34	
		std dev	0.33	0.02	0.31	0.27	0.06	0.24	
		all	0.47	0.98	0.60	0.58	0.88	0.42	
	1.9	mean	0.53	0.97	0.51	0.55	0.9	0.35	
		std dev	0.31	0.02	0.31	0.27	0.06	0.24	
		all	0.34	0.99	0.66	0.35	0.90	0.26	
MONGOLIA (TESTING)	0.1	mean	0.90	0.83	0.17	0.90	0.54	0.12	
		std dev	0.30	0.07	0.21	0.030	0.12	0.14	
		all	0.88	0.86	0.29	0.97	0.55	0.18	
	0.4	mean	0.68	0.95	0.46	0.62	0.77	0.15	
		std dev	0.37	0.03	0.34	0.30	0.10	0.12	
		all	0.45	0.98	0.59	0.55	0.77	0.20	
	0.7	mean	0.56	0.97	0.44	0.54	0.82	0.16	
		std dev	0.47	0.03	0.42	0.34	0.09	0.16	
		all	0.48	0.99	0.67	0.66	0.80	0.31	
	1.0	mean	0.48	0.97	0.50	0.45	0.86	0.14	all
		std dev	0.45	0.02	0.47	0.37	0.08	0.15	0.90
		all	0.32	0.99	0.71	0.41	0.85	0.23	
	1.3	mean	0.32	0.98	0.33	0.31	0.87	0.13	
		std dev	0.40	0.01	0.43	0.30	0.07	0.15	
		all	0.32	0.99	0.66	0.34	0.87	0.21	
	1.6	mean	0.33	0.98	0.29	0.26	0.88	0.12	
		std dev	0.39	0.02	0.36	0.31	0.07	0.15	
		all	0.29	0.99	0.61	0.31	0.88	0.22	
	1.9	mean	0.32	0.98	0.35	0.27	0.9	0.14	
		std dev	0.41	0.01	0.43	0.31	0.05	0.17	
		all	0.34	0.99	0.66	0.35	0.90	0.26	

Table (3.2). *Results: MONGOLIA dataset*

th_σ		Sens(px)	Spec(px)	TPV(px)	Sens(v)	Spec(v)	TPV(v)	AUC
1	mean	0.92	0.34	0.30	0.97	0.19	0.31	
	std dev	0.07	0.10	0.12	0.03	0.05	0.17	
2	mean	0.82	0.53	0.34	0.93	0.28	0.31	Max
	std dev	0.09	0.09	0.13	0.05	0.05	0.17	0.84
3	mean	0.71	0.64	0.37	0.88	0.34	0.31	
	std dev	0.11	0.08	0.15	0.07	0.04	0.17	
4	mean	0.62	0.71	0.39	0.84	0.37	0.31	
	std dev	0.13	0.07	0.16	0.06	0.04	0.17	
5	mean	0.56	0.75	0.39	0.80	0.39	0.31	Mean
	std dev	0.13	0.07	0.16	0.07	0.04	0.17	0.72
6	mean	0.51	0.78	0.40	0.77	0.41	0.31	
	std dev	0.13	0.07	0.16	0.08	0.04	0.17	
7	mean	0.47	0.80	0.41	0.74	0.42	0.31	
	std dev	0.12	0.07	0.16	0.07	0.04	0.17	
8	mean	0.44	0.82	0.42	0.72	0.43	0.31	Min
	std dev	0.12	0.07	0.17	0.07	0.04	0.17	0.64
9	mean	0.42	0.83	0.42	0.71	0.44	0.31	
	std dev	0.13	0.06	0.18	0.07	0.04	0.17	

Table (3.3). *Results: STARE dataset*

vessels are few.

3.4 The optic disc detection

3.4.1 Introduction

The optic disc (OD) is the image of the optic nerve and in fundus images usually appears as a round region brighter than the surrounding. From it, the central retinal artery and vein emerge, to cover, with further branching, most of the retinal region. Locating the OD position in fundus images is quite important for many reasons. Many important retinal pathologies may affect the optic nerve. Since the OD may be easily mistaken for large exudative lesions by image analysis techniques, its detection is also important to exclude it from the set of possible lesions. Moreover, OD detection is fundamental for establishing a frame of reference within the retinal image and is, thus, important for any image analysis application. Once the OD has been identified, other regions of clinical importance can be determined. This is the case of the fovea or macula, as discussed later. The detection of OD position is

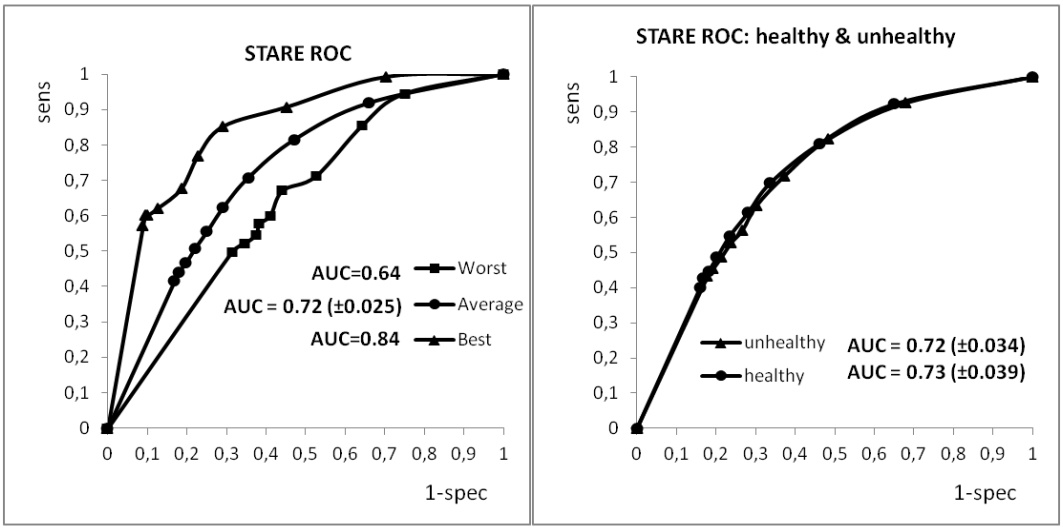

(a) (b)

Figure (3.8). *The ROC curve of the false vessels algorithm for the STARE dataset. a) The average, the best and the worst ROC curves among images from the STARE dataset. b) The average ROC curves for the subsets of "unhealthy" (with lots of false vessels) and "healthy" images: no difference is visible*

also a prerequisite for the computation of some important diagnostic indexes for hypertensive/sclerotic retinopathy based on vasculature, such as central retinal artery equivalent (CRAE) and central retinal vein equivalent (CRVE), because they are estimated in the circular ROI centered at the optic disc and comprised between 2 and 3 its radius. OD detection is also important for the spatial calibration of the image, which can be performed considering the distance between the optic disc center and the fovea as 4.5 mm or considering the OD radius which can be estimated of 1850 μm. Finally the determination of its position is used here to estimate the orientation of the flux inside vessels, a prerequisite for our own procedure to reconstruct the vascular tree, as discussed at the end of this chapter.

The OD localization methods can be classified into two main categories, *appearance-based* methods and *model-based* methods. Appearance-based methods identify the location of the OD as the location of the brightest round object in the retinal image. These methods include techniques such as intensity thresholding [26], highest average variation (in the optic disc there are the dark blood vessels) [27], matched spatial filter, principle component analysis (e.g. Li and Chutatape [28] projected a new image to the disc space specified by the eigenvectors of the training images). Recently Duanggate et al. [29] proposed a parameter free method that detects the OD analyzing the bright blobs by means of three descriptors. Finally the morphological operators [30] and the Circular Hough Transform [31] have been also used. Sekhar et al. detect the optic disc by finding the brightest region within the image. The size of the OD is calculated using morphological operators. The Circular Hough Transform is then applied to the gradient image to detect the contour and the center of the OD [31]. Qureshi et al. [32] combined a set of appearance-based methods obtaining results better than each single method. Although the appearance-based methods are simple and have high success rates in normal images, they fail to correctly localize the OD in diseased retinal images, where the lesions may have similar appearance properties to the OD 3.9a and 3.9b. Model-based methods usually rely upon extracting and analyzing the structure of the retinal vessels and defining the location of the OD as the point where all the retinal vessels originate ([33], [34] and [35]). Techniques such as geometrical models [35], convergence of vasculature [33], and

vessel's direction matched filter [34] have a relatively high success rate in diseased images, but they are computationally very expensive because they require segmentation of the retinal vessels as an initial step of the localization process. Nevertheless, if the OD detection is just a step within a global analysis including also the vascular part, as it is in the context of this thesis, the drawback of the computational time does not exist. The major limitation of the model approach is that it allows to detect the optic disc center but not its radius, which is important for example in the definition of the ROI for the AVR computation or in the image calibration. Another limit is the accuracy of the OD center estimation, because usually the vessels originate not exactly at the optic disc center (as it can be seen in 3.9c), so a further and more accurate analysis based on the optic disc appearance is often needed. The solution we propose here is combines the benefits of the appearance-based methods and the model-based methods.

The papers mentioned above present results on different datasets, sometimes on public datasets such as DRIVE (Digital Retinal Image for Vessel Extraction [36]) or STARE, sometimes on private images. Moreover a public dataset where the optic disc detection has been manually provided by an expert, does not exist and thus evaluations about intra e intergraders variability have not been performed yet. It makes quite difficult to compare the algorithm's performance, as the optic disc boundary is often blurred and easily confused with the inner neuroretinal rim or the outer scleral ring 3.10. The collaboration with the Reading Center of the Moorfields Eye hospital allowed me to obtain a manual segmentation of the optic disc by an expert and a second assessment by a another expert. These reference data will be soon made publicly available on the web.

3.4.2 Methods

The method proposed here is a refinement of the method previously developed by our research group and based on the double parabolic vessels model [35] with a local analysis of edges detection followed by the Circular Hough Transform (CHT).

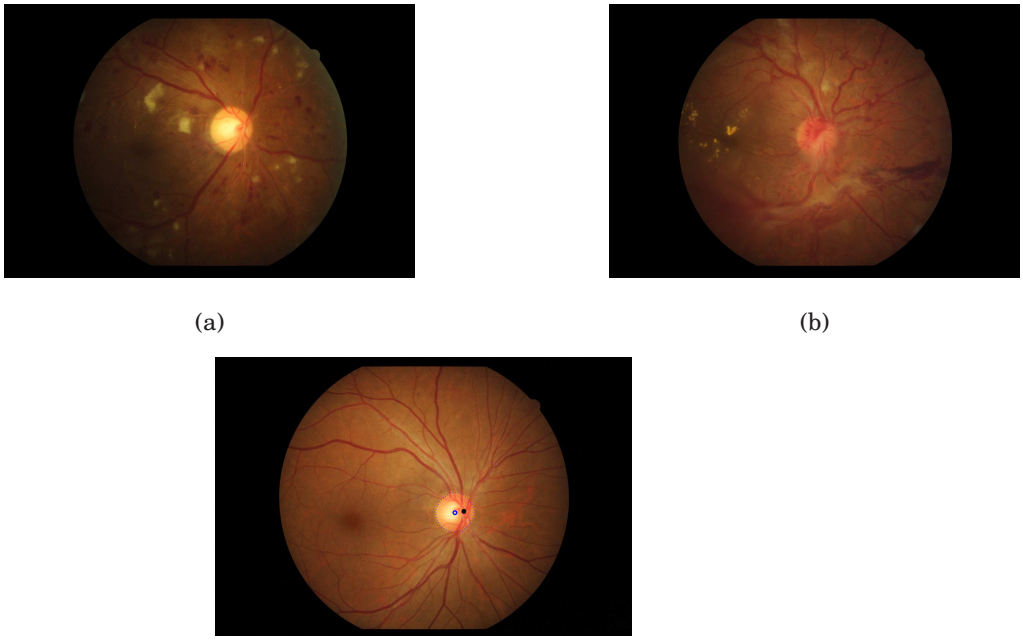

(a) (b)

(c)

Figure (3.9). *The appearance-based methods do not work properly when lesions have appearance properties similar to the OD (a and b). On the contrary a limit of the model based methods is the not high accuracy because the OD center is identified where vessels converge*

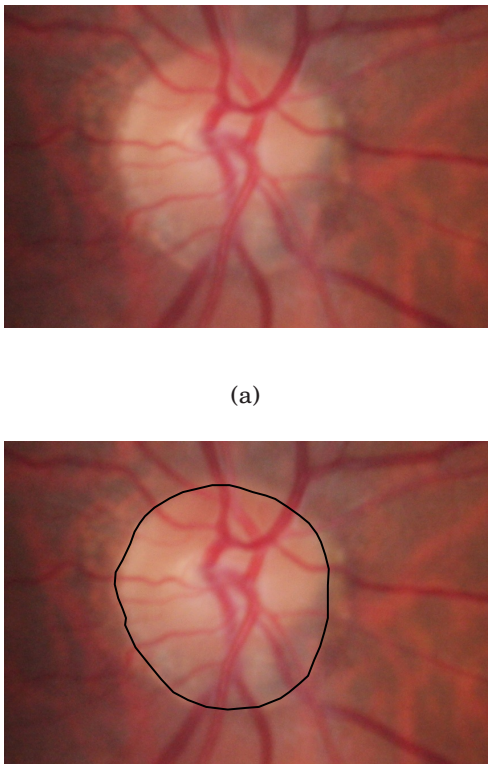

(a)

(b)

Figure (3.10). *An image of the dataset with not well-defined optic disc edge (a) and its ground truth segmentation provided by the grader (b).*

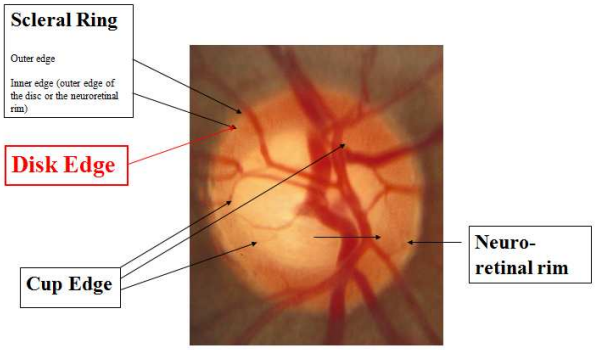

Figure (3.11). *The optic disc edge has not to be confused with the inner cup edge and with the outer scleral ring edge. Even if in this image the scleral ring is thin a wrong optic disc segmentation including it, would cause a not trivial error.*

The geometrical model

The geometrical model of the vessels direction requires the definition on the whole image of a function

$$\theta^{mod}(x, y, \mathbf{p}), \quad -\pi/2 \leq \theta^{mod} \leq \pi/2 \tag{3.9}$$

which represents the preferential direction in the image of a vessel present at point (x,y). Vector **p** is the set of parameters defining the model and its position and includes the OD coordinates. By visual inspection of retinal fundus images (see a representative example in Fig. 3.12, it appears that a common vascular pattern is present in all images:

the main vessels originate from the OD and follow a specific course that can be geometrically modeled as two parabolas, with a common vertex inside the OD. The definition of the directional model can, therefore, be based on this assumption. If we assume a Cartesian coordinate system centered at the optic disc, these parabolas can be described as the geometrical locus Γ

$$\Gamma = (x, y) : a * y^2 = |x| \tag{3.10}$$

where a is the parameter governing the aperture of the parabolas.

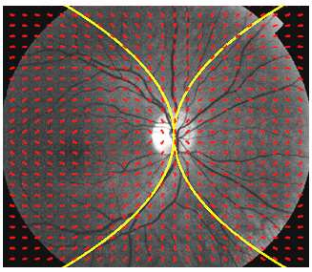

Figure (3.12). *The vessels parabolic model*

For a generic point (x,y) belonging to locus Γ, i.e., on the parabola, the preferential vessel direction is tangent to the parabolas themselves and can be expressed by:

$$\tan(\theta_{\Gamma}^{mod}(x,y,\mathbf{p})) = sgn(x) * sgn(y) * \frac{1}{2 * a * \sqrt{(\frac{|x|}{a})}} \tag{3.11}$$

Γ implicitly divides every quadrant in two areas: the internal area (with respect to the convexity of the parabola) and the external area. Anatomical knowledge indicates that vessels bifurcate when moving away from the OD, and branch vessels tend to diverge from the main vessel. In particular, vessels inside the parabolas quickly bend toward the macula in the temporal region (left-hand side in Fig. 3.12), whereas in the nasal region this inward deflection happens at a much slower rate (right-hand side in Fig. 3.12). The tangent equation 3.11 was, thus, extended to accommodate points outside by adding a correction term d:

$$d(x,y,\mathbf{p}) = \frac{y - sgn(y) * \frac{1}{2*a*\sqrt{(\frac{|x|}{a})}}}{c(x)} \tag{3.12}$$

$$c(x,y) = \frac{c_1}{1+\exp -x} + \frac{c_2}{1+\exp x} \qquad c_1 > 0, \;\; c_2 < 0 \tag{3.13}$$

The numerator of 3.12 is zero for a point belonging to horizontal parabola axis, whereas for a point outside its absolute value increases in a way proportional to the vertical distance between the point and the parabola axis. This

increment in tangent magnitude is modulated by equation 3.13, which expresses the rate of divergence of the direction at any given coordinate. Given a generic origin for the Cartesian coordinates system in use (e.g., upper-left corner in the image), in order for the parabolas to be centered at the coordinates of the OD center, as shown in Fig.3.12, a translation transformation had to be applied to the model:

$$x^* = x - xod$$
$$y^* = y - yod$$

The complete model for vessel direction θ^{mod} at any point (x,y) in the image is given by the following equation:

$$\begin{aligned}\theta^{mod}(x,y,\mathbf{p}) &= \arctan\left(\theta_{\Gamma}^{mod}(x^*,x^*,\mathbf{p}) + d(x^*,y^*,\mathbf{p})\right) \\ &= \arctan\left(sgn(x-xod) * sgn(y-yod) * \frac{1}{2*a*\sqrt{(\frac{|x-xod|}{a})}} + \right. \\ &\quad \left. + \frac{(y-yod) - sgn(y-yod) * \frac{1}{2*a*\sqrt{(\frac{|x-xod|}{a})}}}{c(x-xod)}\right)\end{aligned}$$

Fig.3.12 shows an example of one such model overlapped to the retinal image.

The data of our model are the vessel directions θ_i measured at points (x_i, y_i) $i = 1, .., n$, belonging to the vascular structure. As stated before, we assume, without loss of generality, that the detected vascular tree is represented by the set of quadruplets:

$$v_i = (x_i, y_i, \theta_i, c_i) \tag{3.14}$$

whose elements represent respectively the coordinates of i_{th} vessel centerpoint (x_i, y_i), the vessel caliber c_i and vessel direction θ_i at that point. The identification of model parameters was performed via the minimization of the weighted residual sum of squares and the simulated annealing (SA) optimization algorithm has been adopted to this purpose, because less sensitive to the local minima than gradient methods. Fig.3.13 represents, e.g., a plot of RSS as a function of parameters xod and yod only.

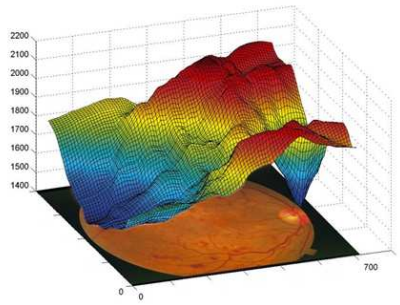

Figure (3.13). *The residual sum of squares of the geometrical model fit as a function of parameters xod and yod*

In order to overcome the stochastic nature of SA algorithm, several optimization runs were performed, starting the procedure from different points in the parameter space, and the final RSS values were compared to select the smallest one. A number of nine runs for each image proved to be suitable in our dataset.

The Circular Hough Transform

Once the geometrical model method provided a rough estimate of the optic disc center, it undergoes a refinement based on edge detection and CHT, which allow to estimate the optic disc diameter as well.

Firstly a square ROI centered at the previously estimated OD center is determined, with size proportional to a first appoximate estimation of the OD diameter based on the anatomical information that the average OD diameter is $1850\mu m$ and the average maximum vessel diameter is $125\mu m$. The red channel of the image ROI is considered because at this component the vessels inside the OD are less visible, it is then filtered in order to reduce noise with the median filter, followed by the Wiener filter. This last is a lowpass filter: it uses a pixel-wise adaptive Wiener method based on statistics estimated from a local neighborhood of each pixel in order to clean an intensity image that has been degraded by constant power additive noise. The filtering step

is a fundamental prerequisite for the further edge detection phase, which is performed using the Canny algorithm. The resulting binary image usually is composed by the OD edge and the vessels edges. These latter are easily removed exploiting the vessels segmentation already performed: the vessels binary mask is dilated in order to include also the vessels edges and then it is subtracted from the Canny image, showing now mostly the OD boundaries. After that, some morphological operations are performed, including the removal of small connected components and the dilation of the Canny image. The latter is fundamental for the following application of the CHT because the optic disc shape is usually not a perfect circle, but an ellipse with a low eccentricity and in order for the circle approximation to be true, the dilation of the OD edge is needed. Hence the Hough transform is applied to the "cleaned Canny" image.

The Hough transform is a method for finding shapes in an image. The basic idea behind the Hough transform is to transform the image into a parameter space that is constructed specifically to analytically describe the desired shape. Maxima in this parameter space then correspond to the presence of the desired shape in image space. The circular Hough transform is almost identical to the Hough transform for lines, but uses the parametric form for a circle:

$$(x-a)^2 + (y-b)^2 = r^2 \tag{3.15}$$

where (a, b) is the center of the circle of radius r that passes through (x,y). The Hough space is three dimensional. The gradient image is transformed to a set of 3 parameters, representing the accumulator, its center and its radius. For each feature point, votes are accumulated in an accumulator array for all the parameter combinations. The accumulator will have set of edge points; each edge point contributes a circle of radius r in the accumulation space. The accumulation space has a peak where these contributory circles overlap at the center of the original circle. Because of the heavy computational load of the CHT, a suitable implementation was needed. The estimated radius of the circles detected is stored in an NN matrix with a one-to-one correspondence to the image, the same for the accumulator. Not all the points of the images

are analyzed, resulting in gaps in the accumulator and center matrix, but this problem was easily solved with the fast morphological operation of "closing", which did not affect the performance of the CHT.

3.4.3 Results

The dataset analyzed is composed of 28 high resolution (3888*2592 pixels) images belonging to the Mongolia dataset, including diabetic subjects with or without retinopathy. 5 images contain many lesions or hemorrhages, 14 are centered at the OD, 14 at the fovea. The reference ground truth data of the OD segmentation have been provided by a grader of the Moorfields Eye Hospital. A second grader examined the first grader's segmentation, if he did not agree the image was discarded from the dataset analyzed (this happened for just two images). Since the method proposed is based on the assumption that the optic disc has a circular shape, we wanted to understand how much the errors depend on this assumption. The results have been obtained not just comparing the overlapping areas between the circle detected as the OD and the reference segmentation, but also between the first one and the circle better approximating the reference segmentation. This circle is obtained in two steps: firstly we found the largest almost regular polygon comprised in the reference segmentation (this is obtained via the "opening" morphological operation) and secondly we measured the maximum distance between the vertices of the polygon and its barycenter. This distance equals the radius of the circumscribed circumference, considered as the circumference better approximating the reference optic disc edge. The results are reported in table 3.4. The sensitivity (fraction of pixels inside the true OD really detected as OD pixels) and the true positive value (fraction of correct pixels inside the estimated OD) have been calculated (specificity is not a significant index because of the very lower OD area in comparison to the image area). These indexes have been calculated also comparing to the "circle" better approximating the reference segmentation (Sens.(c) e TPV (c) in table). The median, the average and the standard deviation have been reported. It is possible to notice that the mean and the median are very different, in particular the median is higher than the mean: a sensitivity of 0.95 (0.98) in comparison to 0.71

	Sens.	TPV	Sens.(c)	TPV (c)	$\|\|OD_{man} - OD_{aut}\|\|(\%diag.)$	Inside	Model's error	Improv. After CTH	Time (sec.)
median	0.95	0.81	0.98	0.73	13.17 (1%)				87
mean	0.71	0.61	0.73	0.57	94.99 (8%)	71%	38%	83%	96
std dev	0.40	0.37	0.42	0.36	177.46				37

Table (3.4). *OD results on 28 images.*

(0.73) and a TPV value of 0.81 (0.73) in comparison to 0.61 (0.57). This is due to the "binary" behavior of the algorithm: usually if the first step based on the vessels model provides a good estimation of the OD center (i.e. it does not stop at a local minimum), then the second step of the CHT is applied on a ROI including the real OD. In this case the final estimation in center and radius is very precise (as the median tells). If otherwise the first step fails completely, also the second one fails and a null sensitivity and TPV are calculated. The Euclidean error reported as $\|OD_{man} - OD_{aut}\|$ refers to the distance between the center automatically estimated and the center of the ground truth circle. This index is also evaluated as the percentage of the diagonal of the image in order to make it comparable with indexes from differently sized images. As reported at the "inside" column the percentage of detected optic discs with the center inside the true OD is 71 %. The reason why the algorithm failed is in 38 % of the case to be ascribed to the vessel model method, the others to the partial overlapping of the estimated OD to the true OD. The "Improved after CTH" column indicates that in 83% of the images, the introduction of the CHT as a second step improves the estimation of the OD center of 38 pixels on average (corresponding to about the 46% of the mean OD radius), besides providing the estimation of the OD radius as well.

In fig.3.14 two examples of the resulting OD detection are shown. Also in a image with many bright lesions the algorithm correctly detects the OD (3.14b).

Even if the comparison with other methods is not very significant because different images with different reference ground truth have been used, in table 3.5 the results reported in recent papers are compared with our own: the performance of our algorithm appears to be similar to the other methods'. The computational time refers to a module running on a Intel(R) Core(TM) i5 2.53 GHz processor and implemented in Matlab language.

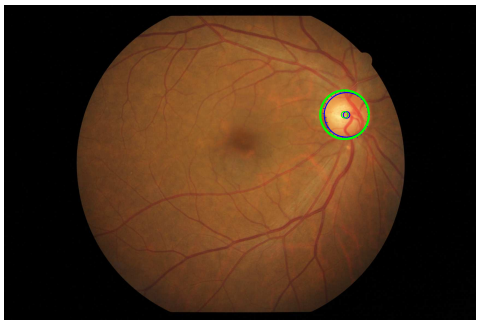

(a)

(b)

Figure (3.14). *The OD automatic detection (in green) on two images belonging to the Mongolia dataset. The ground truth segmentation is shown in blue. The detection is very accurate even if many lesions are present (b).*

Method		Sens.	TPV	Sens.(c)	TPV (c)	$\|\|OD_{man} - OD_{aut}\|\|(\%diag.)$	Inside	Time (sec.)
Qureshi et. al [32]	DRIVE					15.95 (2%)	79 %	
Qureshi et. al [32]	Diaredtb					12.10 (1%)	79 %	
Duanggate et al. (clear OD images) [29]	mean	0.71	0.71					161
Duanggate et al. (faint OD images) [29]	mean	0.53	0.56					223
The proposed method	mean	0.71	0.61	0.73	0.57	94.99(8%)	71%	96
The proposed method	median	0.95	0.81	0.98	0.73	13.17(1%)	71%	87

Table (3.5). *Comparison of our method with the most accurate ones presented in literature*

3.5 The fovea detection

3.5.1 Introduction

The macula is a very important region of the eye because it contains the maximum density of cones (the color receptors of the visual system). In most fundus images, the macula is the darker region of the image, and the central region of the macula is denominated fovea. Anatomically the fovea region is a circle of 0.25 mm of diameter, with its center located two optic disc diameters away from the optic disc center, in the temporal side of the optic nerve (i.e. towards the macula center) 3.15.

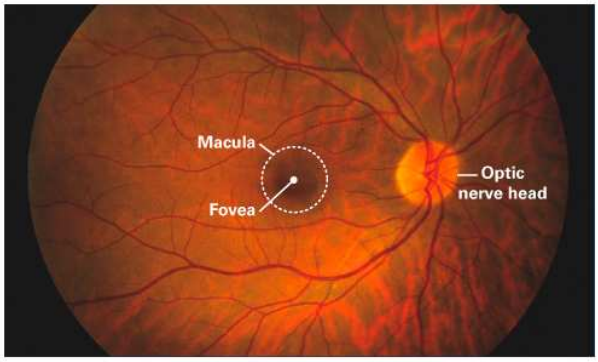

Figure (3.15). *Location of the fovea and the macula*

As described by Ciulla et al. [37], at any time during the progression of Diabetic retinopathy (DR), patients with diabetes can also develop Diabetic Macular Edema (DME). Since the fovea has a very important function in vision, the distance at which lesions are located from it greatly affects their clinical relevance [38]. In particular DME has three severity levels: mild, moderate and severe. In mild DME some retinal thickening or hard exudates usually occur far from the macula center. The moderate DME is characterized by the occurrence of retinal thickening, or by hard exudates in the neighborhood of the macula center. Finally, the severe DME presents retinal thickening or hard exudates involving the macula center. Thus, the accurate detection of the macula center plays an important role in the assessement of the DME.

Other pathologies can affect the fovea and the macula, for example the

Age Macular Degeneration (AMD) and the Macular Telengiectasia (MacTel). In the case of the AMD, with advancing age, the cells of the retinal pigment epithelium become less efficient in performing their tasks for many reasons; the retina can no longer receive its proper nourishment and accumulates waste material, which leads to amorphous deposits termed drusen. The retinal pigment membrane cells slowly degenerate and atrophy, and central vision is lost. This form of disease is called the dry type of age related macular degeneration or geographic atrophy. Alternatively, if the integrity of Bruch's membrane (innermost layer of the choroid) is broken, neovascular complexes from the choroid grow into the subpigment epithelial and subretinal spaces in a process called choroidal neovascularisation. The new blood vessels are leaky, leading to oedema (extravasation of blood and lipid materials), which progressively disrupts visual function. The end result is a dense fibrovascular scar that may involve the entire macular area. This form of disease is called exudative or the wet type of age related macular degeneration.

MacTel is a disorder of the blood vessels which supply the macula. The fovea has no blood vessels at all because they would interfere with central vision. MacTel refers to a curious, very poorly understood condition of the blood vessels around the fovea (juxtafoveal) which become dilated and incompetent. While MacTel does not usually cause total blindness, it commonly causes loss of the central vision, which is required for reading and driving vision, over a period of 10-20 years [39].

The fovea center is also an important landmark fundamental for establishing a frame of reference within the retinal image and among different images, mainly if belonging to the same patient. For example the distance between the OD center and the fovea (usually comprised between 2 and 2.5 times the OD radius and with an average value of $4.5\ mm$) can be exploited to determine a proper estimation of the image magnification (defined as the image height divided by the actual object height), i.e. of the calibration factor ($\mu m/pixel$), important when different images are compared as well as to determine sizes of lesions or hemorrhages within the image. Moreover if images from the same patient are compared, the distance between the fovea and the OD remain constant providing an important reference measure, for comparing images of different kinds, sizes, FoVs or just taken in different moments.

Finally the fovea center and the OD center are fundamental for the method presented in the next paragraphs regarding the vessel map reconstruction: arteriolars come out from the OD and spread out converging again as capillaries towards the fovea (the opposite course for the venulars).

Several approaches for detecting the fovea in retinal images have been proposed in the literature. Sinthanayothin et al. [27] used a fovea template to find the fovea locus in retinal images. This template is an artificial grayscale model of the real fovea region and is obtained using a Gaussian distribution with a fixed standard deviation. Narasimha-Iyer et al. [40], proposed to locate the fovea center using a two-step approach, which is based on the optic disc diameter, a region of interest and an adaptive threshold. Niemeijer et al. [41] used a method based on a cost function as well as a point distribution model to detect and locate the fovea. Li and Chutatape [42] combined the information provided by low intensity pixels (characteristic of the fovea region) and the main vessels arcade, and detected the fovea with a parabola fitting method. Sekhar et al. [31] used the spatial relationship between the optic disc diameter and the fovea region, a region of interest (ROI) is identified. Within this ROI they apply thresholding and the morphological opening operator to identify the fovea center. Recently Welfer et al. [43] exploited again spatial relationship between the optic disc diameter and the fovea region, determining a ROI where they detected fovea candidate regions by using specific morphological filters. With these filters, bright lesions (i.e. hard exudates) and dark lesions (i.e. microhemorrhages or microaneurysms) are removed before finding fovea candidate regions. Afterwards, the center of the darkest candidate region, located below the optic disc center, is selected as the fovea center. These methods have an high rate of success and in some cases a value of 100% has been reported [31, 43]. Usually they have been tested in public datasets such as DRIVE [44], STARE [45], Diaretdb1 [46], where not all the images of each dataset have been considered, because in some cases the fovea is not visually detectable. Nevertheless the images discarded are not always the same, for example for the DRIVE database composed of 40 images, 3 of them were discarded from the testing sets in all the studies, but others (in a number from 1 to 4) are sometimes included and sometimes not, making the comparison difficult. Moreover, and this is a weakness point of

all the methods presented, they refer to different manual ground truth measurements provided by different experts and no studies have been performed to investigate the intra e inter-subject variability in determining the fovea center. Therefore, if every method compares to different ground truth, the results comparison can be just qualitative and approximate. The method here presented has been tested on 29 images from the Mongolia dataset (15 centered at the fovea, 14 centered at the macula, with 5 images in a advanced pathological state) by an expert from the Moorfields Eye Hospital, and this new dataset will be soon made public so every method can be tested on the same reference ground truth. Here we present an algorithm which exploits the usual anatomical information about the distance from the OD center and the fovea center, followed by a filtering phase and an adaptive thresholding step. The novelty of this method is the exploiting of the information of the longest (nearly horizontal) axis of symmetry of the image passing through the OD center and supposed to pass very close to the fovea center.

3.5.2 Methods

The fovea detection is performed here exploiting 2 properties of the image analyzed: its orientation and the chromatic features of the macula.

The "orientation" of the image is here conceived as a pseudo-symmetry of the image. Before defining it, let us introduce some statistical operators are here reminded: they are "central moments" of the image. They provide information about the variability and the distribution of the color intensity within the image.

Given the $I(x, y)$ image, its central moment of orders p and q μ_{pq} is defined as:

$$\mu_{pq} = \sum_x \sum_y (x - \bar{x})^p (y - \bar{y})^q I(x, y) \tag{3.16}$$

where $(\bar{x}, \bar{y})$ are the coordinates of a reference centroid, in our case the OD center.

Moreover we define the $cov[I(x, y)]$ covariance matrix on the image:

$$cov[I(x,y)] = \begin{bmatrix} \mu_{20}^{'} & \mu_{11}^{'} \\ \mu_{11}^{'} & \mu_{02}^{'} \end{bmatrix}$$

$$\begin{aligned} \mu_{20}^{'} &= \mu_{20}/\mu_{00} \\ \mu_{02}^{'} &= \mu_{02}/\mu_{00} \\ \mu_{11}^{'} &= \mu_{11}/\mu_{00} \\ \mu_{00} &= \sum_{x}\sum_{y} I(x,y) \end{aligned}$$

where each moment is normalized with respect to μ_{00}, given by the sum of all the pixels' intensity; μ_{20} and μ_{02} are respectively the variance σ_x^2 and σ_y^2.

The eigenvectors of the covariance matrix correspond to the maximum and the minimum axis of the ellipse associate to the image intensity: the image orientation can be deduced from the angle between the maximum axis and the horizontal direction. It is obtained from the equation:

$$\Theta = \frac{1}{2}\arctan\left(\frac{2\mu_{11}^{'}}{\mu_{02}^{'} - \mu_{20}^{'}}\right) \tag{3.17}$$

Since the central moments have been computed relative to the OD center, Θ is the angle comprised between the horizontal straight line passing through the aforementioned point and the straight line passing in the proximity of the fovea.

Anatomical information suggests that the distance OD center-fovea is about 2-2.5 times the OD diameter. From this, a circular region ROI is drawn centered at the OD and with radius from 1.75 to 2.75 times the OD diameter. Just the right or left half of the ROI is then considered, if respectively the left or the right eye is analyzed. The further analysis is performed only on a small sector of the ROI and using the angle from the horizontal line: the sector is centered at this angle and its edges have an angular distance from it of $\pi/8$. Since the estimation of the central moment is performed with a high accuracy, just a small sector is considered avoiding to consider other dark regions in the image, as hemorrhages or just vessels.

Once the ROI is detected, the fovea center is estimated through a series of filtering and thresholding operations in the following order:

1. adaptive thresholding segmenting the dark regions from the background
2. median filtering
3. filtering with a circular template in order to detect the circular fovea
4. second thresholding to segment the points of larger response to the previous filter
5. the 4-connected region with the centroid closest to the previously estimated "fovea" line is considered

The fovea center is thus positioned in correspondence of the chosen centroid. In Fig. 3.16 the main steps of the fovea segmentation procedure are illustrated: the first filtering step, with in red the "orientation" line,3.16a , the thresholding phase 3.16b and the final result 3.16c. Here the estimated center is plotted in red, the reference in white, the tolerance region used in this study to indicate the "region" of a successful detection (if the red point is inside) is plotted in white and in black the tolerance region used in other studies [41]- [43].

3.5.3 Results

As above, the Euclidean distance has been used for measuring the fovea detection accuracy of our method. Automatically detected fovea centers are considered correct within a distance of 136 pixels from the ground truth (in terms of the Euclidean distance). The idea of using a fixed distance for measuring the fovea detection accuracy has been proposed by Niemeijer et al. [41] and by Welfer et al. [43]. The former used a distance of 50 pixels and images of 768Œ576 pixels, the latter adjusted this distance proportionally to the smallest image size of their dataset. Similarly, we too adapted this distance to our dataset (high resolution images from Mongolian diabetic people), resulting 136 pixels long (black circle in 3.16c). Nevertheless it seemed to us to be too much high and this impression has been confirmed by the graders we are collaborating with, so it has been reduced to 100 pixels. Table 3.6 shows results on our dataset: in 27 images among 29 the fovea have been rightly detected, resulting in a rate of success of 93%. The 2 images where the algorithm failed

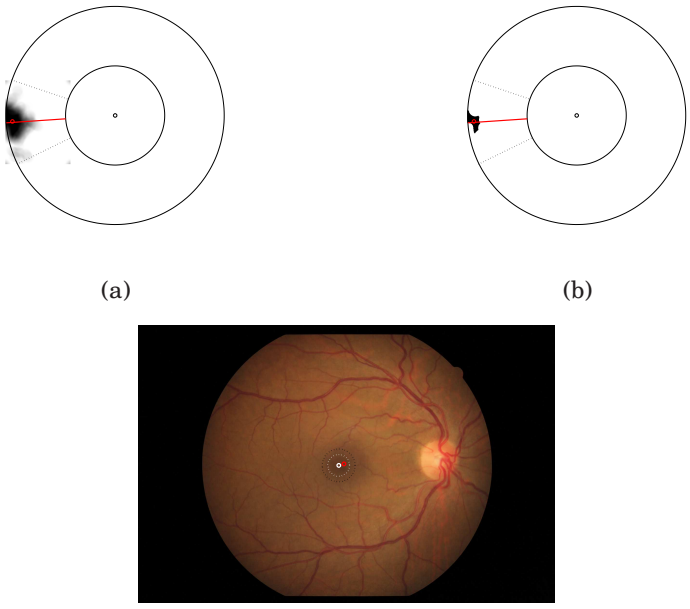

(a) (b)

(c)

Figure (3.16). *The main steps of the fovea segmentation procedure: the first filtering step with in red the "orientation" line (a), the thresholding phase (b) and the final result (c). The white dash circle indicates our tolerance region, the larger black circle indicates the tolerance region used by Niemeijer et al. [41]*

	Mean err.(px)	Median err.(px)	σ err	Success (%)	Mean Time (sec)
without 2 wrong images	30	24	21	93	2

Table (3.6). *Fovea detection results on 29 images from our Mongolian dataset. It will be made soon publicly available on the web.*

	Mean err.(px)	Median err.(px)	σ err	Success (%)	Mean Time (sec)
37 images	33	10	93	95	2
35 images	12	9	17	100	2

Table (3.7). *Fovea detection results on the DRIVE dataset*

are centered at the OD and the fovea is really hardly detectable because it is located in the outer part of the image and the OD is slightly shifted respect to the image center towards the fovea. The mean error is of 30 pixels (about 30% of our success threshold distance) and the median error to 24 pixels (about 24% of our success threshold distance). The average computational time is just 2 sec on a Intel(R) Core(TM) i5 2.53 GHz processor, for a Matlab language.

We tested our method also on the DRIVE dataset to compare with the other algorithms. In this case the ground truth has been provided by myself, using the same protocol used by the expert and considering 2 features: the fovea is usually located at the darkest area inside the macula and the capillaries converge towards its center even if they stop a bit far from it (the fovea is a no-vascular zone). As for the Mongolia dataset, also for the DRIVE dataset the tolerance area has been reduced from 34 [43] to 25 pixels. From the DRIVE database 3 images not including the fovea have been obviously discarded. We report the results obtained by our method both including all the 37 images and discarding 2 images where the fovea is not very visible, at the periphery of the FoV (results reported in the literature included a number of images varying from 34 to 37). In tables 3.7 and 3.8 our results on the DRIVE database are shown. A remarkably high rate of accuracy was achieved, reaching 100% if the 2 images with a hardly detectable fovea are discarded. These results are comparable with the best algorithm presented in literature but with a smaller tolerance region, so even in more restrictive conditions the performance are as high as the best algorithm.

Methods	Rate of success (%)
Sinthanayothin et al. [27]	78.38
Narashima-Iyer et al. [40]	83.78
Sekhar et al. [31]	91.89
Welfer et al. [43]	100
Our method (37 images)	94.59
Our method (35 images)	100

Table (3.8). *Comparison of our results on the DRIVE dataset with other methods*

3.6 The reconstruction of the vessels network: bifurcations and crossings detection

3.6.1 Introduction

The cardiovascular system is a highly branched structure, with the number of blood vessel junctions being in the order of billions. However, contrary to vascular topography being a completely random geometric network, there is evidence to support the concept of an organized geometric structure, to minimize physical properties such as shear stress and work across any vascular network [6]. In 1926, Murray calculated that the most efficient circulation across a vascular network can be achieved if blood flow is proportional to the cubed power of the vessel's radius (known eponymously as Murray's law). Thus, $D_0^x = D_1^x + D_2^x$ where (D_0) is the diameter of the parent vessel, and (D_1 and D_2) are the diameters of the daughter vessels. Theoretical values for the value of X (junctional exponent) approximate to the value of 3 in healthy vascular networks, and deviations from this optimal value reflect a less optimized circulatory network. In addition, the angle subtended between two daughter vessels at a vascular junction has also been found to be associated with an optimal value, approximately 75 degrees. Thus, these parameters serve as measures of optimality of circulatory geometry and can be used to obtain information on the effect of systemic cardiovascular disease on the retinal circulation. The identification of vascular bifurcations is one of the

basic steps in this analysis. Other important diagnostic signs can appear at vessels crossings, for example the Salus' and Gunns' signs (respectively regarding the vein compression and vein deflection). Hence, the detection of crossing points is a step of the diagnostic procedure for many diseases.

The estimation of other diagnostic parameters depends on the detection of these feature points, as the AVR which considers only vessel trunks in a circular region centered at the OD [5], the vessel tortuosity often measured considering the length of the vessel and the distance between the two vessel ends [47] and the vessel axial length suggested to be a diagnostic parameter [48].

These points are also important from a purely image analysis standpoint. If stable, they are valuable as features (i.e., landmarks) for registration, mosaicing, and change detection [49].

More than 40 vascular bifurcations and 20 crossings can be seen in a typical retinal fundus image. Their manual detection by a human observer is a tedious and time consuming process. The existing attempts to automate the detection of feature points can be categorized into 2 classes: those directly applied on the binary image resulting from the vessels segmentation and those considering the vessel structures as defined in 3.14.

The majority of methods belongs to the first category. For example in [50] firstly the skeleton of the vascular tree is obtained from the segmented binary image and then three types of significant points in the skeleton are detected: terminal points, bifurcation points, and crossing points. In a first pass, skeleton pixels with only one neighbor in a 3 x 3 neighborhood are labeled as terminal points and pixels with three neighbors are labeled as candidate bifurcation points. Because vessel crossing points appear in the skeleton as two bifurcation points very close to each other, a second pass is made using a fixed-size circular window centered on the candidate bifurcations, the window diameter is set equal to the largest vessel diameter expected in that particular image. The process fails when:

1. two true bifurcation points are very close and are merged into a crossing point (3.17a)

2. two vessels cross at a very acute angle so that the two candidate bifur-

cation points fall outside the circular window and are, thus, defined as two bifurcation points (3.17b)

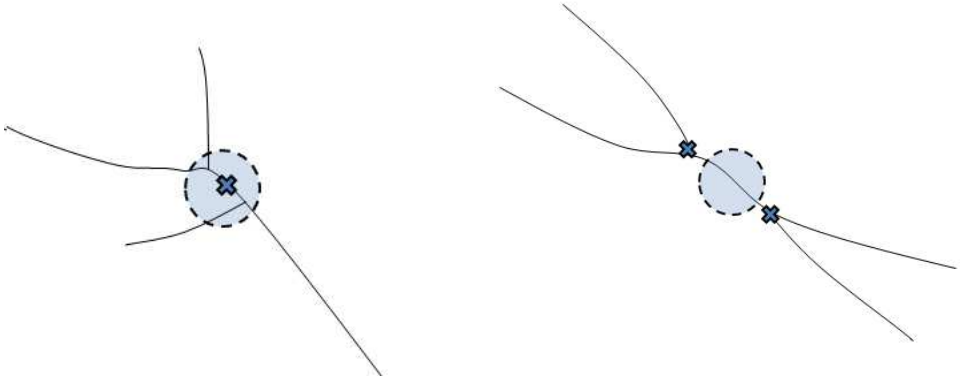

(a) (b)

Figure (3.17). *Two critical situations: in a) two bifurcations are very close and they are wrongly detected as a crossing, on the contrary in b) the vessels cross with very acute angle and two wrong bifurcations are detected*

A solution to this problems has been recently presented by Calvo et al. in [51]. In order to understand if two close feature points are actually a crossing or 2 close bifurcations, they considered circles with different sizes and a vote system to weight the classifications performed with the different radius.

Another method directly applied on the binary segmented image has been recently proposed by Azzopardi et al. [52] dealing only with the bifurcations detection. It does not require the skeletonisation process (hence the problems above indicated are overcome) but it is not a completely automatic method because it needs an initial manual intervention: the user has to identify at least one bifurcation. Such a feature is used to automatically configure a detector that will respond to the same and similar patterns, via the combination of Gabor filter responses to the bifurcation subunits composed by the three vessel arcs connected to the bifurcation node. It reported a very high accuracy on the DRIVE manual segmented images: a recall rate of 98.52% and a precision rate of 95.19%. Nevertheless even this method requires the vessel segmentation to be exactly performed and it does not provide the crossing points detection. Finally the lots of filters applied for different rotations

suggest a high computational load.

The second category of methods, considering the vessel structures, includes just a few works. Al Diri et al. [53] distinguish the vessel segment ends in three groups: the "bridge" links an end to another end to form a continuous vessel (a crossings is determined when 2 bridges cross), the "junction" links an end to other two ends (and a bifurcation is detected), the "leaf" when an end is not connected to anything else. These segment ends are divided in subsets of "joinable segments ends", determined on the basis of their position and angle. Each set is solved independently, considering all the possible configurations of connection between vessel ends. The most plausible configuration is determined by means of neural cost functions. They are learned by self-organizing feature map neural networks based on a training set of junctions and approximately model the probability distribution of junction configurations. This method does not assume the vessels tracking has been performed perfectly, indeed the connectivity problem considers some tracking errors could be present, as false vessels or close vessels overlapping. They provided results on the public dataset DRIVE where the vessel segmentation has been obtained via the ESP tracking algorithm. Since they made the ESP segmentation results publicly available, the method here proposed has been tested also on these data.

In our work we adopted the same philosophy: since each vessel tracking sometimes fails, the algorithm for the bifurcations and crossing detection should account for them. We used the same method proposed by Grisan et al. based on the linking of close vessels ends on the basis of compatible features as described in [22]. In the next paragraph we start explaining this method for the bifurcations and crossings automatic detection and how it has been improved considering not just local features (depending on tracking errors) but also global information.

3.6.2 Methods

The typical vessel network as provided by the tracking procedure is composed by vessel segments disconnected at crossings and bifurcations and by other isolated segments where the tracking failed to continue (Fig. 3.18). The au-

tomatic connection of these segments is often not a trivial task. An example of complicated case is illustrated in Fig. 3.18b (this is the cropped image of Fig.3.18a at the "1st rectangle"). At this junction both a crossing and a bifurcation are present: the tracking provided lots of short vessel segments of similar caliber, very close and arranged in a a complicated way. Another difficult situation is presented in 3.19a, where the vessel under analysis is plotted with a continue yellow line. At both the ends this segment is close to other 2 vessel segments and, if just the local approach adopted for example by Martinez-Perez et al. was applied, two bifurcations would be detected, instead of just the correct one on the right. An other complicated case in presented in Fig. 3.18c, which is a particular of Fig. 3.18a at the "2nd rectangle". The tracking algorithm in this case provided an uncomplete detection of the vessels crossings (the lower left segment has not been tracked near the crossing point). Therefore most of the aforesaid methods would have failed because a bifurcation would be detected.

Our algorithm has been conceived in order to solve these critical situations. The rationale of our method is that global information can provide a necessary help for the local analysis about vessels connection. Indeed if we look just at the cropped images, it is difficult to understand how vessels are arranged, on the contrary looking in a larger area the human eye understands from which vessels they derive in their path from the OD to the fovea (or to the retina periphery). This information has been accounted in our algorithm considering the arrangement of the vessel in respect to the OD, the fovea and the parabola as defined in the vessels model presented in section 3.4.2. In particular we want to understand which is the "versus" of the vessel segment: the positive "versus" is defined from the end "closer" to the OD to the one more "distance" (no the Euclidean distance is considered but the distance along the vessels path from the OD to the periphery). The procedure to identify the versus, for example at the vessel barycenter, is explained in Fig. 3.19. We defined three "reference" directions for the vessel: the first one is that of the line connecting the vessel barycenter to the OD, the second one of the line connecting the vessel barycenter to the fovea, the third one of the line passing trough the barycenter and perpendicular to the parabola 3.19b. For each vessel the most informative "reference" direction is chosen: it is deter-

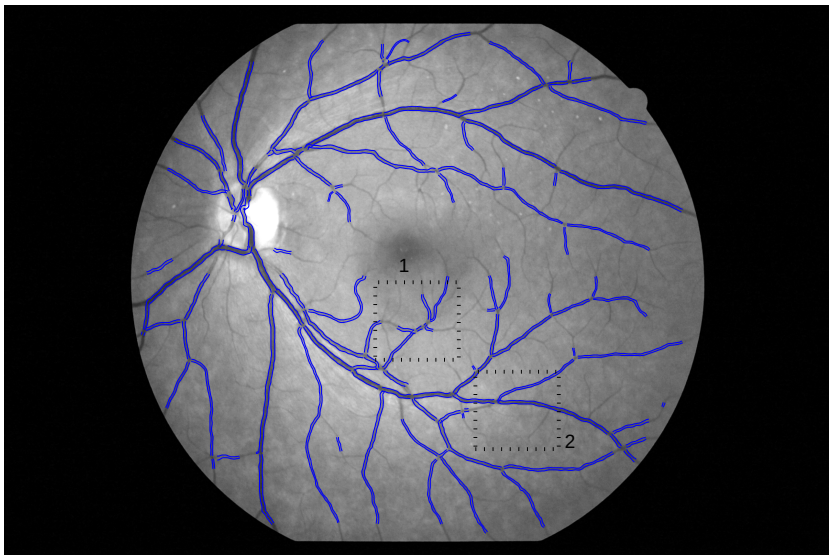

(a)

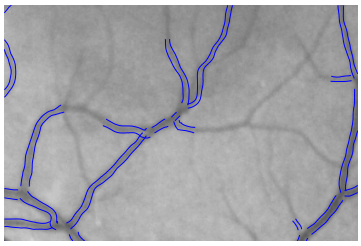

(b)

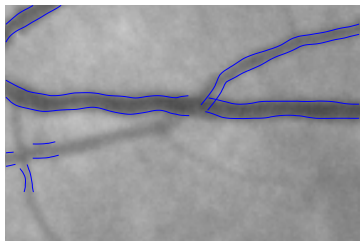

(c)

Figure (3.18). *An example of the vessel network provided by the tracking algorithm. Vessels appear disconnected and in some cases the automatic connection procedure is an hard task. In b) lots of short isolated vessels are close and arranged in a unusual way. In c) the tracking failed to detect part of a vessel at a crossing*

mined as the one with the smaller direction difference in respect to the line tangent to the vessel at its barycenter. In the example the smaller angle is α, hence the "reference" direction is given by the fovea position and the positive versus is defined according to the line connecting the barycenter to the fovea (Fig. 3.19b). Therefore in this case just the correct bifurcation plotted in red has been detected and the other candidate bifurcation on the left has been rightly discarded.

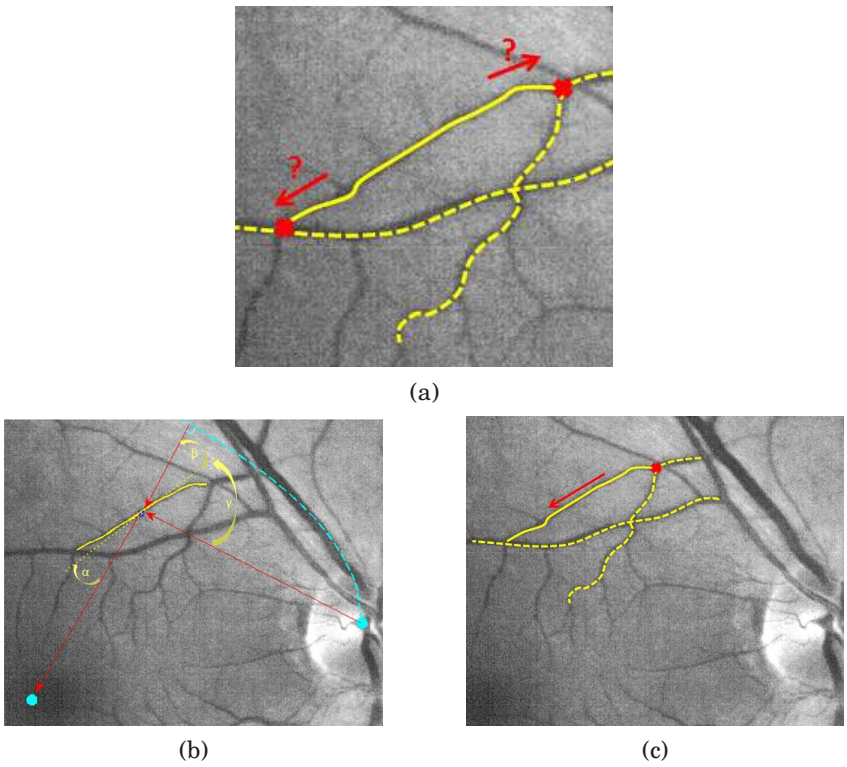

Figure (3.19). *The estimation of the vessel "versus". It is to difficult to infer the "versus" just considering a local window: two bifurcations would be detected (a). If a larger window is considered the information about the OD, fovea and vessels parabola is considered. In this case the fovea is chosen to provide the most informative "reference" direction (b). The vessel is oriented towards the fovea and only the correct bifurcation on the right is finally detected (c).*

Actually the vessels versus is not estimated just at its barycenter, but in each sample point of the centerline. Therefore for each vessel we obtain a

probability for the vessel versus. Vessels are classified as "sure" vessels if the versus probability is larger of a threshold empirically set at $th_{versus} = 0.9$, as "unsure" otherwise. A connection between vessel ends is possible if the vessels have a "sure" versus and the "first" end of a vessel and the "second" end of the other one are considered.

The linking procedure

We implemented the linking procedure presented by our research group in [22].

The segments belonging to the same vessel are likely to have end-points which face each other and that are likely to be similar with respect to direction (modulus π), caliber and intensity. In order to identify those extrema candidates to be connected, we have devised a greedy algorithm that exploits four features: distance between two end-points, their respective caliber, their direction and the difference in their mean greylevel values, evaluated in a 5x5 neighborhood. Since the meaning of these features is very different, and it is difficult to robustly normalize and combine them, four score functions have been defined between every pair of end-points p_i and p_j in the vessel structure. Being $\delta_{i,j} = \sqrt{(x_i - x_j)^2 + (y_i - y_j)^2)}$ the Euclidean distance between the two points, and denoting with $\bar{g}_i$ the mean grey-level value in a 5x5 neighborhood around p_i, and being σ_δ, σ_θ, σ_d scaling constants, the scores are:

$$\Delta_{i,j} = \exp^{-\frac{\delta_{i,j}}{\sigma_\delta}} \tag{3.18}$$

$$\Theta_{i,j} = \exp^{-\frac{\theta_{i,j}}{\sigma_\theta}} \tag{3.19}$$

$$D_{i,j} = \exp^{-\frac{d_{i,j}}{\sigma_d}} \tag{3.20}$$

$$G_{i,j} = \exp^{-\|\bar{g}_i - \bar{g}_j\|} \tag{3.21}$$

Pairs of end-points having all four scores above minimum thresholds are considered for connection. The algorithm searches hierarchically for pairs with the greater Δ, and among them those with the greater Θ. The resulting pairs are connected, yielding to a unique vessel, then the matrices Δ,Θ, D are updated by removing the linked pairs. The procedure continues until there are no more end-point pairs having scores in 3.21 above the thresholds.

The algorithm by Grisan et al. has been improved taking into account also the number of connections: at each iteration when the pair with the highest score is chosen, a subsets of pairs in its neighborhood is considered. Different connection configurations are compared and the one with the maximum global score is chosen (given by the sum of the single pair scores). This improvement allowed to mange complex situations where a lot of vessels are involved, as in Fig. 3.21.

The crossings and bifurcations detection

Once the linking procedure has been performed, a crossing point is identified where two vessels crossing and a bifurcation where the prolongation of a "sure" vessel at the "first" end crosses another vessel (the length of he prolongation segment has been defined empirically). Moreover the "versus" information has been exploited to detect crossing points even if the tracking has not been properly performed or the vessels are at the periphery of the retina (arrows with a continuous line show these situations in Fig. 3.20). In these cases a crossing point is detected if the prolongation of a "sure" vessel at the "second" end, crosses another vessel.

3.6.3 Results

We compared the performance of our algorithm with the best results provided in literature [22] [53] [52]. In tables 3.9 and 3.10 the comparison is provided.

In the first table results are presented as sensitivity and true predictive value according to how they are provided by the compared methods. The first index evaluates how many correct bifurcations (crossings) are found among the all real true bifurcations (crossings), the second one among those automatically detected. Our method behaves significantly better than the one by Grisan et al., indeed it has been conceived in order to improve this method previously developed by our group. The results have been obtained on the same dataset used by Grisan (DB60), composed of 60 images with 50^0 FoV, focused centrally between the temporal margin of the optic disc and the macula. They were slides then digitized with 24-bit color depth and 1300 dpi, yielding an approximate size of 1400x1200. The method by Azzopardi et al. provided

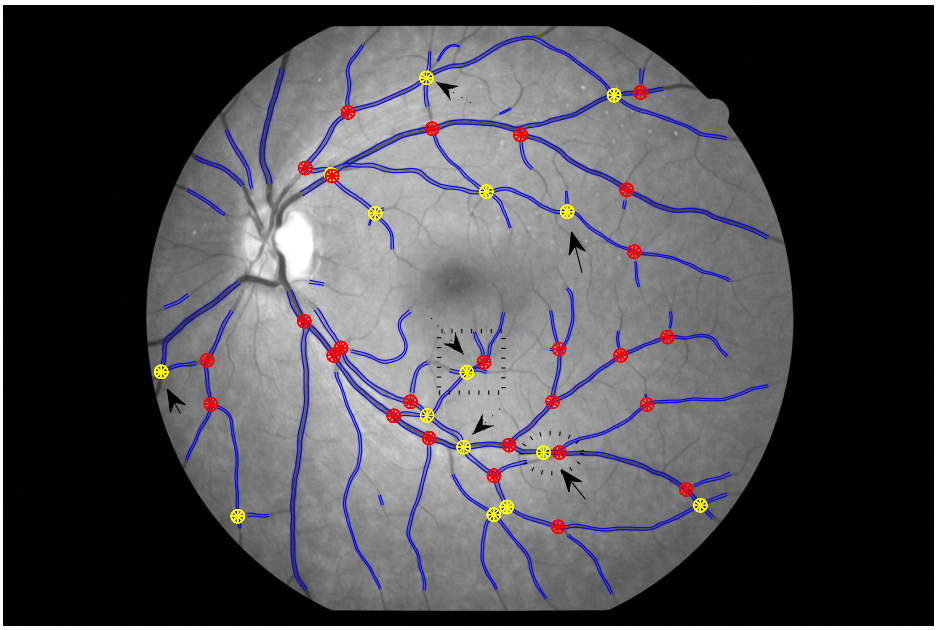

Figure (3.20). *The automatically detected bifurcations are highlighted in red and crossings in yellow. Arrows indicate difficult situations. In particular arrows with continuous lines show crossing points detected thanks to the "versus" information even if the tracking has not been properly performed. The rectangle indicates a complicate situation zoomed in Fig. 3.21. The circle shows a situation where the crossing point has been correctly detected thanks to the "versus" information. However in this case also a wrong bifurcation is found because one of the two vessels crossing is split in two segments (the linking procedure failed because the two segments ends are too distant)*

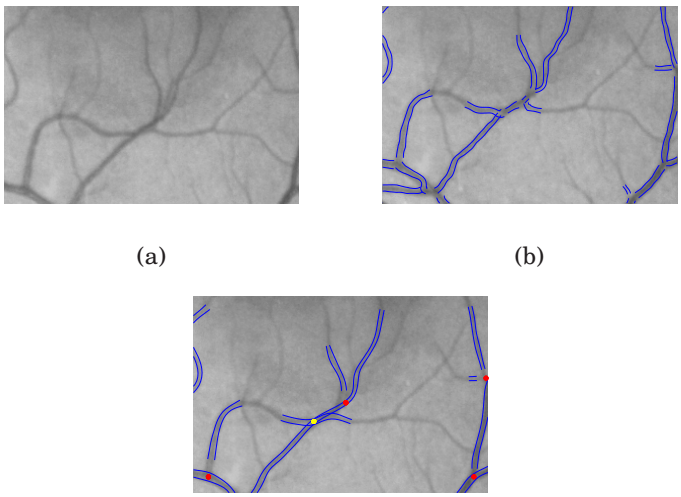

(a) (b)

(c)

Figure (3.21). *These image are cropped from from 3.18a (1st rectangle) and 3.20 (rectangular area). This is a critical situation for the linking and bifurcations/crossings detection procedures, because of the large number of vessel involved and their unusual arrangement. The "versus" information and the linking procedure encouraging configurations with lots of connections, allow to solve this critical situation. a) the image, b) the result of the tracking procedure, c) the tracking after the linking procedure. A correct bifurcation (in red) and a correct crossing (in yellow) are finally detected.*

better results than ours. Nevertheless it does not allow the detection of crossing points and it reports results just on a perfect vessel segmentation (the one provided for the DRIVE dataset). Since this method does not consider tracking errors and it does not manage these critical situations, it is probable that in situations where the tracking is performed automatically, the discrepancy of results is not so high.

In table 3.10 results are provided using not only the same dataset as Al-Diri, but also their automatic tracking segmentation via the ESP algorithm (results on the DRIVE dataset are available on the REVIEW site). Therefore this is the comparison most reliable. Here the indexes evaluated regard the fraction of vessel segment ends that are correctly identified as belonging to bifurcations, crossings or as simply leaves. Our algorithm provides very interesting results with true predictive values (for each class the fraction of vessel ends really belonging to that class) of about 0.9 for all the three classes.

Dataset	Method	Tracking method	Sens. Bif.	TPV Bif.	Sens. Cross.	TPV Cross.
DB60	Grisan et al. [22]	their autom. track. method	0.76	0.87	0.62	0.74
	our method	our autom. track. method	0.83	0.87	0.62	0.74
DRIVE	Azzopardi et al. [52]	DRIVE manual segmentation	0.98	0.95	-	-
	our method	DRIVE manual segmentation	0.80	0.92	0.93	0.71

Table (3.9). *Comparison of our results with those provided by other methods. The same datasets have been considered.*

Dataset	Method	Tracking method	TPV Bif.	TPV Bridges	TPV Leaves
DRIVE	Al-Diri et al. [53]	their autom. track. method (ESP)	0.71	0.76	0.59
	our method	their autom. track. method (ESP)	0.94	0.91	0.87

Table (3.10). *Comparison of our results with those provided by the Al-Diri's method. The percentages of vessel ends rightly classified as bifurcations, bridges or leaves, are reported.*

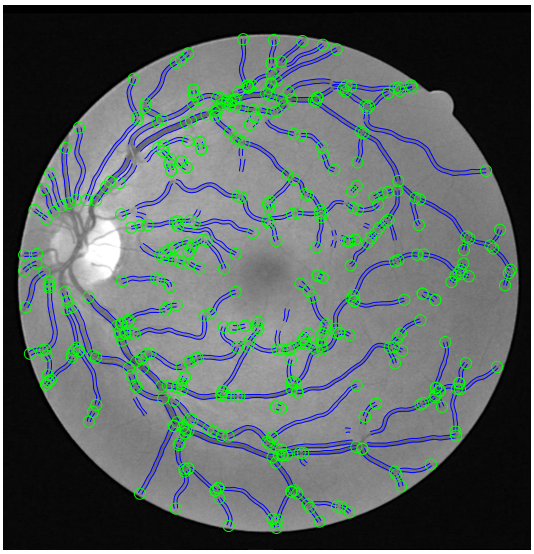

(a)

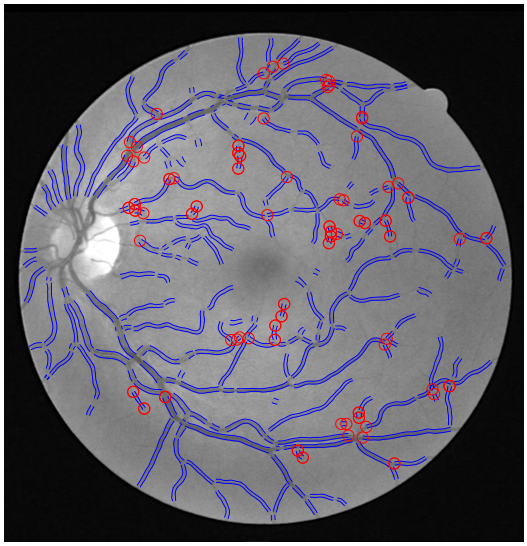

(b)

Figure (3.22). *Results on a image belonging to the DRIVE dataset, where the tracking has been performed by the ESP algorithm [53]. The vessel ends correctly classified are marked in green (a), those wrongly classified in red (b)*

Chapter 4

The automatic vessels classification in arteries and veins

If several algorithms have been developed to segment the vessels network, very few works have been reported in the literature about the automatic vessels classification as arteries or veins, despite the useful application this could have in the early diagnosis of retinopathies. In this chapter an algorithm for the artery/vein classification is presented. It starts considering local features regarding color of the vessel centerlines and the intensity profile of transversal vessel sections. An initial probability to be vein is assigned to each vessel. Secondly it takes into account morphological constraints deriving from the vascular tree considered as a graph: at bifurcations and crossing points the vessels have a defined AV pattern, since branches belong to the same class as the trunk and two vessels crossing are surely of different type. The algorithm can be customized for a particular important application: the AVR parameter estimation, which is performed just in a circular ROI centered at the OD.

The algorithm is planned to be run after a vessels segmentation and, as usual, we assume the detected vascular tree is represented by the set of triplets (x_i, y_i, c_i), whose elements represent respectively the coordinates of vessel center-point (x_i, y_i) and the vessel caliber c_i.

4.1 Introduction

In the early stage of several retinal diseases vascular changes do appear but they often affect differently each type of vessels. For example, vessel tortuosity in diabetic retinopathy affects arteries and veins in a different way; focal arteriolar narrowing, venous beading and generalized arteriolar narrowing are all important vascular signs affecting both hypertensive and diabetic retinopathy.

Arteries usually appear brighter than veins and sometimes with a central reflex due to the increased reflectivity of the arteriolar walls because of the oxygen content (see e.g. in Fig. 4.1a). Nevertheless these differences are visible only in the main vessels and are usually dependent on patients and locations on the retina, making the AV classification a hard task (as in Fig. 4.1b).

Two different approaches have been adopted so far in literature: the first one takes into account the entire vessel network and it requires an initial step of manual labeling of some vessels as arteries or veins, whereas the second one considers the color features of single vessels and is completely automatic.

The first method has been implemented by Rothaus et al. ([54]) and previously by Akita and Kuga ([55]): they considered the vessel network as a connected graph, where the classification information propagates from the first manually labeled vessels to the connected vessels. In these two papers the information has been dealt with in a deterministic and probabilistic context respectively. Both the approaches have the limit to be very dependent on a correct vessels tracking, because the initial manual labeling of some vessels is then propagated exploiting the connectivity and if it fails the error is propagated trough the vascular network. Rothaus et al. concluded their paper suggesting the need to integrate the structure-graph approach they used with local features regarding shape and color vessels. For the AV classification they reported just qualitative results plotted in images, thus the comparison with this method can not be performed.
The second approach has been adopted by Grisan et al. ([56]), who used an unsupervised fuzzy classification applied on each different quadrant (“divide

(a)

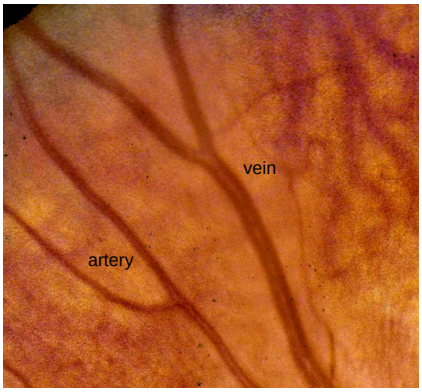

(b)

Figure (4.1). *Sometimes veins and arteries appear very different (a), but they are often hardly distinguishable (b)*

et impera strategy"). This method had shown very good results (about 93 % of correct classification in large vessels), but its results have been provided just for a single dataset and its application on our datasets did not yeld the same performance (see the "Results" section). Also Niemejer et al. ([57]) developed a vessel classification algorithm for the AVR computation based on the second approach. They used a supervised approach based on the k-NN classification but also this method has been applied on images from a single dataset: the public dataset DRIVE. In the last step of the classification algorithm they used the prior knowledge that arteries and veins usually come in pairs. Results are provided just for large vessels where the manual AV classification has been performed by an expert only on the basis of the local color features and not on connectivity. Kondermann et al. ([58]) introduced the use of metaknowledge information: they took into account the anatomical information that vessels cross each other only if they belong to different classes. They used a supervised classification method based on PCA and neural networks applied only in the circular ROI for the AVR computation: results on 4 images of high quality have been reported. Li et al. ([20]) used a piecewise double gaussian model to fit the vessel profile and to classify it as artery or vein on the basis of features given by the model parameters. They tested the algorithm in 237 segments, achieving an accuracy of 82% for arteries and of 89% for veins, but they do not specify the kind of images, wheather all the vessels have been considered or large ones and/or vessel in the AVR ROI. Finally Muramatsu ([59]) developed a method to classify vessels with the purpose to calculate the AVR using a non standard procedure that considers just the largest vessels on a ROI wider than the usual one, with images centered on the macula. Also in this case a supervised approach has been applied.

An unsupervised multiclassification approach is proposed here in order to analyse different features in a specific way, i.e. in the most adequate and controlled way for each feature. In particular the two classifiers are presented respectively in the next and in the following paragraph, later their integration and the inclusion of metaknowledge information from the "graph vascular tree" are performed. The whole algorithm works in a probabilistic context: each classifier assigns to each vessel a probability to be vein P_v.

The algorithm is not applied on the whole vessels, but on their sections

belonging to different concentric circular regions centered at OD and with width the OD radius. This procedure allows to exploit information deriving from the radial symmetry with respect to the OD, for example regarding the similar number of arteries and veins and the usual alternation of the two types of vessel. The P_v of each vessel sections are then combined together by considering their average, weighted or not for the caliber and/or the length of the correspondent vessel section. The algorithms are applied separately on the single circular ROIs, as shown in Fig. 4.2.

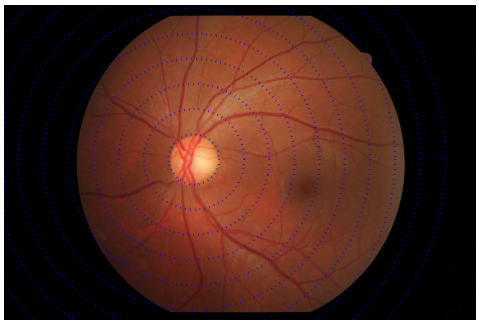

Figure (4.2). *The circular regions where the AV classification algorithm is applied*

4.2 The single pixel color classification

The first step in AV classification is to consider color features, since for example arteries appear usually brighter than veins. We analyzed the discriminating power of a series of color features derived from the RGB and HSL color spaces using the mean or variance or correlation (for example between the red value and the green value) of pixels belonging to a circular neighborhood of vessel centerline pixels. Results from different neighborhood radius lengths were compared and the best performance was achieved with a radius equal to 0.3 times the estimated caliber of vessel in that point of the centerline. Other features, referring not to axis pixels but to transversal profiles, were also evaluated: signals obtained from RGB and HSL intensity values along sections transversal to vessel axis were analyzed by computing the energy of

their first and second derivatives (supposed to be higher in arteries) and the height of the central peak (grater in arteries as central reflex is more evident than in veins), expressed by the “color contrast" parameter described in the next section. A summary of these features is reported in table 4.1.

Nr.	Features
1-3	Mean of red, green and blue
4-6	Mean of hue, saturation, luminosity
7-8	Variance of red and green
9	Correlation between red and green
10	Correlation between red and blue
11	Correlation between green and blue
12	Correlation between red and hue
13	Correlation between red and saturation
14	Correlation between hue and luminosity
15	Correlation between green and saturation
16-18	Energy of 1^{st} derivative of red, green and blue trasversal signals
19-21	Energy of 2^{st} derivative of red, green and blue trasversal signals
22-24	Heigth of central red, green and blue peaks

Table (4.1). *The complete set of features analyzed*

Combinations of one, two or three features constituted the features vector input for a Fuzzy-C-means classifier, chosen for its greatest robustness to outliers than the K-means one. We applied the unsupervised clustering because of the presence of a large intra- and inter-image contrast and luminance variations, which may be cause problems in a supervised classification approach. Because of these great differences in color between different image regions, I adopted here the same strategy previously developed by our group [56], who proposed to divide the image into four quadrants and to apply the classification algorithm separately in each single region. In that study the most discriminating features were the variance of red and the mean of hue. In the study by Niemeijer et al. [60] the feature selection phase elected a group of 12 features as the most useful for classification, corresponding approximately to features number 1,4-5,19-21 here. Our results on the first dataset of 10

images showed good performances using pairs of features and in particular the mean of red and variance of red (1,7) and about the same results were obtained with the mean of red and mean of hue couple (1,4).

One limit of the “divide et impera" strategy is the image partition into four quadrants by the x and y axis centered on the optic disk and parallel to the image borders. This division should follow the natural structure of the vessels net as two opposite parabolas centered at the OD and with horizontal axis. However the true axas parabolas are not usually parallel to the image sides and the separation between vessels pairs is not always so clear: sometimes they follow a radial distribution or a part of a vessel axis could belong to different quadrants because of their natural course or because the optic disk center identification has not been very accurate. As a consequence, it could happen that in a quadrant there is only one great or medium caliber vessel or a strong predominance of pixels of the same type (artery or vein), therefore the fuzzy clustering of pixels into two groups is often not consistent. This limit has been overcome by using ten quadrants axis rotations (rotation angle: 9^o): the FCM classification is applied in each quadrant for each rotation and assigns to each vessel the probability to be vein as the fraction of vein pixels over the total number of vessel pixels. The vessel final probability is then computed as the average between the ten rotation probability values (Fig. 4.3).

A useful a priori information is given by the similar number of vessels classified as arteries and as veins and the anatomical information that in each circular region there are at least six arteries and six veins (indeed the AVR parameter is calculated in a smallest circular region, with at least the same number of vessels than in the other regions, considering the six largest arteries and the six largest veins). This is a prior very strong, therefore in each rotation it contributes for the vessel probability estimation: e.g. if the total number of veins is less than six, the artery with the vein probability closest to 0.5 become a vein and this procedure is repeated until the number of veins is at least six.

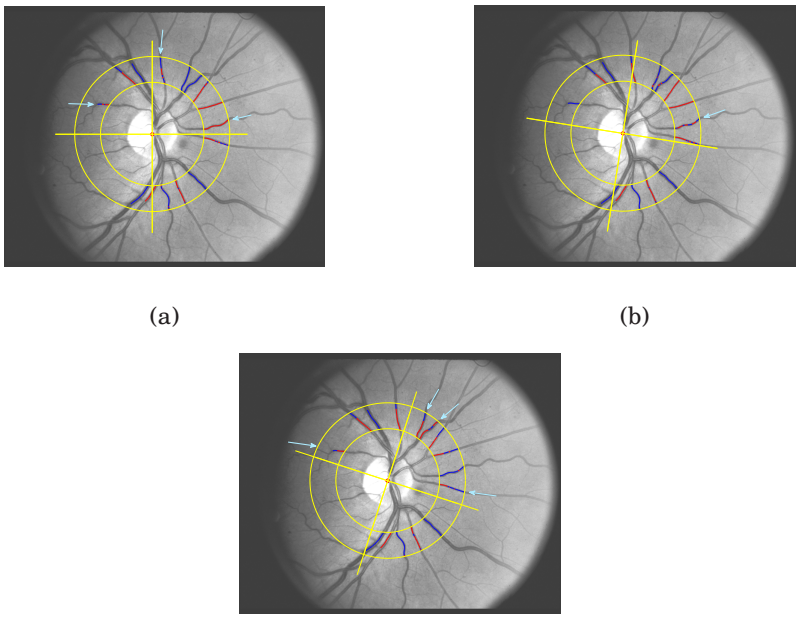

(a) (b)

(c)

Figure (4.3). *A/V discrimination results given by the FCM classifier applied for different axis rotation: no rotation (a),* 18^o *(b) and* 36^o *angle rotations. If the number of vein pixels (blue) is greater than the number of artery pixels (red), the vessel is identified as a vein (or viceversa as an artery) with a probability equal to the percentage of vein pixels (or viceversa equal to the percentage of artery pixels). Arrows indicate vessels wrongly classified: some misclassification errors are present only in corrispondence to a certain number of rotations. It shows the importance of mediating between different rotation results.*

4.3 The single vessel classification based on central reflex

One of the most discriminating features that clearly appears by visual inspection is the central reflex, which is more usual and evident in arteries than in veins, in particular because of the oxygenate blood that increases the vessel reflectivity. Other less usual conditions may contribute: e.g. the light reflex is more common in younger retinas due to their increased reflective surfaces or in patients with a pathological state, as in diabetic subjects.

We decided to exploit this different behavior between arteries and veins as the discriminating feature for this second classification approach, as described in our work [61]. In Fig. 4.4 we can notice the typical red intensity signals of an artery (Fig.4.4a) and of a vein (Fig.4.4b) measured on a section transversal to their axis with width 1.2 times the vessel caliber. The signal tails refer to the background pixels, which show greater red values than the pixels inside the profile concerning the vessel; the central pixels intensity values increase because of the central reflex, which appears higher in the artery than in the vein (sometimes in veins the reflex does not exist at all).

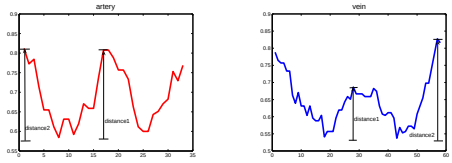

(a) (b)

Figure (4.4). *A typical artery transversal profile (a) and a typical vein transversal profile (b). The "red contrast" parameter is given by the ratio between distance1 and distance2.*

From the vessel transversal profile we derived a parameter, called the "red contrast", which measures the relevance of the central reflex: it is defined as the ratio between the peak of intensity in the central part of the vessel red profile and the largest of the intensities at two end-points of the profile:

$$RedContrast = \frac{maxR_{l,2l} - minR}{maxR_{extr} - minR} \tag{4.1}$$

where $maxR_{l,2l}$ is the peak of intensity in the central part of the vessel profile, that is between 1/3 and 2/3 of the transversal profile width (equal to 1.2 the vessel caliber, $l = 1/3$ of the profile width), $maxR_{extr}$ is the max value at the end-points and $minR$ is the minimum value along the profile.

For this feature we adopted a classification approach applied to the entire circular ROI and not to single quadrants. This is justified by the fact the "red contrast" parameter is calculated as a ratio of local image features, therefore it is a "normalized" parameter that is not dependent on luminosity and contrast intra-image differences. A supervised classification did not allow better

results because of the great inter-image variability on the vessel central reflex magnitude: a vein in a image can show the same features of an artery in a different image or viceversa.

The classifier receives as input the average value of “red contrast" among the total transversal sections of each vessel (also median, minimum and maximum values for each vessel have been considered as discriminating parameters, but they showed inferior performances). The “red contrast" values of all the vessels are then incrementally ordered in a crescent way and a probability function is created. It assigns a vein probability of one to the vessel with the minor value and a vein probability of zero (i.e. artery probability close to one) to the vessel with the largest value. The relation between “red contrast" values and the probability P_v was designed as sigmoidal, because usually there is a small range of central reflex magnitudes with middle values that is usually relative to small vessels (the central uncertainty range) and then vessels with large values (arteries) and vessels with small values (veins), but with “red contrast" values in a large range. These considerations lead us to conceive a probability function that increases the small differences in the central uncertainty range and that reduces the extreme ranges: the sigmoidal function appeared the most suitable choice (Fig.4.5).

The classifier adapts its parameters to any specific image on the basis of some a priori information: we assume that in the ROI the number of veins is very close to the number of arteries and that this number is at least six. We exploited this information by initially assigning $P_v = 0.5$ to the median “red contrast" value; however this assumption turned out to be too strict. We assigned $\mathrm{P}_v = 0.5$ to another “red contrast" value if it follows a greater separability between the probability values of vessels that would be classified as veins and those classified as arteries and, at the same time, the condition of at least six veins and six arteries is still verified. The separability is estimated through the Fisher separability index.

The resulting classification probability $P_{v_{RC}}$ follows the Hill trend:

$$P_{v_{RC}} = 1 - \frac{CtR^h}{md^h + CtR^h} \tag{4.2}$$

where CtR is the vessel “red contrast" value, h and md are two parameters:

the first one indicates the curve slope, the second one the value where the probability is 0.5.

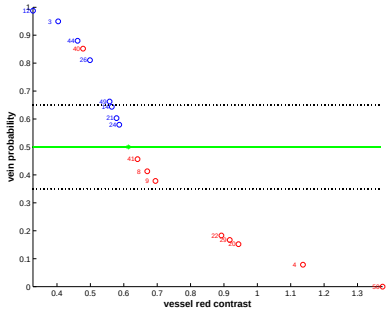

Figure (4.5). *An example of the sigmoidal vein probability function for an image belonging to the DCCT dataset. The median "red contrast" value for this image has been calculated to be about 0.6. Vessels belonging to the vein class have been highlighted in blue and arterial vessels in red. Only one misclassification error is present for this image: a small artery has been classified as a vein.*

4.4 The multiclassifier integration

For each vessel, two vein probabilities have been evaluated: the Color Probability ($P_{v_{col}}$) and the Red Contrast Probability ($P_{v_{CR}}$). Their information now needs to be integrated: since there are great interimage and intraimage variabilities and it is not possible to establish a priori which classification method is more suitable for the image under analysis, I decided to calculate P_v as the average value:

$$P_v = \frac{P_{v_{col}} + P_{v_{RC}}}{2} \tag{4.3}$$

4.5 Global information conditioning the final classification probability

Until now the classification procedure has taken into account only information regarding the single vessel appearance (except the expected number of veins and arteries), but more information can be provided looking at the entire ROI. In the next paragraphs it will be explained how metaknowledge information regarding the layout of vessels and their connections have been implemented and exploited to improve the final classification.

4.5.1 The AV alternation

In the inner circular regions the vessels are arranged in a radial way and usually an artery comes in pair with a very close vein, mainly if just the vessels trunks are considered, as in the AVR estimation. However this hypothesis is not verified at a bifurcation, where the branches belong to the same class. Anyway, if the fact that two consecutive vessels belong to different classes is likely, it is certain (if the vessel segmentation is correct) that three or more consecutive vessels can not be classified in the same way.

These considerations are summarized as follows:

- an artery comes usually after a vein and viceversa and the alternation hypothesis is more reliable the closer are the vessels: a decreasing exponential dependence links distance to alternation frequency (see below)

- no more than 2 consecutive vessels may belong to the same class

The decreasing exponential relationship linking the AV alternation probability to the vessels distance, has been conceived from empirical examination of the vessel behavior in images belonging to the training data set. The parameter setting has been provided on empirical considerations as well. The decay time parameter τ_{alt} has been set to $\pi/6$, meaning that if two vessels are 30^o apart, the alternation hypothesis is true with a probability half than if the two vessels were immediately adjacent. For angular distances larger than 30^o the alternate hypothesis is no more reliable. The angular distance

is calculated as the amplitude of the circle sector comprised between vessel i and vessel j end points on the inner circle of the ROI.

The mathematical expressions that describes this relationship is:

$$w_{i,j} = exp(-\frac{dist_{i,j}}{\tau_{alt}}) \tag{4.4}$$

The previous assumptions imply that for a vessel i, its P_{f,v_i} (its final probability to be vein) depends on its P_{v_i} (previously calculated) and on adjacent vessels' type, in particular on S_{v_j}, where S stands for the state of the jth vessel (Artery or Vein) and $j = i \pm 1, \pm 2$ (vessels are counted in a default direction, for example clockwise). This dependence has been implemented in a easier way: vessels are read clockwise, starting from a random vessel, and ending at the same vessel, therefore the first vessel is also the last one and, although for each vessel i its P_{f,v_i} can be implemented with a one-step dependence, it actually depends not just on the previous one's state, but in general on all the other vessels' state (also on the following vessels), because the "circle is closed".

The Markov chain seems to be the most suitable implementation, indeed for each step (i.e. for each vessel) of the discrete-time random process (the vessels' spatial map) two states are considered (Artery and Vein) and the conditional probability distribution P_{f,v_i} at the current step depends only on the state of the previous step $S_{v_{i-1}}$. In particular, this model can be described as a Hidden Markov Model because during the i_{th} step's analysis the states of the previous steps are not known, but only their output, that is their P_{v_j}, with $j < i$. This classical Hidden Markov Chain does not show all the properties our system has been supposed to have, i.e. the cyclicity property (the first step depends on the last one) and the dependence on the two previous steps, not just on the previous one (if two steps are of the same state, the next step has to be different). The second property could be added with a second order Markov chain, however we preferred to develop a new flexible and easy implementation tool for a Markov chain with the required properties: our Markov chain system has been studied with a binary tree, where each level corresponds to a particular vessel and a node can have two children: the "Artery" child and the "Vein" child. Fig.4.6 represents the tree structure in the case of seven vessels in a ROI (in red the "Artery" child and in blue the "Vein" child). Each path

connecting the first level nodes to a leaf represents a particular sequence of possible states for the correspondent vessels. It is possible to see that the levels' number is equal to the vessels' number plus one and if a path starts with an Artery at level 1 it will end with an Artery at level 8 (the same for the Vein). The reason is that the first and the last node represent the same vessel in order to satisfy the cyclicity property. Another important feature of this tree is that it is incomplete: if a node is an Artery and its parent is an Artery as well, the child has to be a Vein (and viceversa): this allows to implement the assumption about two maximum consecutive vessels of the same type.
This binary tree can also be seen as an acyclic graph starting from the root, where each node belonging to the same level i has a value equal to P_{v_i} if it is a Vein node and equal to $P_{a_i} = 1 - P_{v_i}$ in case of an Artery. Each arc has a weight equal to the transition probability $P_{t_{i-1,i}}$ from the parent's state at the (i-1)th level to the child'state at the i_{th} level. The transition probability $P_{t_{i-1,i}}$ is a function of the $w_{i-1,i}$ (previously defined in eq.4.4) which is multiplied by a scaling factor, equal to 0.8 if the alternation hypothesis is verified or equal to 0.2 if the parent is of the same kind of the child. The two values of the scaling factor have been assessed on the basis of empirical considerations. The value of the nodes and the cost of the arcs define the cost of the global paths starting from the first level and ending at the leaves. The probability of a particular sequence of states given the P_{v_i} observed for each vessel can be calculated as the global cost of the correspondent path. It has been evaluated on the training set in two different ways, yelding very similar results (a slight better performance has been achieved with the "Sum method" in eq.4.5):

$$w_s(s_1, .., s_n) = \sum_{i \in V}(P_{v_i} + P_{t_{i-1,i}}) + \sum_{i \in A}(P_{a_i} + P_{t_{i-1,i}}) \tag{4.5}$$

$$w_p(s_1, .., s_n) = \prod_{i \in V}(P_{v_i} * P_{t_{i-1,i}}) * \prod_{i \in A}(P_{a_i} * P_{t_{i-1,i}}) \tag{4.6}$$

where V is the set of all the nodes representing the Vein state and A the set of all the nodes representing the Artery state. In Fig.4.6 the maximum cost path is highlighted with a thicker line, it will follow that for the situation represented by this tree, the $(s_1, s_2, .., s_7) = (A_1, V_2, A_3, V_4, V_5, ..)$.

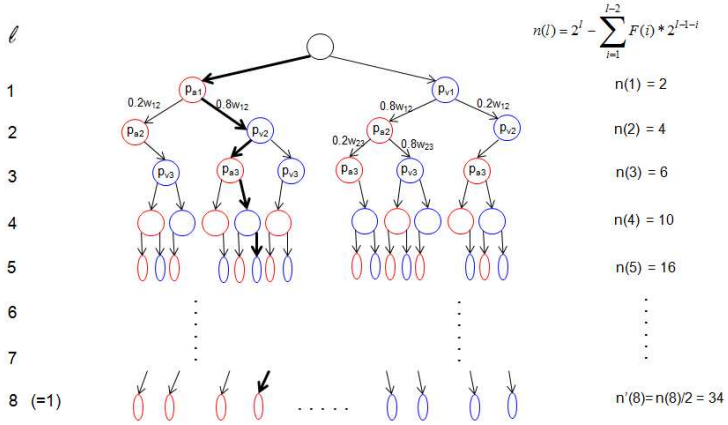

Figure (4.6). *The binary tree used to implement the final step of the classification algorithm taking into account the knowledge about the vessel network structure. Each level of the tree corresponds to a particular vessel. In this particular example only 8 vessels need to be classified. Each path from the first level to the leaf represents a possible classification of the 8 vessels. Red nodes stand for the artery class, the blue nodes for the vein one. The maximum cost sequence is highlighted with a thicker line: the correspondent vessels classification will be then applied on the vessels set analyzed. n(l) measures the number of nodes for each level l (the F function stands for the Fibonacci number).*

4.5.2 The vascular graph

In a manual examination, the examiner usually looks firstly sat major vessels in the image and labels them as arteries or veins and then classifies the smaller vessels according to the type of the major ones to which they are connected. Moreover, if two vessels cross they are assigned to different classes.

A prerequisite to the automatization of this process is that bifurcations and crossings have been correctly detected and that the linking of the various segments into a single vessel has been properly performed.

The constraints at critical points (bifurcations and crossings) is not just a local problem, because through connected vessels the information is propagated to another critical point, where other constrained are defined. In this

way the vascular network can be divided in some "clouds" of vessels linked by reciprocal constraints. Each cloud is analyzed separately as a graph with a bistable configuration. Indicating with c_i the class to which the i vessel belongs ($c_i = 1$ if it is a vein or $c_i = 0$ if an artery), if for a example a vessel a and a vessel b cross, and the vessel a is a branch of a vessel c, the cloud composed by (a, b, c) can assume the 2 configurations:

$$(c_a, c_b, c_c) = (1, 0, 1) \;\; || \;\; (c_a, c_b, c_c) = (0, 1, 0) \tag{4.7}$$

represented in Fig 4.7 by the 2 vertex points highlighted in red. The black point P in figure represents the "probability vector" associated to the the vessel triplet, i.e. $P_{a,b,c} = (P_{v_a}, P_{v_b}, P_{v_c}) = (0.8, 0.6, 0.25)$, so in this case $(c_a^{init}, c_b^{init}, c_c^{init}) = (1, 1, 0)$. The vertex point closest to the point P (in terms of Euclidean distance) is the point $(1, 0, 1)$ and it represents the most probable AV configuration. Hence, in this example the final classification becomes $(c_a, c_b, c_c) = (1, 0, 1)$, changing the classification of 2 among the 3 vessels.

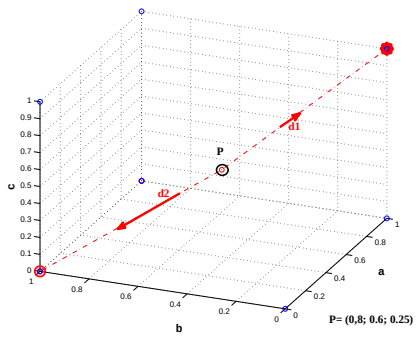

Figure (4.7). *Example explaining how the most probable vessels classification configuration is determined for a subset of 3 vessels, starting from the probabilities of the single vessels. Points at vertexes represent the possible configurations (1=Vein, 0=Artery), the coordinates of the point P the vessel probabilities. The most probable configuration is represented by the vertex closest to P.*

This method cannot be applied if errors in the tracking postprocessing algorithm determine an impossible configurations of constraints, as in the example above if the c vessel was connected to the b vessel. These cases are

simply excluded from this final step and the vessels classification relies on the probabilities estimated so far.

This final step has been intended to be applied when a reliable connection of vessel segments and a reliable bifurcations and crossing detection has been performed. In the next paragraphs we will see that in our experiments with different datasets the global information always improves the classification results, mainly if the image is poor in quality and/or resolution and the color features by themselves are not so informative for the classification.

4.6 Results

Firstly we report the results of the classification algorithm applied only to vessels considered for the AVR computation, so in the circular ROI comprised between 2 and 3 OD radius; if a vessel branches, just the trunk is analyzed. Secondly, results on entire images are presented. The first situation is more easily managed, because of the small area where just a minimal variability in color intensity may be present, compared to the whole image. Moreover, the radial distribution of vessels allows the AV alternation hypothesis to be almost verified; finally the number of arteries and veins is in this case very similar.

4.6.1 Materials

The algorithm for classification was firstly developed for its application in the AVR computation. To this purpose it has been tuned using a set of 10 images, acquired during the DCCT study [62]. The testing set was composed by 58 images, belonging to three different datasets: 10 derived again from the DCCT dataset, 18 from the ETDRS one [9] and 30 acquired by the Vision Research Unit in the Department of Twin Research and Genetic Epidemiology, King's College of London. Images extracted from DCCT and ETDRS datasets were made available by the Center of Ophthalmology and Visual Sciences, University of Wisconsin, USA; they were acquired in the analogic format with a 30^o field of view and then saved in digital format (with .tiff extension), with a resolution of 3.7 μm/pixel, resulting in 2346 x 2652 pixel images. The other

thirty images were acquired directly in digital format (with .jpg extension), their resolution was of 6.9 μm/pixel with a dimension of 1664 x 1664 pixels. For this first step the vessel segmentation has been obtained using the tracking method by Poletti et al. [15] and in case of visible errors they have been edited with a user-friendly interface that will be described in the last chapter. The "extended" version of the algorithm including all the vessels in the image did not need a further training phase. Nevertheless a lot of "versions" of the method have been analyzed: for example about the inclusion or not of crossings and bifurcations information and about how the P_v of the singular vessel segments of each circular ROI are weighted in order to define P_v of the complete vessel. These "versions" have been tested on three sets of images: a small dataset composed by 6 images from the Mongolia dataset, the first 8 images of the DRIVE training set, 28 images resulting from the registration (obtained with a software used by the Reading Center at the Moorfields Eye Hospital) of couples of images (from the Mongolia dataset) relative to the same eye and taken with 2 different FoVs. The registered images are very suitable for evaluating the performance of the graph-approach AV classification because of the large number of connected vessels forming the complete vascular tree. The images used for the "extended" version differ from those analyzed by the normal algorithm, because they include also images centered on the fovea which are more suitable to test the the version of the algorithm.

4.6.2 AVR ROI results

Results are presented in tab 4.2. They have been evaluated both separately on each single dataset and on the entire testing dataset. Considering a vein vessel classification as the positive outcome of a test and the artery vessel classification as the negative one, the following indexes have been evaluated: the sensitivity (V), the specificity (A), the accuracy among the six largest arteries and the six largest veins, the global accuracy among all the fifteen vessels considered per image and the computational time. Each performance index has been calculated considering each dataset as a whole (that is considering vessels from all the images together) and also taking into account the single images; mean and median value of each performance index from all

the images have been evaluated.

Dataset		Sens. (6V)	Spec. (6A)	Accur. (6V+6A)	Tot. Accur.	Time (sec.)
DCCT (TRAINING)		0.92	0.90	0.91	0.92	
	mean	0.92	0.90	0.91	0.92	10.5
	median	1	1	1	0.97	
DCCT (TESTING)		0.90	0.90	0.90	0.89	
	mean	0.90	0.90	0.90	0.89	12.16
	median	1	0.83	0.92	0.90	
ETDRS		0.94	0.91	0.93	0.89	
	mean	0.94	0.91	0.93	0.89	12.00
	median	1	1	0.96	0.90	
KING'S		0.92	0.88	0.90	0.88	
	mean	0.92	0.88	0.90	0.87	9.64
	median	1	0.92	0.92	0.90	
ALL (TESTING)		0.93	0.89	0.91	0.88	
	mean	0.93	0.89	0.91	0.88	10.81
	median	1	1	0.92	0.90	

Table (4.2). *Results.*

Some considerations emerge from the analysis of the table's results. First of all, the algorithm provided about the same results in the different testing datasets and they are not significantly different from that obtained on the training dataset. This despite a remarkable variability among the datasets for what concerns both the image features (as resolution, dimension, file format, field of view, quality) and the subject features (diabetic patients in the DCCT and ETDRS study and people from a genetic study for the King's College's dataset). Moreover, a large inter-subject variability exists (Fig. 4.8). The similarity in the results appears to be due to the multi classification approach applied and to the introduction of meta-knowledge information about the general vessel network structure, therefore independent on the particular image analyzed. Fig. 4.9 shows the rate of classification accuracy obtained for each image of the four datasets. Each panel refers to a particular dataset: the first plot represents the results achieved with the "color pixel" classification, the second one with the "red contrast" classification and the third one with their integration and the introduction of the meta-knowledge information.

A different behavior is clearly recognizable between the ETDRS (panel c)

and the King's College dataset (panel d): in the first one, the classification provided by the "color pixel" algorithm is more reliable than that provided by the "red contrast" algorithm and they add complementary information resulting in very reliable results (third row plot). On the contrary, in the King's College dataset the second method is clearly more reliable than the first one, but their integration provides very good results as well. The "portability" (the algorithm can be used without regarding the image analyzed) and the "modularity" (because of the different parallel steps) properties constitute the major advantages of this algorithm.

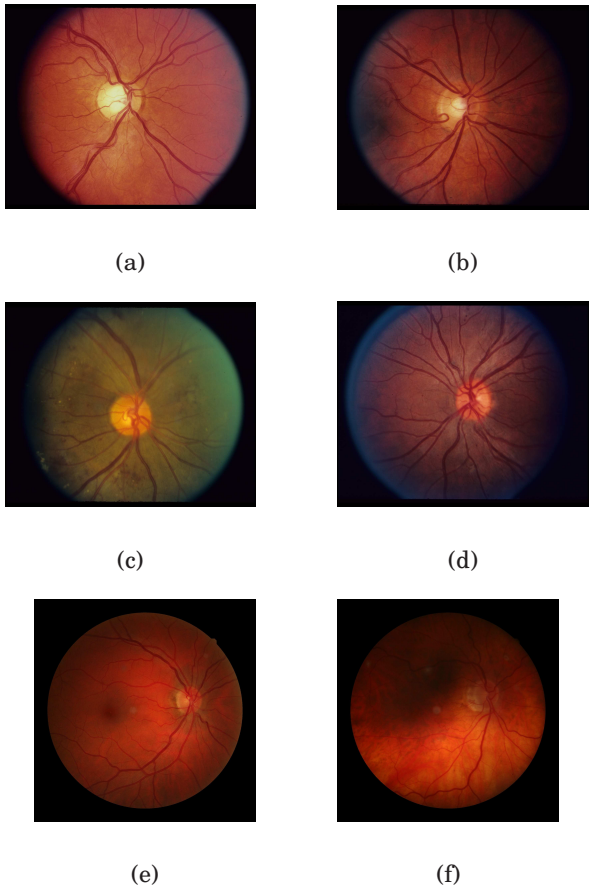

Figure (4.8). *Examples of images belonging to the DCCT dataset (a-b), to the ETDRS dataset (c-d) and to the King's College dataset (e-f).*

From table 4.2 it is possible to see that almost all the performance indexes are greater than 0.90, in particular the veins vessels have been classified

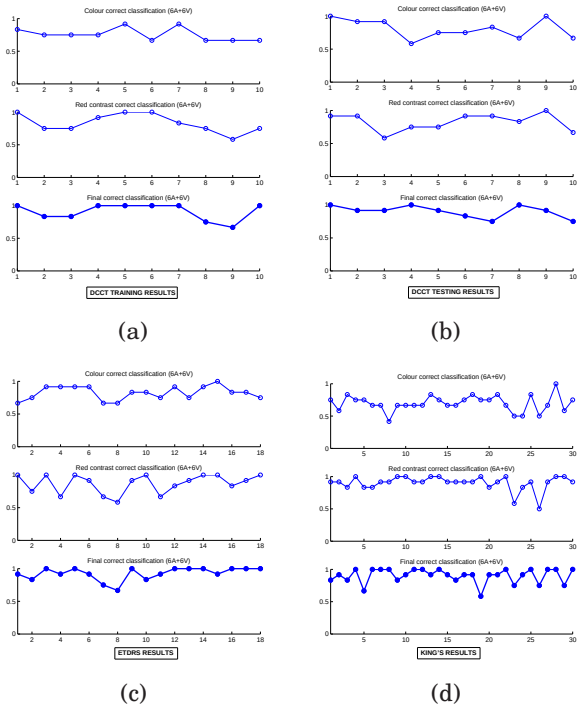

Figure (4.9). *The four panels represent for each dataset (a) DCCT training, b) DCCT testing, c) ETDRS, d) King's College) the rate of accuracy of the different steps of the classification algorithm: with the "color pixel" classification, with the "red contrast" classification and the final results (width line). The results are shown for each image as the number of the correctly classified vessels among the six largest veins and arteries.*

with a very high accuracy (here denominated as "sensitivity") equal to 0.93 (considering all the images together), whereas an accuracy of 0.89 has been obtained in the arteries' classification. The algorithm's application on the twelve vessels considered for the AVR provided an accuracy equal to 0.91, which is not significantly higher than the ability to classify fifteen vessels per image, which is equal to 0.88. It is important to highlight that among the twelve largest vessels, also medium and small caliber vessels are often considered. It means that the accuracy results have not to be intended just for the largest vessels but in general for vessels belonging to a larger caliber range. Then it is useful to observe than a 0.93 mean sensitivity in all the

images means that on average per image 5.58 out of 6 veins are correctly classified, a 0.89 mean specificity means that on average per image 5.34 out of 6 arteries are correctly classified and finally a 0.91 mean accuracy means that on average per image 10.92 out of 12 vessels are correctly classified. In other words the user has to manually correct just one vessel per image, and this is a very fast operation in our AVRnet system, described in the next chapter ([63]). Finally, the median value of each performance index is higher than the mean value and in many cases it is equal to 1, meaning the for the majority of images no user correction operation is required.

It is difficult to compare our results with those from previous papers because of the different conditions in which the classification has been applied. In Niemijer et al. [60] the classification has been performed on vessels manually segmented that have been classified by an expert just on the basis on local color information. Moreover, the method used is threshold dependent (a k-Nearest Neighbour classifier was used) and therefore the results are presented with a ROC curve, which is not applicable here because our method uses a fixed threshold of 0.5 for the P_v. Anyway, the ROC curve in [60], showed a sensitivity of 0.9 for a specificity of just 0.7 and, viceversa, a specificity of 0.9 for a sensitivity value of 0.6. The work presented by Li et al. [20] considered a group of vessels (their diameter and location are not specified) segmented in a semiautomatic way (the vessel profile is fitted with a double gaussian model): it showed a sensitivity of 0.82 and a specificity of 0.89. In our previous work ([56]), where just the “color classification" has been applied, the vessels segmentation was provided automatically and the AVR ROI has been considered like in this work. Although the results are similar to those provided here (accuracy of 0.87 on the total vessels and 0.93 on the main vessels), images from a single dataset have been analyzed. The application of the “color classification" algorithm only on the datasets considered here, has shown a very much performance and this is the reason that led us to improve our classification algorithm.

4.6.3 Whole image results

In this paragraph different implementations of the structural-graph approach and their performance are presented.

These versions differ for:

1. how the P_v of the single segments belonging to different ROIs are integrated to get the final P_v of the vessel
2. the kind of relationships among the vessels, i.e. if bifurcations and/or crossings (or neither of these) "constraint" points are considered
3. in case the "connectivity constraints" points are considered, if all vessels provide the same contribution or if their P_v are weighted for their caliber and/or length
4. if the "constrained" points have been detected automatically or manually provided by the user

For the first problem, indicating with Pv_{si} the probability to be vein of the i_{th} segment belonging to the vessel j (with $i = 1, .., n_j$ and n_j representing the number of circular ROIs the j vessel crosses), the following implementations have been considered :

$$Pv: \quad Pv_j = \sum_i Pv_{si} \tag{4.8}$$

$$Pv^{w_d}: \quad Pv_j = \sum_i w_{di} * Pv_{si} \tag{4.9}$$

$$Pv^{w_{dl}}: \quad Pv_j = \sum_i w_{di} * w_{li} * Pv_{si} \tag{4.10}$$

$$\tag{4.11}$$

where w_{di} and w_{li} are respectively the "diameter" weigh and the "length" weigh of the i_{th} segment. In table 4.3 the reliability of these three different implementations for each dataset is reported. The results have been computed considering both the "vessel" unit and the "pixel" unit: the former index just explains how well the algorithm works on vessels, the latter takes

into account also the length of the vessels because it reports how many pixels have been correctly classified.

From these first results it is possible to notice firstly that no significant difference exists among the three implementations, secondly that the algorithm works better in the Mongolia dataset (both with single and registered images) than in DRIVE. This is not unexpected, given the better quality and higher resolution of images belonging to the first dataset. Thirdly the indexes computed for the "vessel" unit are significantly lower than those obtained with the "pixel unit". The reason is twofold: the shorter vessels usually are also thinner and they are much more difficult to classify (in this case just the connectivity information is significant) and the longer vessels have much more data, so more information can be used for the classification. From these first results it appears that the algorithm applied to the whole image is not as reliable as in the AVR ROI (table 4.2). This should not come as a surprise, because of the greater variability in the whole image as compared to the ROI and because no information about the vessels layout and classification of adjacent vessels can be exploited.

In table 4.4 results regarding the usage of vessels connectivity constraints are shown, in particular the contribution of the crossings and bifurcations automatic detection. If no significant differences can be noticed for the two Mongolia datasets among the simple P_v, the $Cr.P_v$ (crossings are considered) and the $Bif.Cr.P_v$ (also bifurcations are considered), for the DRIVE dataset the improvement is remarkable. The reason should be ascribed again to the poorer image quality of the DRIVE dataset: color and other local features are not so informative as the relationships between vessels in connection and crossings, which become determinant for the final vessel classification.

In table 4.5 the results about the P_v weighted for the caliber and/or length are presented, in particular in the case crossing constraints are considered. In a "vessel cloud" of crossing vessels their P_v can have the same weigh or those correspondent to larger and/or longer vessels (where usually the classification is easier) can make a stronger contribution. The results confirm that the "weighted" solution appears the best one, in particular if vessels are weighted for their length (or for both their length and caliber).

Finally in table 4.6 the best performing implementations previously deter-

mined have been merged into a single solution: both bifurcations and crossings are considered and the P_v are weighted for the vessel caliber and length. Results have been reported for the Mongolia (single images) and the DRIVE dataset, both in terms of mean and median. The median is much higher than the mean, because for each dataset a very difficult image is present, where the main arteries and veins appear very similar (Fig. 4.10). For both datasets, the median has values greater than 0.8, in particular, for the Mongolia one, the algorithm has shown a sensitivity (veins) of 0.82 and a specificity (arteries) of 0.83, and for DRIVE they reach respectively a value of 0.81 and 0.89. It is important to notice that despite the difference between the 2 datasets, the algorithm performs in a similar way, confirming its "portability" feature not only in the AVR ROI but also in the entire image. It has to be reminded that this performance refer to a vascular network correctly segmented but where the detection of bifurcations and crossings is obtained with the previously described automatic algorithm. In table 4.6 it can be seen that if also the information about bifurcations and crossings is correct (they have been manually corrected after the automatic detection), the algorithm achieves much better results: a median sensitivity of 0.93 and a median specificity of 0.95 for the Mongolia dataset and a median sensitivity of 0.88 and a median specificity of 0.91 for the DRIVE dataset.

In figure 4.11 the resulting final AV classification for 2 images belonging to the MONGOLIA and DRIVE datasets are shown and classifications performed with the automatic and manual bifurcations and crossings detection are compared. In figure 4.12 the ground truth and final automatic AV classification of a "registered" Mongolia image are shown.

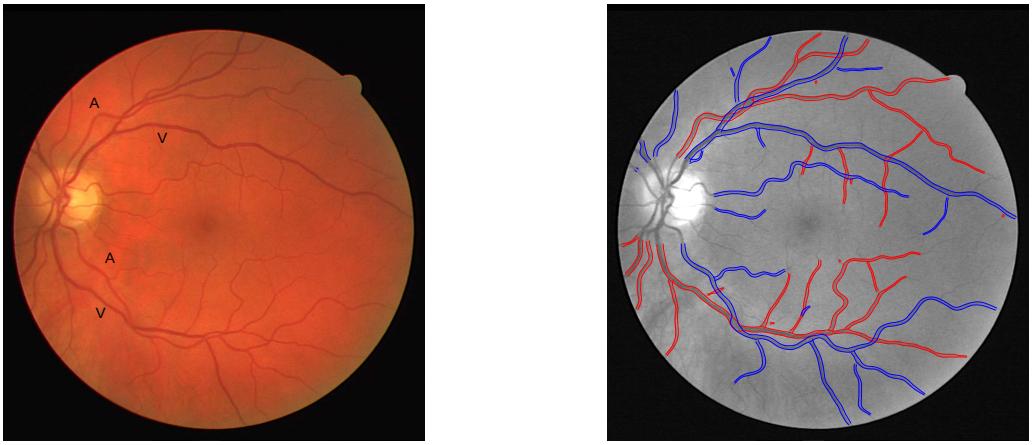

(a) (b)

Figure (4.10). *The automatic AV classification for the* 5_{th} *image from the training DRIVE dataset. This is the most difficult image to analyze because of the slight differences between arteries and veins. The algorithm fails for the vessels in the inferior temporal part of the image.*

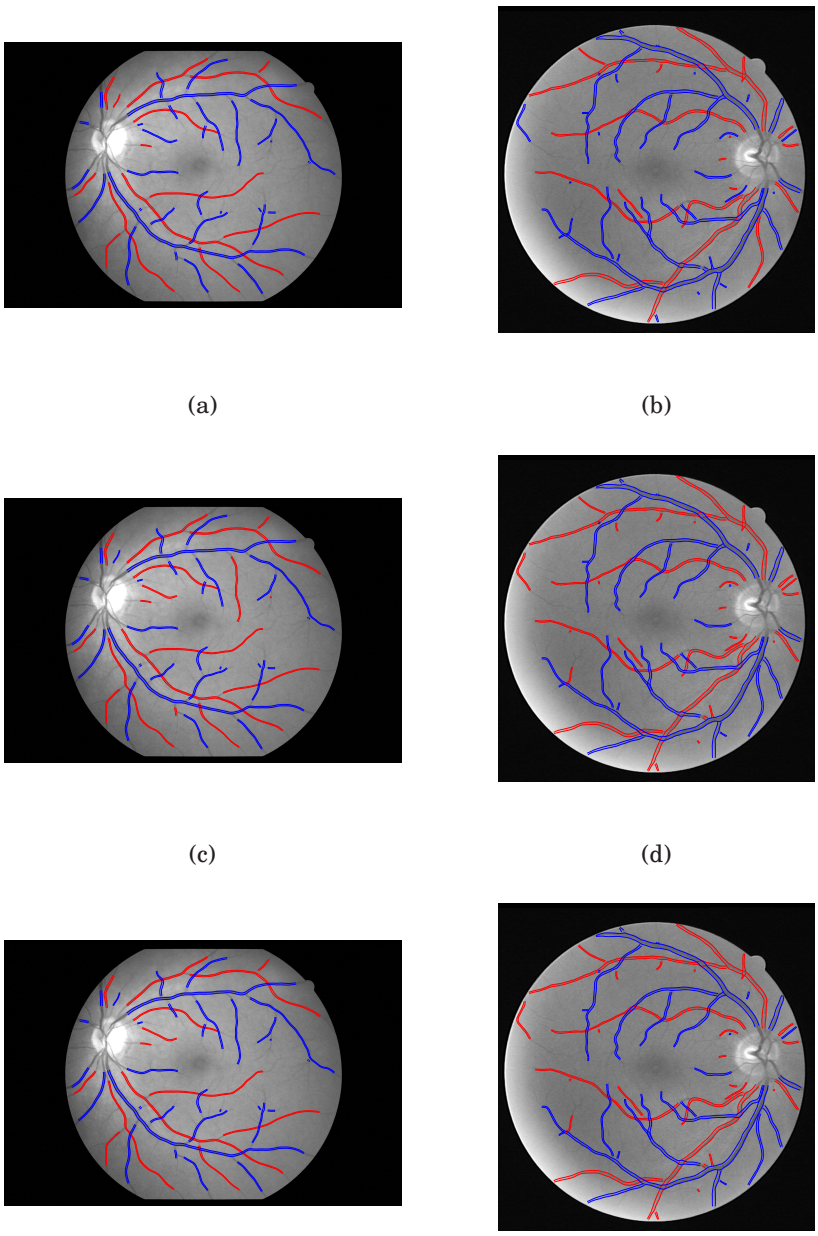

(a) (b)

(c) (d)

(e) (f)

Figure (4.11). *The AV classification in an image of the MONGOLIA dataset (left) and of the DRIVE dataset (right). The upper images show the ground truth (a and b), the central ones the automatic AV classification exploiting the automatic detections of crossing sa nd bifurcations (c and d), the lower ones the automatic AV classification in the case of a manual bifurcation and crossing detection.*

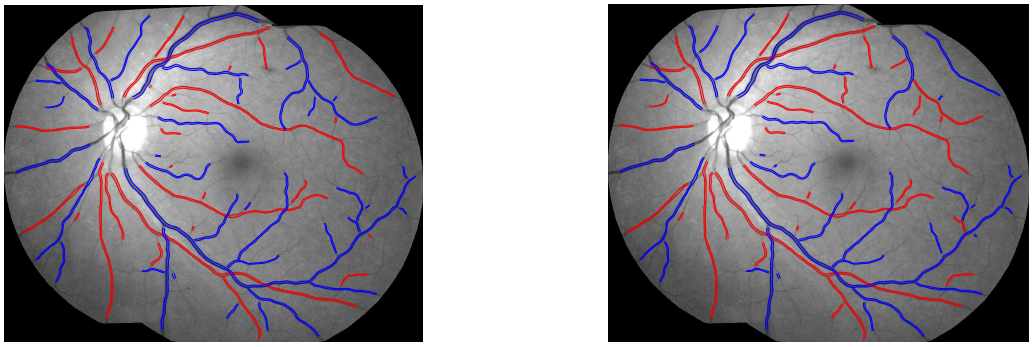

(a) (b)

Figure (4.12). *The ground truth and the automatic AV classification for an image obtained from the registration of two MONGOLIA images.*

Dataset		**Sens.** Pv	**Spec.** Pv	**Sens.** Pv^{w_d}	**Spec.** Pv^{w_d}	**Sens.** $Pv^{w_{dl}}$	**Spec.** $Pv^{w_{dl}}$
MONGOLIA	mean [px] ($\pm$ CI 95%)	0.73 ($\pm$ 0.12)	0.81 ($\pm$ 0.24)	0.73 ($\pm$ 0.12)	0.79 ($\pm$ 0.23)	0.74 ($\pm$ 0.10)	0.82 ($\pm$ 0.24)
(single image)	mean [ves] ($\pm$ CI 95%)	0.57 ($\pm$ 0.12)	0.72 ($\pm$0.22)	0.57 ($\pm$ 0.12)	0.70 ($\pm$ 0.21)	0.58 ($\pm$ 0.10)	0.72 ($\pm$ 0.22)
MONGOLIA	mean [px] ($\pm$ CI 95%)	0.71 ($\pm$ 0.04)	0.83 ($\pm$ 0.03)	0.70 ($\pm$ 0.04)	0.82 ($\pm$ 0.03)	0.72 ($\pm$ 0.04)	0.84 ($\pm$ 0.03)
(registered images)	mean [ves] ($\pm$ CI 95%)	0.66 ($\pm$ 0.04)	0.78 ($\pm$ 0.04)	0.66 ($\pm$ 0.04)	0.78 ($\pm$ 0.04)	0.67 ($\pm$ 0.04)	0.79 ($\pm$ 0.04)
DRIVE	mean [px] ($\pm$ CI 95%)	0.59 ($\pm$ 0.08)	0.73 ($\pm$ 0.14)	0.61 ($\pm$ 0.09)	0.71 ($\pm$ 0.14)	0.58 ($\pm$ 0.08)	0.70 ($\pm$ 0.12)
	mean [ves] ($\pm$ CI 95%)	0.44 ($\pm$ 0.09)	0.67 ($\pm$ 0.13)	0.45 ($\pm$ 0.10)	0.66 ($\pm$ 0.12)	0.43 ($\pm$ 0.09)	0.66 ($\pm$ 0.10)

Table (4.3). *Artery-Vein Classification Results: how the P_v of the single segments belonging to different ROIs are integrated to get the final P_v of the vessel*

Dataset		**Sens.** Pv	**Spec.** Pv	**Sens. Cr.** Pv	**Spec. Cr.** Pv	**Sens. Bif.Cr.** Pv	**Spec. Bif.Cr.** Pv
MONGOLIA	mean [px] ($\pm$ CI 95%)	0.73 ($\pm$ 0.12)	0.81 ($\pm$ 0.24)	0.79 ($\pm$ 0.12)	0.79 ($\pm$ 0.24)	0.73 ($\pm$0.22)	0.77 ($\pm$0.30)
(single image)	mean [ves]	0.57 ($\pm$ 0.12)	0.72 ($\pm$0.22)	0.63 ($\pm$ 0.13)	0.74 ($\pm$ 0.22)	0.68 ($\pm$ 0.18)	0.77 ($\pm$0.26)
MONGOLIA	mean [px]	0.71 ($\pm$ 0.04)	0.83 ($\pm$ 0.03)	0.75 ($\pm$ 0.04)	0.79 ($\pm$0.04)	0.74 ($\pm$ 0.04)	0.74 ($\pm$ 0.04)
(registered images)	mean [ves] ($\pm$ CI 95%)	0.66 ($\pm$ 0.04)	0.78 ($\pm$ 0.04)	0.71 ($\pm$ 0.04)	0.78 ($\pm$ 0.04)	0.70 ($\pm$ 0.04)	0.70 ($\pm$ 0.04)
DRIVE	mean [px] ($\pm$ CI 95%)	0.59 ($\pm$ 0.08)	0.73 ($\pm$ 0.14)	0.62 ($\pm$ 0.10)	0.68 ($\pm$ 0.17)	0.77 ($\pm$ 0.09)	0.79 ($\pm$ 0.13)
	mean [ves] ($\pm$ CI 95%)	0.44 ($\pm$ 0.09)	0.67 ($\pm$ 0.13)	0.48 ($\pm$ 0.09)	0.66 ($\pm$ 0.14)	0.64 ($\pm$0.06)	0.73 ($\pm$ 0.14)

Table (4.4). *Artery-Vein Classification Results: the contribution of the automatic detections of crossings (Cr. Pv) and bifurcations (Bif.Cr. Pv)*

Dataset		**Sens. Cr.**Pv	**Spec. Cr.**Pv	**Sens. D-Cr.**Pv	**Spec. D-Cr.**Pv	**Sens. L-Cr.**Pv	**Spec. L-Cr.**Pv	**Sens. DL-Cr.**Pv	**Spec. DL-Cr.**Pv^{w_l}
MONGOLIA	mean [px]	0.79 (± 0.12)	0.79 (± 0.24)	0.80 (± 0.12)	0.82 (± 0.25)	0.83 (± 0.08)	0.85 (± 0.25)	0.83 (± 0.08)	0.85 (± 0.25)
(single im.)	mean [ves]	0.63 (± 0.13)	0.74 (± 0.22)	0.65 (± 0.12)	0.75 (± 0.23)	0.67 (± 0.09)	0.76 (± 0.23)	0.67 (± 0.09)	0.76 (± 0.23)
MONGOLIA	mean [px]	0.75 (± 0.04)	0.79 (±0.04)	0.75 (± 0.04)	0.81 (± 0.04)	0.77 (± 0.04)	0.84 (± 0.03)	0.76 (± 0.05)	0.84 (± 0.04)
(regist. im.)	mean [ves]	0.71 (± 0.04)	0.78 (± 0.04)	0.71 (±0.04)	0.79 (± 0.04)	0.73 (± 0.04)	0.79 (± 0.04)	0.72 (± 0.04)	0.79 (± 0.04)
DRIVE	mean [px]	0.62 (± 0.10)	0.68 (± 0.17)	0.67 (± 0.10)	0.72 (± 0.17)	0.67 (± 0.10)	0.73 (± 0.17)	0.68 (± 0.11)	0.75 (± 0.18)
	mean [ves]	0.48 (± 0.09)	0.66 (± 0.14)	0.50 (±0.09)	0.69 (± 0.14)	0.50 (± 0.09)	0.69 (± 0.14)	0.52 (± 0.09)	0.70 (± 0.15)

Table (4.5). *Artery-Vein Classification Results: at crossings the P_v can be weighted for the vessel caliber and/or length.*

Dataset		**Sens.** Pv	**Spec.** Pv	**Sens. DL-Bif.Cr.** Pv	**Spec. DL-Bif.Cr.** Pv	**Sens. Man. DL-Bif.Cr.** Pv	**Spec. Man. DL-Bif.Cr.** Pv
MONGOLIA	mean [px]	0.73 (± 0.12)	0.81 (± 0.24)	0.73 (± 0.21)	0.77 (± 0.28)	0.83 (± 0.18)	0.86 (± 0.28)
(single image)	median [px]	0.73	0.82	**0.82**	**0.83**	**0.93**	**0.95**
	mean [ves]	0.57 (± 0.12)	0.72 (±0.22)	0.68 (±0.17)	0.77 (±0.24)	0.77 (±0.18)	0.86 (±0.25)
	median [ves]	0.55	0.75	0.71	0.79	0.86	0.91
DRIVE	mean [px]	0.59 (± 0.08)	0.73 (± 0.14)	0.76 (± 0.14)	0.82 (± 0.18)	0.81 (± 0.16)	0.84 (± 0.19)
	median [px]	0.60	0.80	**0.81**	**0.89**	**0.88**	**0.91**
	mean [ves]	0.44 (± 0.09)	0.67 (± 0.13)	0.62 (± 0.10)	0.77 (± 0.16)	0.69 (± 0.13)	0.80 (± 0.19)
	median [ves]	0.45	0.76	0.62	0.84	0.71	0.86

Table (4.6). *Artery-Vein Classification Results: manual bifurcations and crossings detection*

Chapter 5

The AVRnet WEB-based system

One of the first diagnostic signs in retinopathy from hypertension and diabetes is the generalized arteriolar narrowing, expressed by the clinical index AVR (Arteriolar Venular Ratio). This measure permits the early diagnosis of both the hypertensive and diabetic retinopathy as well as their pharmacologic treatment follow-up. It is calculated as the ratio between the CRAE (Central Retinal Arteriolar Equivalent) and CRVE (Central Retinal Venular Equivalent), which estimates caliber of arteries against caliber of veins, these latter less subject to diameter changes [64], [57]. The Knudston formulas to calculate the AVR parameter consider vessels in a circular Region Of Interest (ROI) centered at the optic disk and take into account only the six largest arteries and the six largest veins [5]. The AVR parameter is not commonly utilized in a clinical context and difficulties are present also in a research context, because of the lack of a fast, precise and accurate tool. IVAN is the most popular software used for this purpose, but the time for the analysis of a single image is about 20 minutes, too long to allow its use it in screening studies or to become a standard in clinical practice [65]. Moreover, IVAN needs well-trained graders, because some operations have to be manually performed: correcting vessel traced profiles and classifying vessels in arteries and veins. In addition, this tool has not been conceived to be used in a telemedicine context.

In this chapter we present a fast and accurate system that requires minimal manual intervention: the AVRnet tool [63]. An additional benefit of the proposed system is that it is designed as a client-server application: a client program interacts with a centralized server application allowing to choose images, perform vascular tracking, manually set parameters, and compute clinical indexes. In particular, clinicians and researchers interested in the measurement or validation of clinical indexes will be able to work remotely with the system through an internet connection. Additional advantages are the possibility of exploiting multiple processors for parallel operations, the availability in any operating system, and the centralized software upgrade.

After this work has been published [63] other two web-based systems have been presented: the Sirius [66] and the VAMPIRE [67] tools. The first one implements a web-based solution for the analysis, management and understanding of retinal images and The first service available deals with the microcirculation analysis in the retinal vessel tree, in particular, an automated method for AVR computation. Nevertheless this tool does not provide an automatic classification of arteries and veins. VAMPIRE is a web-based system developed not to the specific AVR computation: it allows the optic disc location, followed by the determination of the geometry at vessel bifurcations, the tortuosity of major vessels, the vessel width estimation and the branching complexity (through fractal dimension) of the vasculature. This system is under a further validation.

In the next chapter also a web-based system for the image tortuosity estimation will be presented. The two systems has been conceived with the same structure, with the idea that they could constitute different modules of a unique system. It can integrate information from the different parameters to provide the final diagnosis or just some modules can be exploited, depending on the user's needing.

5.1 Methods

The proposed system is composed of three modules:

1. an algorithm for the vascular tracking, which detects the structure and

characterizes the morphology of the vascular tree (we implemented the tracking algorithm described in chapter 4);

2. an interactive editing interface, which allows the user to set the required parameters of analysis, highlights critical situations, and, when necessary, helps in the correction process;

3. the analysis algorithm, which takes into account the settings entered by the user and, according to the vascular tracking information, computes the clinical parameters.

The system was organized as a client-server structure.

5.1.1 Graphical User Interface

The proposed system interacts with the user by means of a Graphical User Interface (GUI)(Fig. 5.1): it is composed of an editing and a display panel. The first contains editing commands and a display where useful information is shown (e.g. solutions proposed by the system, helping information, results). The second shows the entire image or zoomed parts of it. At the beginning, the user is prompted to input the scale factor (μm/pixel) and to locate the optic disk.

The GUI was designed according to the following rationale:

1. to highlight critical situations (e.g. tracking errors);

2. to propose possible solutions;

3. to limit the number of user operations;

4. to allow fast and easy operation;

5. to allow editing any result.

Therefore the display panel shows only vessels that do not cross completely the ROI widthways, i.e. short vessels either not connected to other ones (and therefore probable false vessels) or vessels with tracking errors. Short vessels could also be branches at a bifurcation: this situation is recognized and proposed to the user, who may confirm it or not. To correct tracking

errors, the user can edit the results just by clicking on the appropriate command: to eliminate a false vessel, to cut an erroneously tracked part of vessel, to split a vessel in two, or to link one vessel to another. Eventually, the user can even trace, with the aid of a custom tool (Fig. 5.1), the vessel borders themselves.

After the guided correction step, the entire image is displayed and the user can select the erroneously tracked vessels that have not been corrected yet, simply by clicking on them. In the final step the user can add those vessels that were not tracked at all by the automatic procedure.

In the final step, the artery/vein classification is performed. As described in [68], the discriminant feature used is the central reflex, which is more evident in arteries than in veins. The classification result is shown on the display panel, where arteries are shown in red and veins in blue. As usual, the user can modify the class of a vessel by simply clicking on it.

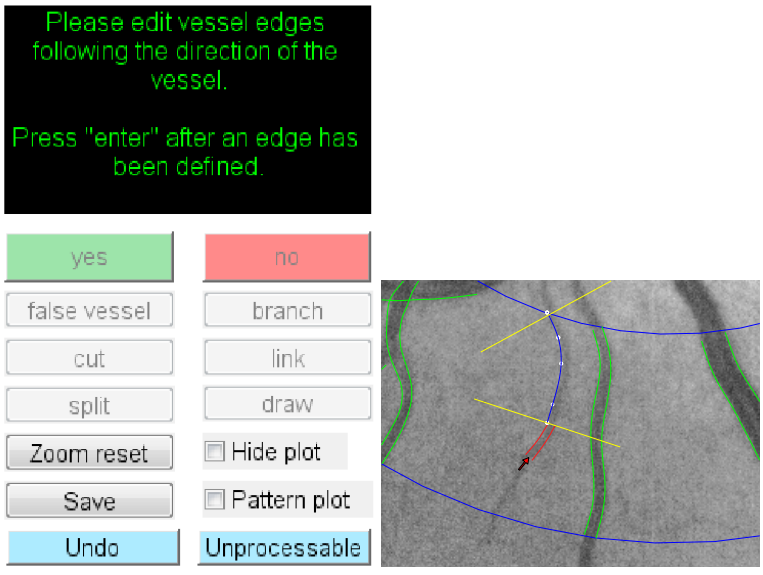

(a) (b)

Figure (5.1). *The GUI interface during the editing of a vessel: a) the panel suggests to the user how accomplish the operation; b) the vessel analyzed is highlighted in red. Five points have been drawn by the user to define the vessel left border, next the tool identifies it by interpolating the points with a spline.*

5.1.2 Clinical Index Extraction

The estimation of the clinical parameters of interest (CRAE, CRVE, AVR) is done according to the Knudston formulas [5]. These results and the final image (with colored veins and arteries) are shown on the screen (Fig. 5.2) and saved in a folder as Excel file and as an image file with format selected by the user.

5.1.3 Client-Server System Architecture

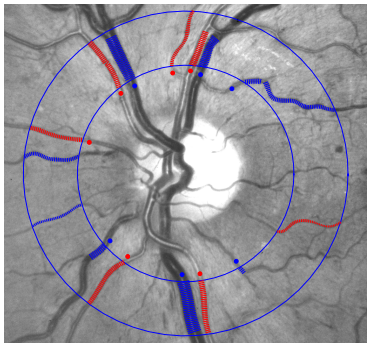

Figure (5.2). *Screen image showing the vein/artery classification (arteries in red and veins in blue), and the resulting CRAE, CRVE, and AVR values.*

The system was created as a client-server application (Fig. 5.3). The encrypted communication between the client-side programs and the server-side software is obtained by interfacing *Java* and *PHP* technologies. When the application starts, the user is required to authenticate, in order to enable a connection with the server and to setup data storage. For every user authenticated, a *PHP* session is created on the server, with unique identification number for each visitor and storing variables based on this ID. This allows to safely manage multiple simultaneous accesses. The user can select one or more retinal images from the local drivers, by means of a *Java* GUI that navigates the local file system: no constrain on image resolution, format or acquisition source is present. Images are sequentially sent to the server, where they are stored and analyzed by the fully automatic vascular tracking procedure. After the vessel tracking on each image is completed, the server sends a message to the client, including a secure link to the address where tracking

results were stored and the client program automatically proceeds to download the files to the user machine.

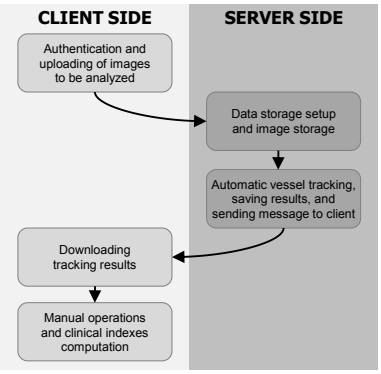

Figure (5.3). *Client/server system framework.*

An intuitive GUI is installed on the client machine, which allows the user to manually check and correct the vessel tracking results (see sec. 5.1.1), in order to obtain final clinical parameters estimation. This process does not need interaction with the server.

5.2 Results

Thirty color fundus images were acquired with a commercial fundus camera in normal healthy subjects, according to the NM1 standard [69]: 50° field focused centrally between the temporal margin of the optic disc and the center of the macula. The image size is 1664x1664 pixels.

In order to assess the reproducibility of the measures provided by the system, we had three graders use the system and independently grade each of the 30 images of our dataset. *Pearson's correlation coefficient* and the *p-value* of a paired t-test were computed for each pair of graders. The first provides a measure of the linear association between each grader, while the latter checks that the results provided by each grader are not biased. Since the two tests are complementary, they provide a good evaluation of the measures reproducibility.

Table 5.1 shows that the correlation between the three graders (columns 2-4) is at least 0.84, indicating that the three graders' assessment is coherently associated in the whole AVR value range. The p-value (columns 5-7) is at least

Table (5.1). *Repeatability of the AVR values measured by three graders.*

	Pearson's correlation coefficient			P-value			Average time
	Grd.1	Grd.2	Grd.3	Grd.1	Grd.2	Grd.3	(sec.)
Grd.1	-	0.87	0.84	-	0.17	0.36	265
Grd.2	0.87	-	0.86	0.17	-	0.67	244
Grd.3	0.84	0.86	-	0.36	0.67	-	289

0.17, indicating that the mean of the distribution of the measures provided by the three graders are not significatively different (Fig. 5.4).

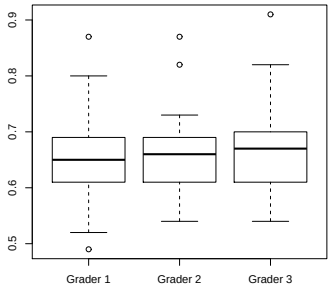

Figure (5.4). *Box plot of AVR values measured by three graders.*

5.3 Conclusion

The system we propose can provide an objective and reproducible measurement of important clinical diagnostic parameters. A more extensive clinical evaluation is in progress on both normal and pathological subjects.

An adequate number of patients will be identify for each pathology of interest, at various severity levels. These patients will undergo a clinical analysis performed along the conventional diagnostic procedure. They will then be examined with the proposed system, and the diagnostic outcomes of the current and proposed system will be compared to assess their level of agreement. The benefits provided by the proposed system in terms of diagnostic capabil-

ities, overall efficacy, and reproducibility, as well as usability, flexibility, and portability, will be further assessed.

The extracted vascular network can be analyzed both for the quantitative measurement of parameters already qualitatively evaluated in conventional clinical practice, and for the assessment of novel measurements, whose correlation with known pathologies can be the goal of future clinical research.

The additional benefit of the proposed system is the possibility of using it through an internet connection: clinicians and researchers interested in the measurement or validation of clinical indexes will be able to work remotely with the system, and assessments will be possible even without the presence of physicians at the care center unit. At present, a beta version of the system is hosted at the website http://bioimlab.dei.unipd.it; it is under beta testing and will be soon publicly available.

Chapter 6

The vascular tortuosity estimation and the TorTnet system

In this last chapter a study concerning the tortuosity parameter is presented. It has been observed that in different pathological situations one of their effects is an increased vessel tortuosity, nevertheless this behavior, in particular in the case of diabetes, has not been clearly understood and reliably demonstrated, basically because a consistent quantitative measure of tortuosity and tools to measure it in an automatic way, do not exist yet. Until now the tortuosity has been evaluated by the graders using a qualitative scale (e.g. mild, moderate, severe, extreme [47]) but a reliable quantitative measure would enable the retinal vascular tortuosity and its progression to be more easily concerned. During the studying period at the Moorfields Eye Hospital the collaboration with the doctors and graders of the Reading Center allowed to investigate about their actual perception of vessels tortuosity and about the diagnostic value of this parameter, until now not really considered in the normal clinical practice.

6.1 Introduction

Recently there has been increasing interest in retinal vessel tortuosity [70]-[71], which might not only be sensitive to early hemodynamic changes in diabetes [72], but is also more observable than other retinal vascular parameters [47]. Sasongko et al. found that retinal arteriolar tortuosity is associated with high HbA1c, even before the presence of retinopathy [70] and they have recently demonstrated that the retinal arteriolar tortuosity is independently associated with mild diabetic retinopathy and early stage of nephropathy in type I diabetes [71]. This suggests that variations in retinal vessel tortuosity may indicate early pathologic changes before the clinical manifestation of diabetic microvascular complications. Taarnhoj et al. [73] in a study with twins found that heritability of tortuosity accounts for 82% with unshared environmental factors accounting for the remaining 18% and that increasing values of mean arterial blood pressure and body mass index were both associated with decreasing levels of retinal arterial tortuosity. Dougherty in [74] measured the vessels tortuosity in three retinal pathologies and discovered that in the retinitis pigmentosa it is significantly higher than for normal vessels, in the diabetic retinopathy it is higher and in the vasculitis it is lower. Even if the tortuosity is a valuable feature in diagnosing any of these three conditions, it is only likely to be successful as a screening test for retinitis. Moreover retinal vessel tortuosity has been associated with the retinopathy of prematurity (ROP), due to the exposure to factors in the extrauterine environment, including higher relative oxygen levels, that disrupts the normal process of retinal vascular development [75].
Despite the many verifications about the diagnostic power of the tortuosity, it is not clearly understood its behavior, in particular in the case of diabetes (and in type II it is still really confused), and most previous studies [72]- [73] have used subjective methods to assess retinal vessel tortuosity, which are imprecise and prone to measurement errors. Hence, it is commonly shared the needing of a standardized quantitative measure for this parameter and of a tool providing it in a reproducible and reliable way [47]. In the next paragraph a summary of the most reliable measures of the vessel tortuosity is presented.

6.1.1 Measures of tortuosity

Various tortuosity measures have been proposed in the literature, but all fail in certain respects. In this section we will review the available methods for evaluating retinal vessel tortuosity, presenting some counterexamples in which these methods provide results that do not match with clinical perception.

Arc Length over Length Ratio

The simpler and most widely used measure of a vessel tortuosity is the ratio between its length and the length of the underlying chord [47]. The idea of using this ratio is that the greater the value of the ratio, the more distant the vessel is from a straight line, i.e., the more tortuous it is. Unfortunately, being the surface of the retina close to a semi-sphere, the non-tortuous paradigm should be the circle arc. In fact, every vessel that has a constant and small curvature, regardless of the amplitude of the arc it describes (as for the main retinal vessels), will be regarded by an ophthalmologist as characterized by negligible tortuosity. Moreover, it is shown in Figure 6.1 that two vessels with very different tortuosity have the same arc length over length ratio measure.

Measure Involving Curvature

Hart [47] presented a number of tortuosity measures that involve the use of the integral of the absolute curvature or of the squared curvature. For a curve $(l) = [x(l), y(l)] : D \subset \Re \rightarrow \Re^2, s \in C^1(\Re)$, with l the curvilinear coordinate on it, the curvature $C_s(l)$ is:

$$C_s(l) = \frac{\dot{x}(l)\ddot{y}(l) - \ddot{x}(l)\dot{y}(l)}{\sqrt{(\dot{x}^2(l) + \dot{y}^2(l))^3}} \tag{6.1}$$

The idea behind this is that this integral should be a measure of the variability of vessel direction. However, the example presented in Figure 6.1 shows that a smaller curvature integral may correspond to a greater perceived tortuosity. In our opinion, there are three main reasons for this result.

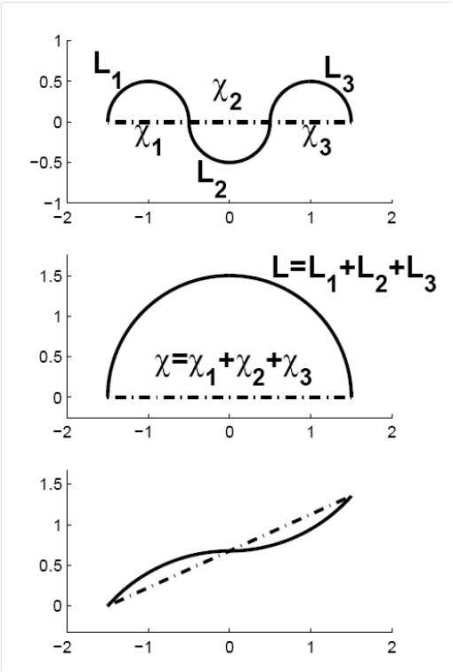

Figure (6.1). *The first two curves (top and middle panel) have very different tortuosity but the same Length L and Chord Length χ. The second and last curves (middle and bottom panel) have the same average angular difference despite their different tortuosity. The curve in the bottom panel has a curvature integral of $\pi/2$ whereas the one in the middle panel has curvature integral π, even if that in the bottom panel is clearly perceived as more tortuous.*

The first is that curvature is non zero only along arcs, while it is negligible along straight or almost straight segments; but straight segments together with arcs dramatically change the tortuosity appearance. The second is that changes in convexity (curvature sign) of the curve are not taken into account, while these are instead the features predominantly taken into account by expert graders to assess tortuosity. Finally, integrating along domain, possibly different in dimension, yields to measures depending on the aforesaid dimension. The ratios between the absolute curvature integral (or the squared curvature integral) and chord length (or vessel length) have been proposed to circumvent the latter point, but still the other two problems remain open with this definition of tortuosity.

To overcome these problems our research group proposed in [76] a new tortuosity measure evaluating the number of vessel twists (changes in convexity or curvature sign), and the size of the amplitude of each of the recognized twists. Firstly the vessels centerlines are interpolates with a spline curve s in order to describe the vessels between sampling points and to filter the noise. After that we decompose any curve into a set of consecutive segments of constant curvature sign. Having defined the curvature of a curve as in 6.1, we define subsegment s_i as a "turn curve" if:

$$[C_{s_i}(l) \geq 0, \forall l \in D] \bigvee [C_{s_i}(l) \leq 0, \forall l \in D] \tag{6.2}$$

In real images, it is common to find small oscillations (changes of convexity with very small amplitude) around the main vessel direction, due to the presence of noise, thus an hysteretic threshold on curvature was used to deal with them. To evaluate tortuosity, we also need the Chord Length L_χ of a curve, defined as the distance between its two extremes:

$$L_s = \|s(max(D)) - s(min(D))\| \tag{6.3}$$

and the Curve Length L_c, defined as:

$$L_c = \int_{min(D)}^{max(D)} \left\| \frac{\partial s}{\partial l} \right\| dx \tag{6.4}$$

Once a curve $s(l)$ is divided into n turn curves

$$s_i : s = s_1 \bigoplus s_2 \bigoplus ... \bigoplus s_n \tag{6.5}$$

the measure of vessel tortuosity proposed is:

$$\tau(s) = \frac{n-1}{n} \frac{1}{L_c} \sum_{i=1}^{n} \left[\frac{L_{csi}}{L_{\chi si}} - 1 \right] \tag{6.6}$$

This tortuosity measure has a dimension of $1/length$ and thus may be interpreted as a tortuosity density, allowing its comparison on vessels of different length. It is worth noting that when n is equal to 1 then τ is equal to 0 and thus vessels with a constant convexity have zero tortuosity.

When an automatic tracking algorithm is employed, a non length-normalized formulation can be taken into consideration. In this situation the vessel network could be tracked in a discontinue way and the tortuosity assessment of the short, high-tortuous vessels could be consequently underestimated. Thus, a slightly different measure of tortuosity can be employed:

$$\tau'(s) = L_c \tau(s) = \frac{n-1}{n} \sum_{i=1}^{n} \left[\frac{L_{csi}}{L_{\chi si}} - 1 \right] \tag{6.7}$$

Recently Trucco et al. [77] suggested that the clinical perception of tortuosity may depend on factors beyond geometric properties of the vessel axis, in particular its caliber could play an important role. Their hypothesis is based on the observation that thicker vessels have thicker walls than thinner ones; hence achieving a given skeletal curvature requires more effort for thicker vessels than for the thinner ones. They defined a measure combining curvature and thickness, expressed by the p-mean root of the averaged p-powers of the curvatures of pairs of corresponding boundary points:

$$\tau_t(\kappa_{B1}, \kappa_{B2}, p) = \left(\sum_j \frac{|\kappa_{B1}|^p + |\kappa_{B2}|^p}{2} \right)^{\frac{1}{p}} \tag{6.8}$$

Mean Direction Angle change

The measure of tortuosity based on local directional changes of the vessel has been proposed by Chandrinos et al. [78]. It computes the average of the angles between sample points describing the vessel. For each point i of the vessel,

it computes the unit vectors from the previous step point d_{i-step} and to the subsequent point d_{i+step}:

$$ad_s = \frac{1}{L_c - 2step} \sum_{i=1}^{n} \alpha_i = \frac{1}{L_c - 2step} \sum_{i=1}^{n} \arccos(d_{i-step} * d_{i+step}) \tag{6.9}$$

In addition to the high sensitivity to noise, deriving from both from the digital quantization and the vessel extraction technique, this suffers from the problems mentioned above. Even the simple example of Figure 6.1 shows that a vessel with constant curvature, such as a semi-circumference, and a vessel formed by the juxtaposition of two arcs of circumference have the same average angle variation, despite their difference in tortuosity.

Until now many tortuosity measures have been proposed [47] [76] [77] [74], although none has been world-wide accepted as the "gold-standard", first of all because the tortuosity is not defined quantitatively in the medical literature. Secondly the role of tortuosity within diagnosis is hardly quantitative, since tortuosity is one of several pieces of information concurring to form a decision. Thirdly most studies compare automatic results with the answer of a single clinician and when more graders are involved, their perception about the tortuosity does not highly agree. For example in [79] two graders have been asked to grade the level of tortuosity of 387 vessels segments of the retina, using a scale from 0 to 5: they agreed in 56% of all grades and a further 42% differed by one grade.

All the studies above cited about the automatic reproducing of the clinical tortuosity perception, refer to the single vessel unit, but a measure of the global tortuosity of the eye has not been proposed yet. In our study we firstly investigated the clinical perception of the tortuosity of the whole retina, then we formulated a measure of the tortuosity matching with the graders' judgements and finally we developed a web based tool for the tortuosity estimation. The different activities rely strictly on each other: if graders do not share a common clear idea of vessels tortuosity and, as a consequence, a measure of this parameter can not be provided, the diagnostic and prognostic power of this parameter can not be established and a suitable tool cannot been provided. Vice versa if a tool is not available, a study on a large scale (so with a

great reliability) can not be undertaken. We start describing the study about the clinical perception of the tortuosity.

6.2 The visual perception about the image tortuosity

Thanks to the collaboration with the Reading Centre, R&D department, at the Moorfields Eye Hospital, it has been possible to study the graders' evaluation and perception of the tortuosity of the whole retina. At first two graders were asked to classify the level of tortuosity in a dataset of 200 images belonging to 50 diabetic Mongolian people (2 images per eye: one with field of view centered on the optic disc and the other on the macula). The dataset has been chosen in order to cover all the complete tortuosity range. The scale used to evaluate the tortuosity comprised 6 levels: mild, moderate low, moderate medium, moderate high, severe and extreme. We preferred subdividing the moderate class in three levels because a preliminary study on a smaller dataset showed that a larger correlation in terms of the Spearman correlation between graders was possible considering more classes. The graders have been asked to classify again the dataset after one month, in order to infer the intra-grader variability. The graders were asked also to order the images from the least tortuous to the most tortuous, because, as graders reported, a common clinical practice is to compare images from the same patient taken in different moments looking for differences in tortuosity. The ordering has been performed with the aid of a software specifically developed for this purpose, allowing the smallest number of comparisons using the merge sort algorithm. The intergraders agreement on the "ordering" method was measured. Finally, also the registered images (resulting from the combination of single images referring to the same eye but with different FoVs) have been graded in order to understand if the average tortuosity value from the images is sufficient to determine the tortuosity of the eye or the registration procedure is needed. The graders were asked to classify the tortuosity of the image just on the basis on their experience, without separating arteriolar and venular tortuosity.

The intragrader variability was evaluated firstly calculating the Pearson

R correlation coefficient (for the classification grading) resulting for the first grader in $R = 0.62$ and for the second one in $R = 0.79$ (average: 0.70) (table 6.1). The two measurements from the first grader agreed in 45 % of the images, differed by 1 class in 40 %, by 2 classes in 12 % and by 3 classes in the further 3%. A mean difference of -0.5 classes between the second and the first time has been measured with a 95% confidence interval of ± 1.85.

For the second grader the two measurements agreed in 47 % of the images, differed by 1 class in 46 %, by 2 classes in 6 % and by 3 classes in the further 1%. The mean difference between the second and the first time has been of 0.17 with a confidence interval of ± 1.72. Considering a scale for the tortuosity with only 4 levels (merging the moderate classes into one) the correlation coefficient decreased in both cases to respectively 0.54 and 0.64, confirming that the intragrader variability is not linked to a too much sensitive scale. These first results show that graders may not have a clear perception of the tortuosity, making the usage of a standardized tortuosity measure necessary. The intergraders variability has been calculated for the classification with the Pearson correlation coefficient and for the ordering method with the Spearman correlation coefficient. Since the classification has been performed twice by each grader, 4 correlation coefficients have been measured and they are reported in table 6.1.

	1st Gr. 1st time	1st Gr. 2nd time	2nd Gr. 1st time	2nd Gr. 2nd time
1st Gr. 1st time	1			
1st Gr. 2nd time	*0.62*	1		
2nd Gr. 1st time	0.79	0.49	1	
2nd Gr. 2nd time	0.96	0.82	*0.79*	1

Table (6.1). *The Pearson Correlation coefficient results: the intra- (in "emphasize" style) and inter-graders variability for the classification of tortuosity.*

Except for the case where R=0.49, the other intergraders correlation coefficients are equal or higher than those regarding the intragraders correlations resulting in an average intersubject correlation of 0.76. The intergraders variability of the ordering method had a Spearman correlation coefficient of 0.69. In figure 6.2 the second grader's ordering versus the first one is plotted: if for very tortuous images the agreement is high, for moderate tortuosity a sparse

cloud is present, suggesting that it is difficult to appreciate qualitatively the differences in the tortuosity between images with medium tortuous vessels or images with both tortuous and non-tortuous vessels. The smaller agreement for the ordering compared to the classification could be partially due also to the difficulty of the ordering on a fairly large amount of images. For these reasons the following analysis has been performed just considering the tortuosity classification and considering as the "true" tortuosity value the average among the 4 classes measures provided by the graders, resulting in values from a continuous domain in the range [1:5].

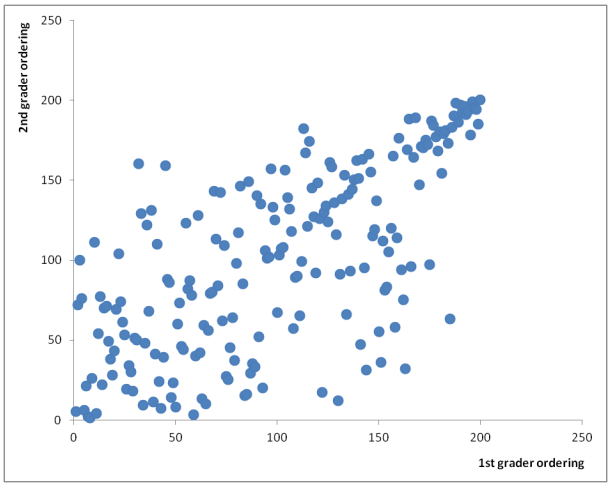

Figure (6.2)

Comparing the tortuosity measures of correspondent images from the same eye but with different FoVs, a correlation coefficient of 0.64 was calculated, which is not significantly lower than those regarding the inter- and intra-variability. Comparing the mean value of each pair of images with the classification of the corresponding "registered" image, a correlation of 0.72 was measured. This value is again not significantly different from those regarding the graders' variability and therefore no conclusions can be drawn regarding the need of the registration procedure. However, the graders themselves indicated a preference for this solution because there might be differences among the different areas of the retina and a single FoV could emphasize some vessels and hide others.

The correlation between the right and left eyes was also calculated: a

value of 0.59 has been obtained, suggesting that the tortuosity could be just partially congenital (and thus similar in both the eyes) and partially due to the pathological condition of the single eye.

6.3 Automatic measures of image tortuosity

After the results about the graders' perception presented above, it was clear that the a computerized measure could not be just a useful help to the diagnosis but it is necessary to allow a standardized, objective and reproducible estimation of tortuosity parameter.

We proposed more measures to express the image tortuosity and, among the best matching the graders'perception, we looked for that with the largest discriminating power between pathological and normal conditions.

Two kinds of measures have been proposed: the first one is based on a *syntactical* approach, the second one on a *local* approach. In the former the image tortuosity is computed as the average tortuosity from single vessel units, in the latter the leading hypothesis is that the vessel unit is not important since local changes in curvature can influence the image tortuosity independently on the vessels involved. The first approach is supposed to reflect better the visual perception of the image and it is supported in literature by encouraging results about the agreement between the vessel automatic tortuosity and the manual expert tortuosity [76] [77]. The second one is more sensitive to noise and it has not been recently applied in studies presented in literature. The problem of the sensitivity to noise can not be relevant because in the analysis of the whole image, the local noise and tracking errors influence just the local estimation of the tortuosity, which is then compensated by the average tortuosity measure. Moreover it does not require the linking procedure between vessel segments, it just need the vessel network segmentation. On the contrary the first approach requires some postprocessing to the tracking step, in order to identify accurately the single vessel units. For example it needs that bifurcations are reliably detected, to avoid that abrupt changes in curvature at these critical points be ascribed to a high vessel tortuosity. Moreover the distinction between bifurcations and ramifications is also required because if in the first case the two branches have to be separated from the trunk, in the

latter the main branch has to be linked to the trunk of which it constitutes the continuation (Figure 6.3).

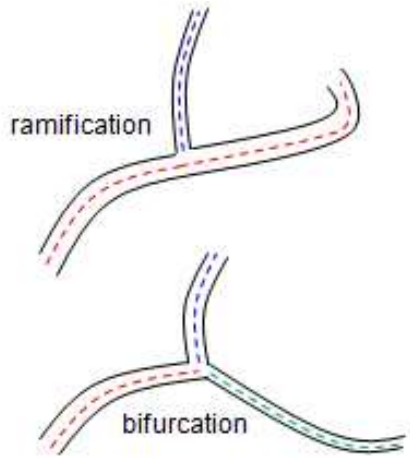

Figure (6.3). *The syntactical approach requires the distinction between ramifications and bifurcations, because in the second case 3 vessels segment (2 branches and the trunk) have to be considered, in the first case just 2: the trunk and the branch*

In the first approach, the measures adopted consider the average vessel tortuosities as defined in 6.7 and 6.6 but and then weight them by the mean vessel caliber, as suggested by Trucco et al. [77], resulting in the two global syntactical measures:

$$T = \frac{\sum_{i=1}^{N} c_i * \tau_i}{\sum_{i=1}^{N} c_i} \tag{6.10}$$

$$T' = \frac{\sum_{i=1}^{N} c_i * \tau_i'}{\sum_{i=1}^{N} c_i} \tag{6.11}$$

where N is the number of vessels in the image.

In figure 6.4 the vessels are highlighted with a color proportional to their tortuosity estimation according the T' formulation.

The second approach considers the direction angle change α_i as defined in 6.9, also in this case weighted for the vessel caliber at the point where the angle change is calculated. Figure 6.5a shows with different colors the different tortuosity values for each vessel centerline point. In particular, the

relation "Tortuosity versus caliber" is considered (Figure 6.5b), where each point refers to a particular vessel centerline sample, the y-coordinate measures the tortuosity (according to α_i) and the x-coordinate the caliber of the vessel at that point. Both the distance from the origin of the barycenter of the distribution and the average $caliber * tortuosity$ are supposed to be suitable measures of the global tortuosity. We denote the first one as T_{bar} and the second one as T_{loc} and they are expressed in formulas as:

$$x_{bar} = \frac{\sum_{i=1}^{M} c_i}{M} \tag{6.12}$$

$$y_{bar} = \frac{\sum_{i=1}^{M} \alpha_i}{M} \tag{6.13}$$

$$T_{bar} = \sqrt{x_{bar}^2 + y_{bar}^2} \tag{6.14}$$

$$T_{loc} = \frac{\sum_{i=1}^{M} c_i * ad_i}{M} \tag{6.15}$$

where M is the total number of vessel centerlines points and α_i is defined as in 6.9.

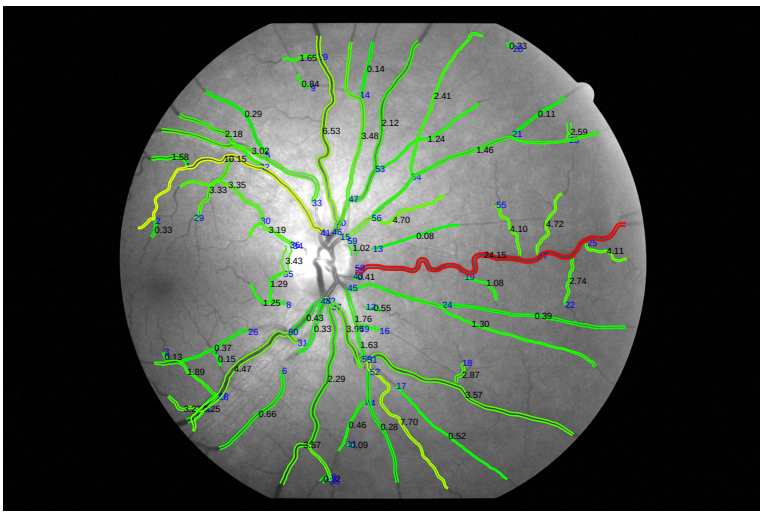

Figure (6.4). *Vessels highlighted with colors proportional to their 'syntactic' tortuosity (scale from blue-low tortuosity- to red-high tortuosity)*

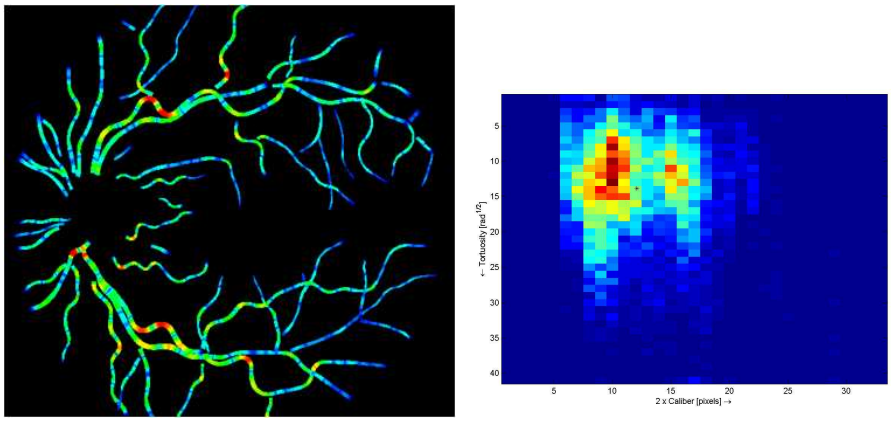

(a) (b)

Figure (6.5). *Vessel points highlighted with colors proportional to their 'local' tortuosity (scale from blue-low tortuosity- to red-high tortuosity)*

6.4 The TorTnet system and its application in the tortuosity study

The measures presented above have been integrated in a system for the the tortuosity estimation: the TorTnet system [80]. It has been conceived as a web-based application with the same structure of the AVRnet system: the user can select one or more retinal images from the local drives, images are sequentially sent to the server, where they are stored and analyzed by a fully automatic vascular tracking procedure. After the vessel tracking on each image is completed, the server sends a message to the client, including a secure link to the address where tracking results were stored and the client program automatically proceeds to download the files to the user machine. In the client machine the postprocessing algorithm starts, then an intuitive interface allows the user to manually check and correct the vessel tracking results. After that, the automatic AV classification algorithm is applied, followed by the user's correction performed just clicking on the wrongly classified vessels. Finally the estimation of the global tortuosity is provided with the different tortuosity measures above presented: their numerical values appears at the GUI display (Fig. 6.7) and figures and graphics, as those in figures 6.8 and 6.9, are provided by the software. Moreover it provides the estimation of the

single arterial and venular tortuosities. After the initial automatic tracking step, the process does not need any more interaction with the server. The different steps are illustrated by the flow chart in Fig. 6.6. The automatic tracking procedure is performed in about 30 seconds and the following whole process in the client machine requires on average 6 min (values in the interval $2 \div 12$ min).

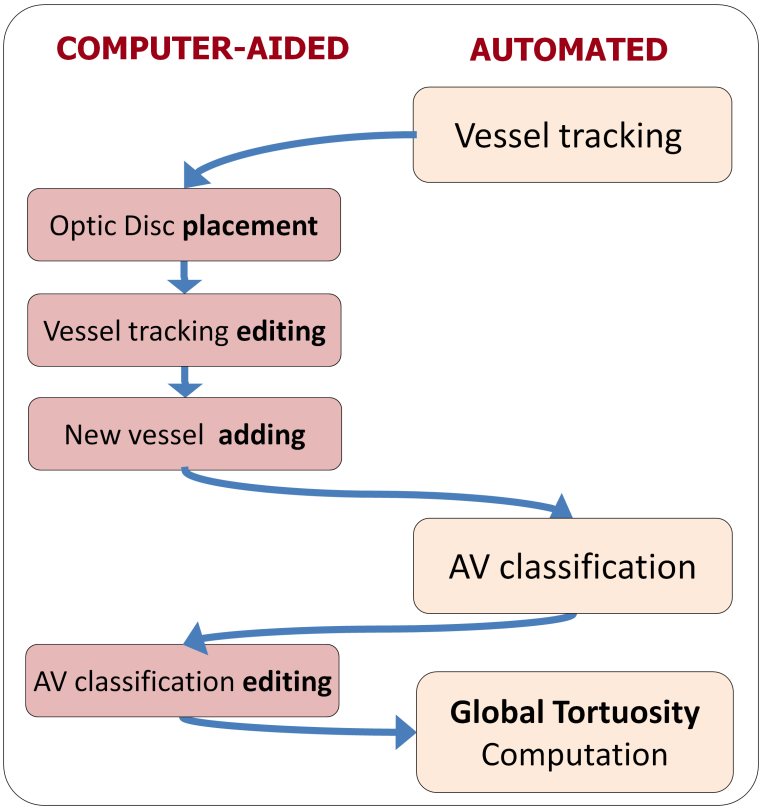

Figure (6.6). *The sequence of steps performed by the TorTnet system for the tortuosity estimation. Some of them are completely automatic, others computer-aided.*

In order to study the correlation between the automatic measures and the manual ones as well as the diagnostic power of the tortuosity parameter, the TorTnet system has been used to analyze the dataset of 100 images composed by the "registered images". The choice of this dataset instead of the single images is justified by the hypothesis that a more reliable measure is inferable considering the whole eye, instead of the single FoVs.

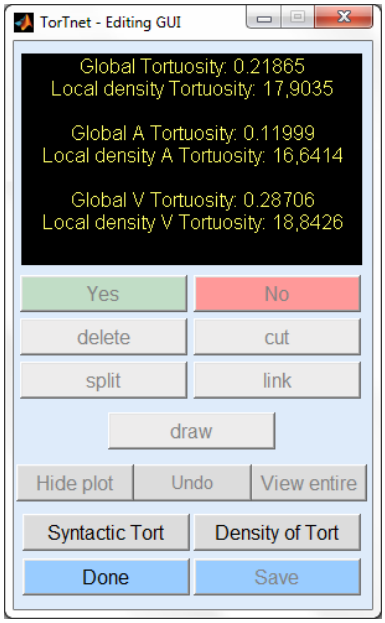

Figure (6.7). *The GUI of the TorTnet system*

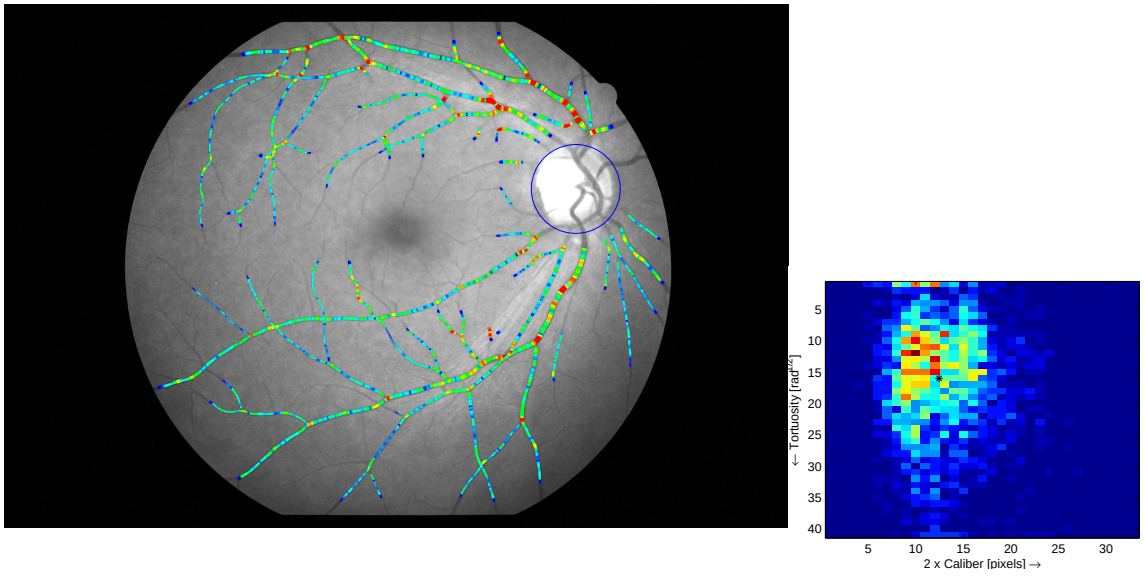

(a) (b)

Figure (6.8). *Images provided by the TorTnet system representing the vessel tortuosity evaluated with the local measure. Vessel samples are colored proportionally to their tortuosity (scale blue to red) (a). For each point the relation between the local measure of tortuosity and the vessels caliber (b)*

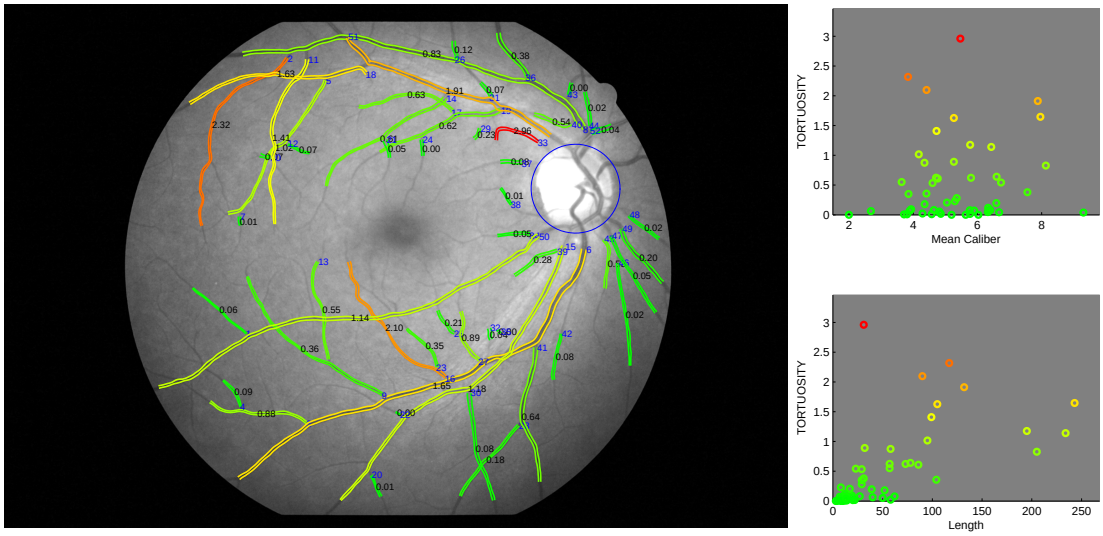

(a) (b)

Figure (6.9). *Images provided by the TorTnet system representing the vessel tortuosity evaluated with the syntactical measure. Vessels are colored proportionally to their tortuosity (scale blue to red) (a). For each vessel the relation between the syntactical measure of tortuosity and caliber (b above) and length (b below)*

In table 6.3 the correlation in terms of the Pearson correlation coefficient between each automatic measure and the manual one considered as the ground truth are reported as well as the correlation between each pair of automatic measures. It is interesting to notice that all automatic measures match in a similar way the clinical perception (R in the interval $[0.56 \div 0.67]$), so on the basis of just this criterion it is difficult to choose the most reliable measure. The correlations are not very high, but they are comparable with those describing the variability between graders and within the same grader, suggesting that these measures could faithfully reproduce the clinical judgements. Moreover it can be noticed that despite their similar correlation with the manual measures, their mutual correlations are not always significant: for example the local tortuosity T_{loc} correlates only 0.35 with the global tortuosity T' and the two local tortuosities T_{loc} and T_{bar} correlate with $R = 0.48$. These results suggest that a single tortuosity measure should not be used and that a combination of the syntactical and local measures should be performed.

	T_{man}	T'	T	T_{bar}	T_{loc}
T_{man}	1				
T'	0.62	1			
T	0.56	0.94	1		
T_{bar}	0.67	0.84	0.86	1	
T_{loc}	0.61	0.35	0.33	0.48	1

Table (6.2). *The Pearson Correlation coefficient R between the tortuosity measures.*

The Tortnet system allowed also to estimate the arteriolar and venular tortuosities separately. The arteriolar and venular tortuosity measurements agree in a similar way with the ground truth ($R_a = 0.53$ and $R_v = 0.55$), suggesting that the graders weighted in the same way the tortuosity from the two kinds of vessels.

All these measures have been used to investigate about the diagnostic power of the tortuosity for the diabetic retinopathy and its linking with other factors such as blood pressure (BP), type of retinopathy, sex, age, duration of the pathology, diet, smoking, insulin, medicines, renal and cardiovascular

problems. Among this group of 50 diabetic patients (100 eyes), the prevalence of the retinopathy is 22%, among these 19% is affected by mild retinopathy (R1) and 3% by moderate retinopathy (R2) (the DR severity is indicated in the scale $[1 \div 4]$, where 1 refers to null retinopathy, 2 to mild, 3 to moderate and 4 to severe). Half of them suffer of high blood pressure (HBP), half are males and half females. Only 4% are type 1 diabetic and the duration of the pathology varies in the range $[1 \div 12]$, with an average of 4.2 years.

First of all the diagnostic power of the tortuosity for the DR has been studied (table 6.3). The tortuosity has been evaluated with the ground truth manual measurements, the automatic "syntactical" tortuosity T', the automatic "local" tortuosity T_{bar} as well as with the other automatic "local" tortuosity T_{loc}. The tortuosity T has not been further analyzed because of its high correlation with the T' tortuosity. In the case of the automatic measures also the arteriolar and venular tortuosity have been considered. Moreover for each kind of measure the difference between the right and left eyes (suggested by the clinician as an important feature) and this difference times the tortuosity of the eye have been analyzed. In table 6.3 the statistically significant results (with $p < 0.05$) are highlighted in bold. It can be noticed that the highest correlation is achieved considering the tortuosity as expressed by T', but similar results have been obtained also with the local measure T_{bar}. On the contrary the manual tortuosity (as well as the automatic tortuosity T_{loc}) is not highly correlated with the DR and this correlations is not statistically significant, indicating that an automatic, quantitative and standardized measure as expressed by T' or T_{bar} is necessary. Another interesting result concerns the different behavior between arteries and veins when the tortuosity from both the eyes is considered: a different arteriolar tortuosity between the 2 eyes seems indicate a pathological condition whereas differences in the venular vasculature (and considering the whole vascular network) are not significant, indicating that in the case of arteries not only the single eye but also a comparison between the two eyes is needed for a reliable diagnosis of the retinopathy. Moreover it constitutes a further reason for the usage of a software that automatically detects arteries and veins and performs a separate analysis for the tortuosity. The discriminating power between DR and no DR of the measures presented above, has been proved also by the outcome

of the Wilcoxon test (the data are not gaussian), which showed significant p-values (of rejecting the null hypothesis of equal means between the 2 groups) for measures where also the R correlation is statistically significant.

	T_{man}	T'	T_{bar}	T_{loc}
$Tort$	$R = 0.19 (p = 0.09)$	$R = 0.50 (p = 10^{-6})$	$R = 0.49 (p = 10^{-6})$	$R = 0.03 (p = 0.79)$
$Atort$		$R = 0.47 (p = 10^{-5})$	$R = 0.46 (p = 10^{-5})$	$R = -0.11 (p = 0.28)$
$Vtort$		$R = 0.43 (p = 10^{-5})$	$R = 0.42 (p = 10^{-4})$	$R = 0.16 (p = 0.18)$
$\|Rtort - Ltort\|$	$R = -0.09 (p = 0.44)$	$R = 0.13 (p = 0.25)$	$R = 0.09 (p = 0.44)$	$R = -0.04 (p = 0.69)$
$\|RAtort - LAtort\|$		$R = 0.41 (p = 10^{-4})$	$R = 0.23 (p = 0.04)$	$R = -0.14 (p = 0.22)$
$\|RVtort - LVtort\|$		$R = -0.08 (p = 0.46)$	$R = -0.02 (p = 0.82)$	$R = -0.14 (p = 0.96)$
$\|Rtort - Ltort\| * tort$	$R = -0.08 (p = 0.43)$	$R = 0.16 (p = 0.18)$	$R = -0.09 (p = 0.43)$	$R = -0.03 (p = 0.73)$
$\|RAtort - LAtort\| * Atort$		$R = 0.49 (p = 10^{-5})$	$R = 0.23 (p = 0.04)$	$R = 0.01 (p = 0.24)$
$\|RVtort - LVtort\| * Vtort$		$R = -0.04 (p = 0.70)$	$R = -0.01 (p = 0.87)$	$R = 0.02 (p = 0.87)$

Table (6.3). *The Pearson R Correlation coefficient (with their p-value) between the DR level (scale=*$[1 \div 3]$*) and direct and indirect tortuosity measures. The columns refer to the different formulations of the vessel tortuosity, the rows to the type of vessels and indirect measures: the difference in tortuosity between the right and left eyes as well as its product with the tortuosity of the eye.*

The correlation between the tortuosity and other factors has been calculated and significant results have been obtained when the BP and the tortuosity manual measurements as well as the automatic tortuosity measure T_{loc} are considered, that is with the measures not informative for the DR. In particular the manual tortuosity showed with the BP an R negative correlation of -0.31 (p=0.0006), the T_{loc} an R correlation of -0.23 (0.045) and when just arteries are considered (AT_{loc}) an R correlation of -0.27 (p=0.017). Also in this case the Wilcoxon test confirmed these results. For the other factors not significant correlation have been measured.

The results above presented show that the tortuosity is an important sign diagnostic for the DR and it seems to be related also to the BP. Nevertheless these interesting results have been mostly obtained when automatic measures have been used, suggesting the needing of a quantitative and reproducible measure. The golden standard tortuosity is difficult to propose, because firstly it seems that beyond the matching with the clinical perception, its diagnostic power should be tested, moreover some measures are related more to the diabetic retinopathy, others to the high blood pressure. It seems

that a combination of the different tortuosity measures could be more informative than the single ones and a suitable "complete" measure should be investigated in a larger dataset.

Conclusions

This work dealt with computerized methods to perform the vascular analysis in fundus retinal images. The diagnostic (and sometimes also prognostic) value of many vascular signs is well known and there is a strong need of computerized tools to assess a quantitative, accurate, reproducible and standardized estimation of the vascular parameters. This procedure must be performed in an easy and fast way in order to be applicable in a clinical context, for example in screening programs involving everyday lots of patients and images to be graded.

In this thesis I presented algorithms that allow a comprehensive analysis of the vascular component in retinal images. They recognize the vascular network as a tree originating at the optic disc and opening towards the periphery: bifurcation after bifurcation the main vessels get narrower and finally become capillaries. These algorithms allow the automatic identification of vessel bifurcations and crossings, where many diagnostic parameters can be estimated, as well as the automatic detection of the optic disc and the fovea, important structures in the eye's physiology. Moreover an automatic classification of the arteriolar and venular vascular components is performed, allowing the diagnosis of pathologies which affect mainly a kind of vessels. These algorithms have been tested on many sets of images, kindly provided by important centers we collaborate with, as the Moorfields Eye Hospital, the King's College and the University of Winsconsin-Madison. The results obtained demonstrate a high accuracy and precision for the majority of these methods, achieved with computational time in the range between some seconds to some minutes, compatible with the clinical needs.

These modules have been conceived to be integrated in tools performing

different kinds of analysis. Two of them have already been implemented: the AVRnet and the TorTnet tools, for the analysis of the AVR parameter (measuring the generalized arteriolar narrowing) and of the tortuosity parameter, respectively. The both have been developed as web-based systems, in order to be used in a telemedicine context. These systems work half on the server machine, performing the more computationally demanding tasks, and half on the client machine, where the user checks for the automatic results and corrects potential errors via a user-friendly GUI. This is a "smart" GUI which detects possible mistakes of the system and allows to correct them by means of very few and easy operations.

The AVRnet tool has been validated on a large number of images, achieving a very high repeatability and accuracy, resulting from the comparison with ground truth manual measurements. TorTnet could not been validated in a similar way, firstly because the diagnostic role of the tortuosity parameter is not clear, in particular for the diabetic retinopathy, secondly because until now this parameter has been evaluated using a qualitative and subjective scale. We proposed new measures to estimate the tortuosity, considering not only the single vessel (different proposals have been already presented in literature about this subject), but also the entire image. These measures allowed to reproduce the clinical perception of the tortuosity with the similar variability existing between graders (we found they actually do not highly agree) and to understand the diagnostic power of the tortuosity for the diabetic retinopathy. Until now only beta versions of these two tools are available on request and we are developing similar tools for the estimation of other vascular parameters.

Bibliography

[1] J. A. Pugh, J. M. Jacobson, W. A. J. V. Heuven, J. A. Watters, M. R. Tuley, D. R. Lairson, R. J. Lorimor, A. S. Kapadia, and R. Velez, "Screening for diabetic retinopathy. the wide angle retinal camera," *Diabetes Care*.

[2] D. J. Taylor, J. Fisher, J. Jacob, and J. E. Tooke, "The use of digital cameras in a mobile retinal screening environment," *Diabetic Medicine*.

[3] H. M. Herbert, K. Jordan, and D. W. Flanagan, "Is screening with digital imaging using one retinal view adequate?" *Eye*.

[4] L. Varma, G. Prakash, and H. K. Tewari, "Diabetic retinopathy: time for action. no complacency, please!" *Bullettin of the World Health Organization*.

[5] M. Knudtson, K. Lee, L. Hubbard, T. Wong, R. Klein, and B. Klein, "Revised formulas for summarizing retinal vessel diameters," *Current Eye Research*, vol. 27, no. 3, pp. 143–149, Jul-Aug 2003.

[6] N. Patton, T. Aslam, T. MacGillivray, A. Pattie, I. J. Deary, and B. Dhillon, "Retinal vascular image analysis as a potential screening tool for cerebrovascular disease: a rationale based on homology between cerebral and retinal microvasculatures," *Anatomical Society of Great Britain and Ireland*.

[7] C.D.Murray, "The physiological principle of minimum work. i. the vascular system and the cost of blood volume," *Proceedings of the National Academy of Science*.

[8] A. V. Stanton, B. Wasan, A. Cerutti, S. Ford, R. Marsh, P. P. Sever, S. A. Thom, and A. D. Hughesy, "Vascular network changes in the retina with age and hypertension," *Journal of Hypertension*.

[9] Early Treatment Diabetic Retinopathy Study Research Group, "Grading diabetic retinopathy from stereoscopic fundus photographs- an extension of the modified Airlie House classification," *Ophthalmology*, vol. 98, pp. 786–806, 1991.

[10] N. M. Keith, H. P. Wegener, and N. W. Barker, "Some different types of essential hypertension: their course and prognosis," *American Journal of Medicine Science*.

[11] H. G. Scheie, "Evaluation of ophthalmoscopic changes of hypertension and arterial sclerosis," *Archives of Ophthalmology*.

[12] S. Chatterjee, S. Chattopahya, M. Hope-Ross, and P. L. Lip, "Hypertensionand the eye: changing perspectives," *Journal of Human Hypertension*.

[13] T. D. R. S. R. Group, "A modification of the airlie house classification of diabetic retinopathy," *Investigative Ophthalmology and Visual Science*.

[14] E. T. D. R. S. R. Group, "Early treatment diabetic retinopathy study design and baseline patient characteristics„" *Ophthalmology*.

[15] E. Poletti, D. Fiorin, E. Grisan, and A. Ruggeri, "Retinal vessel axis estimation through a multi-directional graph search approach," in *World Congress on Medical Physics and Biomedical Engineering*, vol. 25/11. Springer Berlin Heidelberg, 2009, pp. 137–140.

[16] O. Chutatape, L. Zheng, and S. Krishnan, "Retinal blood vessel detection and tracking by matched Gaussian and Kalman filters," in *Engineering in Medicine and Biology Society, 1998. Proceedings of the 20th Annual International Conference of the IEEE*, vol. 6.

[17] A. Hoover, V. Kouznetsova, and M. Goldbaum, "Locating blood vessels in retinal images by piecewise threshold probing of a matched filter re-

sponse," *IEEE Transactions on Medical Imaging*, vol. 19, no. 3, pp. 203–210, March 2000.

[18] A. Can, H. Shen, J. Turner, H. Tanenbaum, and B. Roysam, "Rapid automated tracing and feature extraction from retinal fundus images using direct exploratory algorithms," *IEEE Transactions on Information Technology in Biomedicine*, vol. 3, no. 2, pp. 125–138, 1999.

[19] F. Zana and J. Klein, "Segmentation of vessel-like patterns using mathematical morphology and curvature evaluation," *IEEE Transactions on Image Processing*, vol. 10, no. 7, pp. 1010–1019, 2001.

[20] H. Li, W. Hsu, M. Lee, and H. Wang, "A piecewise Gaussian model for profiling and differentiating retinal vessels," in *Proc. Int. Conf. Image Processing*, vol. 1. Citeseer, 2003, pp. 1069–1072.

[21] Y. Tolias and S. Panas, "A fuzzy vessel tracking algorithm for retinal images based on fuzzyclustering," *IEEE Transactions on Medical Imaging*, vol. 17, no. 2, pp. 263–273, 1998.

[22] E. Grisan, A. Pesce, A. Giani, M. Foracchia, and A. Ruggeri., "A new tracking system for the robust extraction of retinal vessel structure," in *Proc. 26th Annual International Conference of IEEE-EMBS*. New York: IEEE, 2004, pp. 1620–1623.

[23] D. Fiorin, E. Poletti, E. Grisan, and A. Ruggeri, "Fast adaptive axis-based segmentation of retinal vessels through matched filters," in *World Congress on Medical Physics and Biomedical Engineering*, vol. 25/11. Springer Berlin Heidelberg, 2009, pp. 145–148.

[24] S. A. Salem, N. M. Salem, and A. K. Nandi, "Segmentation of retinal blood vessels using a novel clustering algorithm (RACAL) with a partial supervision strategy," *Medical and Biological Engineering and Computing*, vol. 45, no. 3, pp. 261–273, 2007.

[25] A. Giani, E. Grisan, M. D. Luca, and A. Ruggeri, "Detecting false vessel recognitions in retinal fundus analysis," in *Proc. 28th Annual Interna-*

tional Conference of IEEE-EMBS. New York: IEEE, 2006, pp. 4449–4452.

[26] S. Tamura, Y. Okamoto, and K. Yanashima, "Zero-crossing interval correction in tracing eye-fundus blood vessels." *Pattern Recognition*.

[27] C. Sinthanayothin, J. Boyce, and C. Williamson, "Automated localisation of the optic disc, fovea, and retinal blood vessels from digital colour fundus images," *British Journal of Ophthalmology*.

[28] H. Li and O. Chutatape, "Automatic location of optic disc in retinal images," *IEEE ICIP*.

[29] C. Duanggate, B. Uyyanonvara, and S. Makhanov, "Parameter-free optic disk detection," *Computerized Medical Imaging and Graphics*.

[30] A. Sopharak, B. Uyyanonvara, S. Barman, and T. Williamson, "Automated detection of diabetic retinopathy exudates from non-dilated retinal images using mathematical morphology methods," *Computerized Medical Imaging and Graphics*.

[31] S. Sekhar, W. Al-Nuaimy, and A. Nandi, "Automatic localisation of retinal optic disk using hough transform," *In: The 5th IEEE international symposium on biomedical imaging: from nano to macro*.

[32] R. J. Qureshi, L. Kovacs, B. Harangi, B. Nagy, T. Peto, and A. Hajdu, "Combining algorithms for automatic detection of optic disc and macula in fundus images." *Computer vision and image understanding*.

[33] G.A.Hoover and M.Goldbaum, "Locating the optic nerve in a retinal image using the fuzzy convergence of the blood vessels," *IEEE Transaction on Medical Imaging*.

[34] A.Youssif, A.Ghalwash, and A.Ghoneim, "Optic disk detection from normalized digital fundus images by means of a vessels' direction matched filter," *IEEE Transaction on Medical Imaging*.

[35] M. Foracchia, E. Grisan, and A. Ruggeri, "Detection of optic disk in retinal images by means of a geometrical model of vessel structure," *IEEE Transaction on medical imaging*, vol. 23, no. 10, pp. 1189–1195, 2004.

[36] J. Staal, M. Abramoff, M. Niemejer, M. Viergever, and B. van Ginneken, "Ridge based vessel segmentation in color images of the retina," *IEEE Transaction on Medical Imaging*.

[37] T. Ciulla, A. Amador, and B. Zinman, "Diabetic retinopathy and diabetic macular edema." *Diabetes Care*.

[38] Early Treatment Diabetic Retinopathy Study Research Group, "Early photocoagulation for diabetic retinopathy. ETDRS report number 9." *Ophthalmology*, vol. 98, pp. 766–785, 1991.

[39] G. Tikellis, M. C. Gillies, R. H. Guymer, I. L. McAllister, J. E. Shaw, and T. Y. Wong, "Retinal vascular caliber and macular telangiectasia type 2," *Ophthalmology*.

[40] H. Narasimha-Iyer, A. Can, B. Roysam, C. Stewart, H. Tanenbaum, A. Majerovics, and H. Singh, "Robust detection and classification of longitudinal changes in color retinal fundus images for monitoring diabetic retinopathy," *IEEE Transactions on Biomedical Engineering*.

[41] M. Niemeijer, M. Abràmoff, and B. Ginneken, "Segmentation of the optic disc, macula and vascular arch in fundus photographs," *IEEE Transactions on Biomedical Engineering*.

[42] H. Li and O. Chutatape, "Automated feature extraction in color retinal images by a model based approach," *IEEE Transactions on Biomedical Engineering*.

[43] D. Welfera, J. Scharcanskia, and D. R. Marinho, "Fovea center detection based on the retina anatomy and mathematical morphology," *Computer methods and programs in biomedicine*.

[44] J. Staal, M. Abramoff, M. Niemeijer, M. Viergever, and B. van Ginneken, "Ridge based vessel segmentation in color images of the retina," *IEEE Transactions on Medical Imaging*, vol. 23, no. 4, pp. 501–509, 2004.

[45] C. U. STARE project, "http://www.ces.clemson.edu/ ahoover/stare."

[46] T. Kauppi, V. Kalesnykiene, J.-K. Kämäräinen, L. Lensu, I. Sorri, A. Raninen, R. Voutilainen, H. Uusitalo, H. Kälviäinen, and J. Pietilä, "Diaretdb1 diabetic retinopathy database and evaluation protocol," *Medical Image Understanding and Analysis (MIUA)*.

[47] H. W.E., G. M., C. B., K. P., and N. M.R., "Measurement and classification of retinal vascular tortuosity," *International Journal of Medical Information*.

[48] N. Patton, R. Maini, T. MacGillivary, T. M. Aslam, I. J. Deary, and B. Dhillon, "Effect of axial length on retinal vascular network geometry," *American Journal of Ophthalmology*.

[49] C.-L. Tsai, C. V. Stewart, H. L. Tanenbaum, and B. Roysam, "Model-based method for improving the accuracy and repeatability of estimating vascular bifurcations and crossovers from retinal fundus images," *IEEE TRANSACTIONS ON INFORMATION TECHNOLOGY IN BIOMEDICINE*.

[50] M. E. Martinez-Perez, A. D. Hughes, A. V. Stanton, S. A. Thom, N. Chapman, A. A. Bharath, and K. H. Parker, "Retinal vascular tree morphology: A semi-automatic quantification," *IEEE Transactions on biomedical engineering*.

[51] D. Calvo, M. Ortega, M. G. Penedo, and J. Rouco, "Automatic detection and characterisation of retinal vessel tree bifurcations and crossovers in eye fundus images," *Computer methods and programs in biomedicine*.

[52] G. Azzopardi and N. Petkov, "Detection of retinal vascular bifurcations by trainable v4-like filters," *Computer Analysis of Images and Patterns*.

[53] D. S. Bashir Al-Diri, Andrew Hunter and M. Habib, "Automated analysis of retinal vascular network connectivity," *Computerized medical imaging and graphics*.

[54] K. Rothaus, X. Jiang, and P. Rhiem, "Separation of the retinal vascular graph in arteries and veins based upon structural knowledge," *Image and Vision Computing*,

vol. 27, no. 7, pp. 864–875, giugno 2009. [Online]. Available: http://linkinghub.elsevier.com/retrieve/pii/S0262885608000590

[55] K. Akita and H. Kuga, "A computer method of understanding ocular fundus images," *Pattern Recognition*, vol. 15, no. 6, pp. 431–443, 1982.

[56] E. Grisan and A. Ruggeri, "A divide et impera strategy for automatic classification of retinal vessels into arteries and veins," *25th Annual International Conference of IEEE-EMBS Proceedings*, vol. 25, pp. 890–894, 2003.

[57] M. Niemeijer, B. van Ginneken, and M.D.Abramoff, "Automatic determination of the artery-vein ratio in retinal fundus images," in *SPIE Proceedings*, vol. 7624, 2010, pp. 76 240I–1–8.

[58] D. K. Claudia Kondermann and M. Yan, "Blood vessel classification into arteries and veins in retinal images," *Medical Imaging 2007: Image Processing*, vol. 6512, no. 1, pp. 651 247–9, 2007.

[59] C. Muramatsu, Y. Hatanaka, T. Iwase, T. Hara, and H. Fujita, "Automated detection and classification of major retinal vessels for determination of diameter ratio of arteries and veins," *Medical Imaging 2010: Computer-Aided Diagnosis*, vol. 7624, pp. 76 240J1–76 240J8, 2010.

[60] M. Niemeijer, B. van Ginneken, and M. D. Abramoff, "Automatic classification of retinal vessels into arteries and veins," *SPIE Medical Imaging Proceedings*, vol. 7260, p. 72601F, 2009.

[61] L. Tramontan and A. Ruggeri, "Computer estimation of the avr parameter in diabetic retinopathy," in *World Congress on Medical Physics and Biomedical Engineering*, vol. 25/11. Springer Berlin Heidelberg, 2009, pp. 141–144.

[62] The DCCT Group, "Color photography vs. fluorescein angiography in the detection of diabetic retinopathy in the Diabetes Control and Complications Trial," *Arch Ophthalmol*, vol. 105, pp. 1344–51, 1987.

[63] L. Tramontan, E. Poletti, D. Fiorin, and A.Ruggeri, "A web-based system for the quantitative and reproducible assessment of clinical indexes from

the retinal vasculature," *IEEE Trans Biomed Eng*, vol. 58, no. 3, pp. 818–821, 2010.

[64] T. Wong, R. Klein, B. Klein, J. Tielsch, L. Hubbard, and F. Nieto, "Retinal microvascular abnormalities, and their relation to hypertension, cardiovascular diseases and mortality," *Survey Ophthalmology*, vol. 46, no. 1, pp. 59–80, Jul-Aug 2001.

[65] L. D. Hubbard, R. J. Brothers, W. N. King, L. X. Clegg, R. Klein, L. S. Cooper, A. R. Sharrett, M. D. Davis, and J. Cai, "Methods for evaluation of retinal microvascular abnormalities associated with hypertension/sclerosis in the atherosclerosis risk in communities study„" *Ophthalmology*, vol. 106, no. 12, pp. 2269 – 2280, 1999.

[66] M. Ortegaa, N. Barreiraa, J. Novoa, M. Penedoa, A. Pose-Reinob, and F. Gomez-Ulla, "Sirius: A web-based system for retinal image analysis," *Internation journal of medical informatics*.

[67] A. Perez-Rovirez, T. MacGillivray, E. Trucco, K. S. Chin, A. Giachetti, C. Lupescu, D. Tegolo, P. J. Wilson, A. Doney, A. Laude, and t. . V. y. . . B. Dhillon", booktitle = Proceedings 33th International IEEE EMBS Conference.

[68] L. Tramontan, E. Grisan, and A. Ruggeri, "An improved system for the automatic estimation of the arteriolar-to-venular diameter ratio (avr) in retinal images," in *30th Annual International Conference of IEEE-EMBS*, 2008, pp. 3550–3553.

[69] S. Bursell, J. Cavallerano, A. Cavallerano, A. Clermont, D. Birkmire-Peters, L. Aiello, and L. Aiello, "Stereo nonmydriatic digital-video color retinal imaging compared with Early Treatment Diabetic Retinopathy Study seven standard field 35-mm stereo color photos for determining level of diabetic retinopathy," *Ophthalmology*, vol. 108, no. 3, pp. 572–585, 2001.

[70] S. M.B., W. J.J., and D. K. et al., "Alterations in retinal microvascular geometry in young type 1 diabetes," *Diabetes Care*.

[71] S. M.B., W. T.Y., and D. K. et al., "Retinal arteriolar tortuosity is associated with retinopathy and early kidney dysfunction in type 1 diabetes," *American Journal of Ophtalmology*.

[72] K. J.K., G. M.S., and S. E., "Retinal vessel dilation and elongation precedes diabetic macular oedema," *British Journal of Ophtalmology*.

[73] T. N.C., M. I.C., and S. B. et al., "Straight versus tortuous retinal arteries in relation to blood pressure and genetics." *British Journal of Ophtalmology*.

[74] G. Dougherty and M. J. Johnson, "Measurement of retinal vascular tortuosity and its application to retinal pathologies," *Medical and Biological Engineering and Computing*.

[75] D. K. Wallace, "Computer-assisted quantification of vascular tortuosity in retinopathy od prematurity (an american ophtalmological society thesis)," *Transactions of the American Ophthalmological Society*.

[76] E. Grisan, M. Foracchia, and A. Ruggeri, "A novel method for the automatic grading of retinal vessel tortuosity," *IEEE Transactions on medical imaging*.

[77] E. Trucco, H. Azegrouz, and B. Dhillon, "Modeling the tortuosity of retinal vessels: does the caliber play a role?" *IEEE Transactions on biomedical engineering*.

[78] K. V. Chandrinos, M. Pilu, R. B. Fisher, and P. Trahanias, "Image processing techniques for the quantification of atherosclerotic changes," in *Proceedings MEDICO98*, Limassol, Cyprus, 1998.

[79] C. G. Owen, A. R. Rudnicka, R. Mullen, S. A. Barman, D. Monekosso, P. H. Whincup, J. Ng, and C. Paterson, "Measuring retinal vessel tortuosity in 10-year-old children: Validation of the computer-assisted image analysis of the retina (caiar) program," *Investigative Ophthalmology & Visual Science*.

[80] A. Ruggeri, E. Poletti, D. Fiorin, L. Tramontan, and T. Peto, "A Web-based System for Vessel Tortuosity Estimation in Retinal Images," in *Proceedings ARVO11*, 2011.